ADVANCED NANOMATERIALS AND DEVICES FOR SPACE APPLICATIONS

By

Kan Xie

A DISSERTATION

Submitted
to Michigan State University
in partial fulfillment of the requirements
for the degree of

Electrical Engineering – Doctor of Philosophy

2017

ProQuest Number: 10688880

ProQuest

ProQuest 10688880

ABSTRACT

ADVANCED NANOMATERIALS AND DEVICES FOR SPACE APPLICATIONS

By

Kan Xie

A new era of space exploration has been ushered in by a new generation of spacecraft with significantly reduced size, weight, and power (SWAP). Such new spacecraft include Small-Sats, CubeSats, and even MicroSats, and they can operate as constellations to perform complex and novel measurements. These new spacecrafts cannot, however, carry the traditional complements of radiation and thermal shielding needed by instruments to survive the harsh space environments. This unique situation presents multiple challenges and numerous opportunities for innovative materials and devices with inherent resiliences.

In this thesis work, the responses to heavy ion irradiation of carbon onions and two sets of GaN nanowire based NanoFETs were investigated. Heavy Ions are a highly penetrating component in space environments. Key features of the space environment were obtained through use of heavy ion beams provided by the National Superconducting Cyclotron Laboratory (NSCL) at Michigan State University. The important features for accurate space simulation are high energies and high charges, i.e., almost fully stripped. These conditions cannot be obtained using an ion implanter. Access to the NSCL enabled the possibility of collecting unique datasets that provided true insights on heavy ion interaction with nanomaterials and devices.

This thesis start with the investigation on carbon onions as potential solid space lubricants. This continuous research effect in collaboration with Tokyo Institute of Technology that explores the possibility of using carbon onions in vacuum and radiation environments. Carbon onions synthesized in temperature series are studied primarily with transmission electron microscope (TEM). Their post radiation structures are recorded, a possible mechanism of structure change for carbon onions under radiation is presented base on analysis of

results.

Second part of this thesis presents the candidate's results and analyses from the investigation of the first known real-time experimental data for Gallium nitride (GaN) nanowire based field effect transistors (nanoFETs) under accurately simulated heavy ion irradiation conditions. Data from the I-V performance during xenon-124 relativistic heavy ion radiation was obtained at the NSCL. The candidate's contributions include development of a unique stability analysis that was used to enable new and accurate electron transport modeling based on thermionic field emission at metal-semiconductor contact Schottky barrier. This further enabled first-time extractions of barrier heights, carrier concentrations and tunneling transmission coefficients from the unique experimental data sets. A complete metal-semiconductor-metal approach was also developed and implemented that enabled extraction of all voltage drops across the nanoFET device as a function of radiation exposure. When the electronic investigation is combined with observed fundamental physical changes of the nanowire by radiation, new concepts of charge distribution and the role of surface orientation of GaN nanowires emerge. Analysis of such unique data sets opens the gateway for the studies of nanoFET device performance in space radiation environments. Work to date and proposed investigations are presented as future work. This investigation represents the main body of the candidate's work.

Initial results from a recent investigation by the candidate into surface acoustic wave enhanced quantum relay devices targeted to space-based quantum communication are also presented as latest work. This study aligned with the current trends in the field of quantum communication technology; the thesis work contributes to a creative approach on how to achieve improved quantum entanglement and coherence in electron spin based devices using surface acoustic waves. Details of surface acoustic wave device fabrication are presented in the third part of this thesis.

To Mother,
for her continuous love and support.

TABLE OF CONTENTS

LIST OF TABLES

LIST OF FIGURES

x

CHAPTER 1

INTRODUCTION

1.1 Problem Description and Motivation

A new era of space exploration has been ushered in by a new generation of spacecraft with significantly reduced size, weight, and power (SWAP) [1]. Such new spacecraft includes SmallSats, CubeSats, and even MicroSats, and they can operate as constellations to perform complex and novel measurements. These spacecrafts cannot, however, carry the traditional components for radiation and thermal shielding needed by instruments to survive the harsh space environments. An extreme environment for materials in space exists because the following stressors are present, either singly or in combination: radiation, vacuum and thermal stress [2]. This unique situation presents multiple challenges and numerous opportunities for innovative materials and devices with inherent resilience.

In this thesis work, the candidate focuses on two specific areas within the larger arena of device and materials in space radiation environments. These are 1) a carbon-based nanomaterial (carbon onions) intended to serve as a solid lubricant in space and 2) a nanowire-based field effect transistor architecture whose aim is to function as a traditional MOSFET but without radiation hardening or heavy shielding. Unique experiments are performed in an accurately simulated heavy ion radiation environment enabled by the National Superconducting Cyclotron Laboratory (NSCL) at Michigan State University (MSU). The candidate's work includes some first of their kind radiation results. Analysis and interpretation of these results constitute the central contribution of this thesis.

For the carbon onions, the lubrication performance is dependent mechanically on the arrangement of layers within the material. Therefore material layer shifting, and re-arrangement for prior versus post radiation conditions are investigated. As carbon onion morphologies are known to vary as a function of growth temperature [3], the thesis investigations are

performed for three sets of carbon onions as a temperature series. These results reveal new information about how multilayer graphene interacts with heavy ions while in radial versus linear arrangements, and how energy may stored and transferred in the onions. The impact of the observed re-arrangements on lubrication performance is also discussed.

For the nanoFET study, key results from real-time investigations for these devices under heavy ion irradiation are presented for the first time. Three new contributions by the candidate are:

1. Stability analysis

2. Thermionic field emission transport through the controlling Schottky barrier and

3. Complete metal-semiconductor-metal device modeling, enabled the first-time extraction of key transport and controlling parameters as a function of time in the beam.

In the last chapter of this thesis, an initial investigation of a new nanocircuit targeted to use as quantum communication relay is also presented. Explorations of active transport modulation by surface acoustic waves (SAW) are given, and device fabrication issues are addressed. This work is promising, both for small spacecraft deployment and for improvements to terrestrial quantum communication circuits.

1.2 CubeSats in Space

CubeSats or U-Class spacecraft, are a type of miniature satellite built to be multiples of 10cm*10cm*10cm (1U) cubic units that typically weight less than 3lbs. From the early 2000s, these satellites have been launched into space as secondary loads with existing missions.

CubeSats are research-purpose spacecraft that can be made with off the shelf commercial materials and components at a much cheaper cost than conventional spacecraft. The initial aims of the CubeSat project included partnering with universities to provide space access opportunities for their students, this goal was successfully achieved. However, many more

groups have recognized and adapted the idea of using CubeSats as scientific research platforms in space environments. Moreover, the technologies used to enable CubeSat launches and maintenance have brought rapid advancements in propulsion, thermal management and communication [4].

The majority of CubeSats currently in operation are stationed in low Earth Orbits (LEO) only. LEO is approximately 2000km or less above Earth surface with an orbital period of between 84 and 127 minutes. In the LEO regime, radiation from the Sun dominates with delivery of substantial amounts of protons, and heavy ions, which become trapped particles. These solar particles are then modulated by galactic cosmic rays, the Earth's atmospheric along with neutrons and other trapped particles, together forming a true dynamic system. Solar events can be categorized into gradual and impulse solar events, and both can result in increased levels of protons and heavy ions with initial energies of 100s of MeV for protons and 100s of GeV for heavier ions.

The research presented in this thesis is therefore targeted to radiation that affects mechanical and electrical performances of devices and/or materials intended to be deployed/used by CubeSat platforms that operate in LEO. Space is a harsh environment for traditional earth materials to survive in due to the extreme temperature ranges, vacuum conditions and a variety of radiation interactions without the protection of Earth's atmosphere.

1.3 The Space Radiation Environment

Solar radiation and galactic cosmic rays are the two-main sources of radiation in space [5], Figure 1.1 demonstrates how the earth's magnetic field deflects the constant bombardment of high energy charged particles and how energetic particles are trapped near the orbit where CubeSats operate (low earth orbit: LEO).

When the charged particles interact with mechanical and electrical materials/devices in space, two kinds of radiation damage are usually considered based on the radiation time scale.
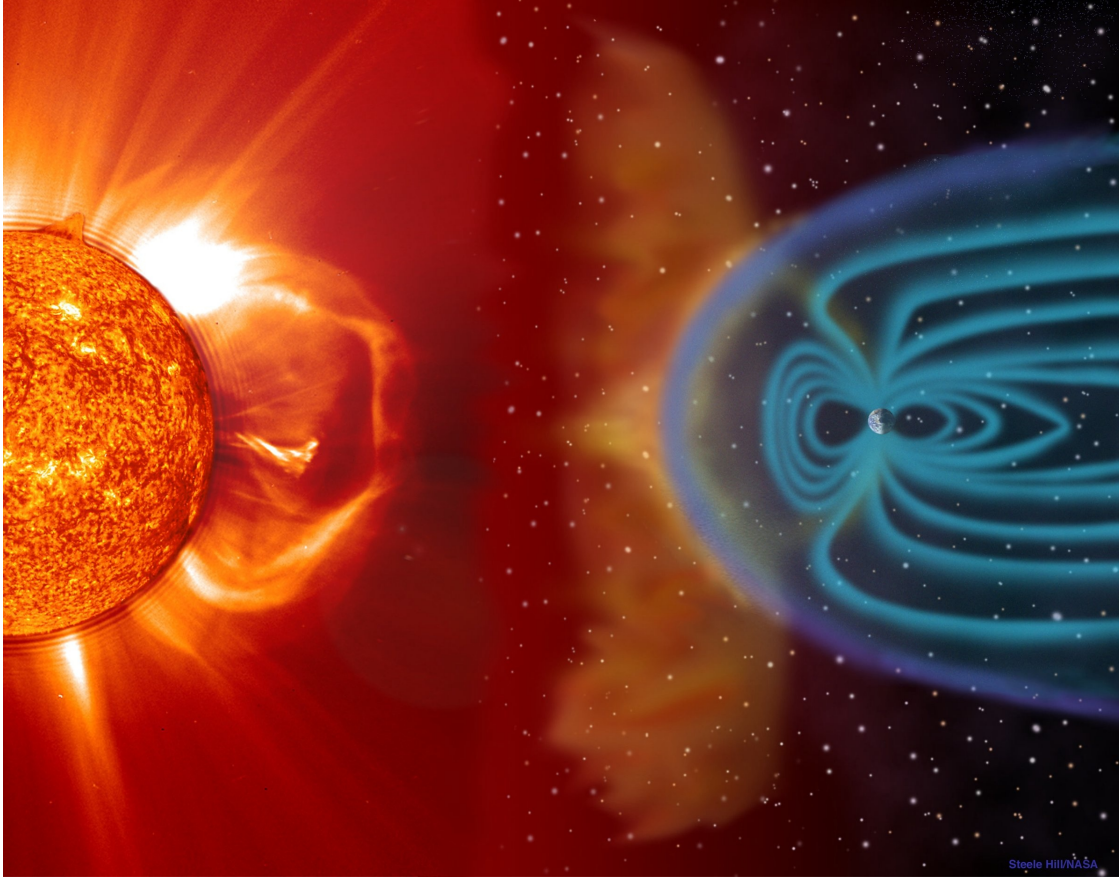
Figure 1.1 Demonstration of the dynamic radiation environment in Low Earth Orbits. Image credit: NASA

One is total ionizing dose (TID) with displacement damage dose (DDD), which considers the long-term effect of radiation effect over time. The other is single event effects (SEEs) that occur when a single charged particle passes through/by the material[6, 7].

Total ionizing dose (TID) is the cumulative long-term ionization damage due to protons and electrons. TID effects typically includes threshold shifts, leakage current, timing skew and functional failures in current state of the art metal oxide semiconductor field effect transistors (MOSFETs). The deleterious effect of low energy protons and electrons can be partially mitigated with shielding[6, 7].

Displacement damage dose (DDD) refers to the long term non-ionizing damage due to protons, electrons and neutrons. This type of damage can produce device degradation in optocouplers, solar cells, charge coupled devices(CCDS) and linear bipolar devices; however,

4

shielding can be very effective to mitigate this kind of radiation damage depending on the onboard location of the devices[6, 7].

Single event effects (SEE) are usually caused by heavy ions. These are highly charged particles that can easily penetrate most shielding. SEEs are the most dangerous of all radiation effects in space applications, as the type of effect can be dynamic and is largely dependent on the fundamental interaction with the device and material[6, 7]. Heavy ion interactions are the major space environment component considered in this thesis.

1.4 Radiation Experiments at the National Superconducting Cyclotron (NSCL)

The heavy ion irradiation experiments are performed at the NSCL at Michigan State University [8]. The NSCL uses a coupled cyclotron system containing a smaller K500 accelerator followed by a larger K1200 accelerator. The state of art facility produces highly uniform, high energy and almost fully stripped particle beams.

The accelerated and striped ion beam is then steered towards specific chambers for variety of investigations. The Single Event Effects Testing Facility (SEETF) [9] developed in partnership with NASA, is used for the series of experiments performed in this thesis. Figure 1.2 demonstrates the accelerating process of a heavy ion beam at NSCL and Figure 1.3 shows the actual experimental set-up at the SEETF vault.

The single-event effect test facility (SEETF) at Michigan State University's National Superconducting Cyclotron Laboratory (NSCL) delivers highly energetic and penetrating heavy-ion beams (see Table 1.1) [9]. Such ion beams make possible testing of many circuit components without delidding or other significant modification. In addition, the extended energy range at NSCL makes it possible to reproduce 99% of the space radiation spectrum [9] in energy (MeV)/amu and in linear energy transfer (LET) MeV cm^2mg. Moreover, the high ion energy means that testing can be done in air, rather than in vacuum, simplifying
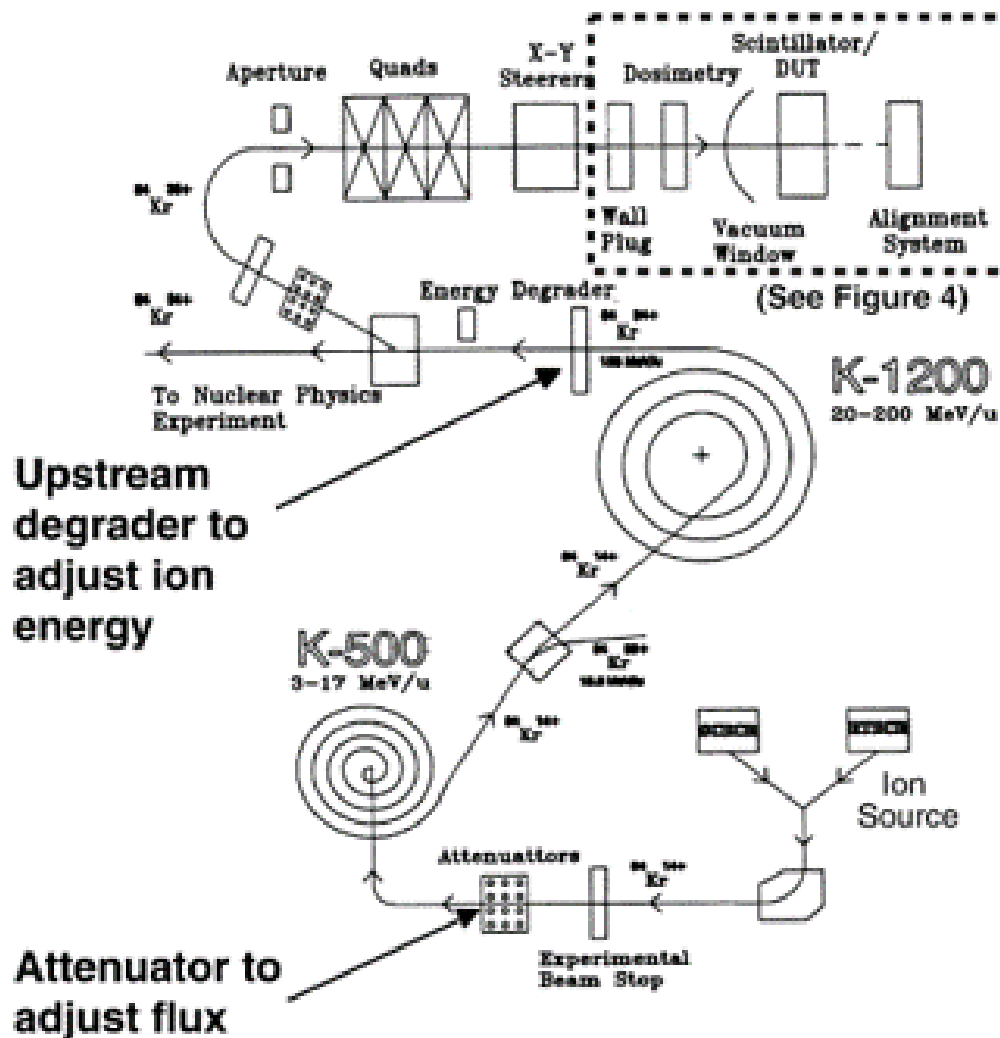
Figure 1.2 Particle acceleration process at NSCL, with smaller K500 accelerator followed by K1200 accelerator, beam path is shown before they are sent to each vault. Image Credit: R Ladbury et al. IEEE T. Nucl.Sci.51,3664 (2004)

issues such as device under test (DUT) cooling and access.

The SEETF facility with NSCL primary and /or mixed beams provides the user with the ability to simulate devices and materials interactions with space environments while recording live data. The SEETF is the ideal set-up to study for the first time heavy-ion interactions with nanomaterials and nanocircuits in a space application appropriate setting.
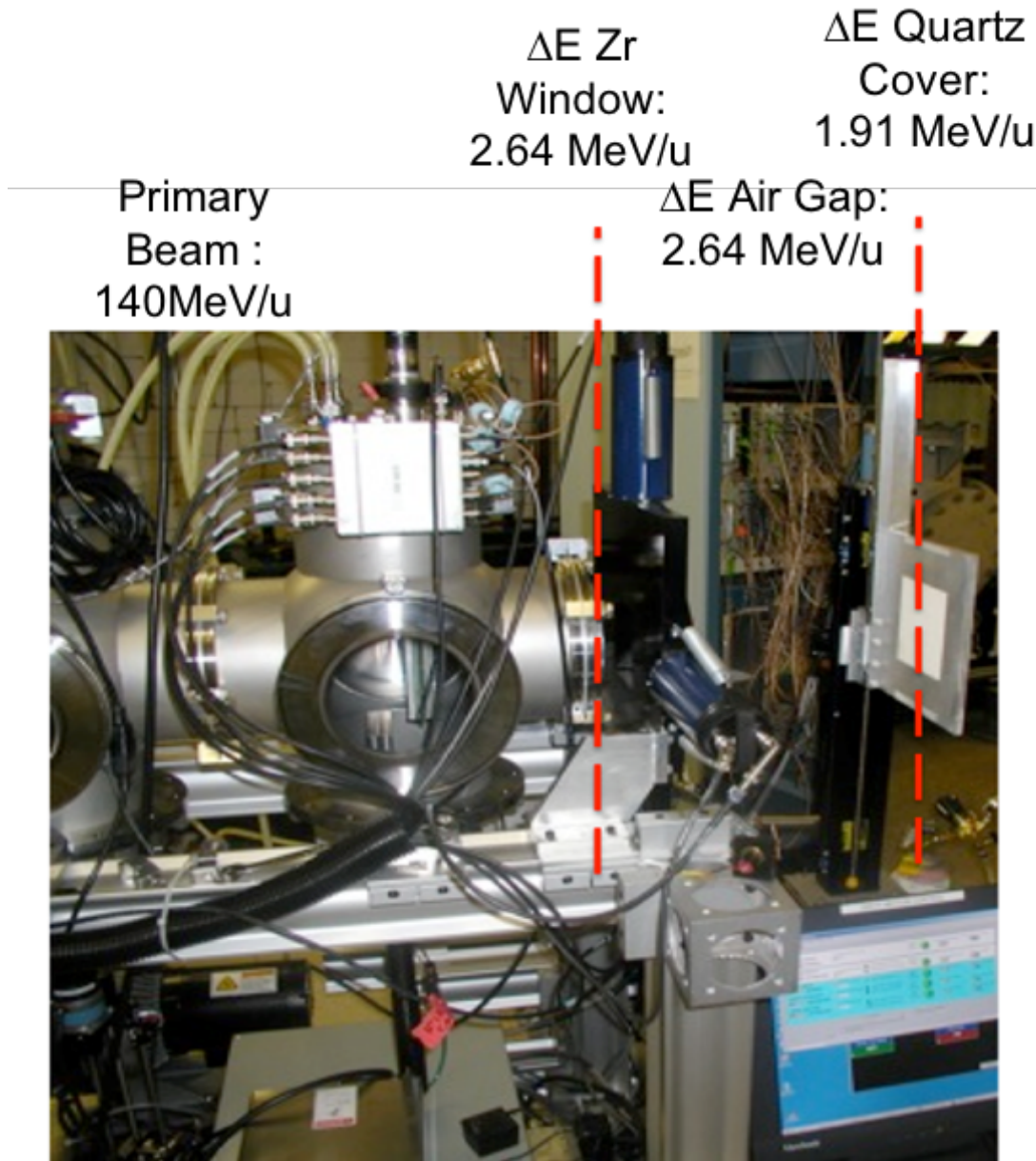
Figure 1.3 Experimental set-up inside SEETF, showing beam exit window with air gap, as well as final beam on target energy for a xenon primary beam with energy of 140MeV/u.

Table 1.1 Partial list of available Ions at NSCL, with ranges and LETs in Si

Ion	Facility	Max Energy (MeV/amu)	LET in Si (MeV $*$ cm^2/mg)	Range in Si (µ m)	Bragg-Peak in Si
Ar-36	NSCL	143	1.50	8860	18
Kr-78	NSCL	121	6.08	4440	40
Xe-136	NSCL	131	14.1	3070	69
Bi-209	NSCL	72	42	1100	100

1.5   Lubricants for Space Applications

Space exploration calls for innovative materials to be used in all systems. This includes all the moving parts such as the reaction wheel for attitude control inside a satellite which spins continually around the clock. Due to the extreme and harsh environment in space, lubrication for moving parts presents extraordinary challenges compared to standard lubrication challenges for ground-based applications.

An extreme environment for lubricants exists whenever the following stressors are present, either singly or in combination: radiation, vacuum and thermal stress [2] Space satellites and particle colliders are examples of applications in which radiation, vacuum, and thermal stress can severely degrade current state-of-the-art lubricant performance [2]. Many well publicized failures, including stuck bolts on the Hubble Space Telescope that required spacewalk intervention, or accelerated wear and failure of the soft gold electrical contacts at the Large Hadron Collider, can be traced back to the failure of current state-of-the-art lubricants due to radiation, vacuum, and thermal stress [10].

Both solid and liquid lubricants have been used in space. A brief analysis of their advantages and disadvantages is presented here.

Liquid lubricants that have been used in space including silicones, mineral oils, perfluoropolyalkylethers (PFPAE), polyalphaolefins, polyolesters, and multiply-alklated cycolpentanes [10, 3, 3, 11, 12, 13, 14, 15, 16]. Due to the weight limits on spacecraft, lubricated rolling-element bearings with small liquid reservoirs and/or porous cages are used instead large reservoirs of liquid lubricant and pumping systems. Liquid lubrication can be lost through vaporization, creep or inadequate supply. Low vapor-pressure fluids are therefore

used as labyrinth seals to prevent vaporization. Barrier films are used to counteract creep and positive feed systems are designed to control and flow of lubricant to ensure proper level of supply.

Grease lubricants, which are semisolid liquids, are also used as space lubricants. Grease is made from liquid lubricant with a thickener that holds the oils in place and provides a resistance to flow. The thickener can be soaps in which a metallic elements such as lithium, calcium, sodium, or aluminum is reacted with a fat or fatty acid. Fine particles can also be used as additives. Greases are in general a better choice for space lubricants than liquids, because grease can act as a reservoir for supplying oil to contacting surfaces, and can also act as a physical barrier to prevent oil loss by creep or centrifugal forces [3, 17].

Solid lubricants can be implemented in several kinds of materials. In general, soft metal films, lamellar solids, polymers and other low shear strength materials are used as solid lubricants for space applications. A solid lubricant can be directly applied onto to a roughened metallic surface or can be deposited using a liquid binding system. Sputtering and ion plating are used as well. Solid lubricants can provide ultra-low friction and wear properties; however, the lifecycle and performance of solid lubricant are largely dependent on the material itself, and its operating conditions.

Although these have all been used as space lubricants since the inception of the space program, these traditional lubricants, liquid, semi liquid and solid, all have major disadvantages. Liquid lubricants such as mineral oils, sila hydrocarbon oils, and polyester-olester preparations can fail due to the lack of a gravitational field which creates difficulty in forming or maintaining a proper seal [2]. Also, these lubricants are largely temperature dependent for their lubrication performance [2, 18]. Other lubricants including graphite, tungsten/molybdenum disulfide and high to ultra-high molecular weight polymers, in semi liquid and solid preparations are susceptible to structural collapse in a vacuum and/or radiation environment as well as liquid flow and loss issues, when used in semi liquid preparations [2, 18]. Polymers are also vulnerable to chemical modification under thermal stress with the

potential loss of mechanical properties [10]. This is where carbon nano materials come in.

1.5.1 Nano-Carbon Materials as Space Lubricants

Carbon-derived materials have outstanding terrestrial lubrication properties and graphite lubricants have been used for many decades. Other carbon-based materials are among the newest lubricant candidates. Carbon nano-particles and carbon films including diamond, diamond-like and graphite-like carbons are presently being investigated for lubrication applications [2]. However, carbon based nano-particles have some unique properties which make them promising candidates for consideration and testing in space as well as terrestrial applications. Carbon based nano-particles appear to be heat resistant, radiation hard, durable and have demonstrated low coefficient of friction (0.01 to 0.10) in tribocouple applications/experiments performed in vacuum [19].

Carbon nano-onions(CNOs) combine elements of diamond sp3 bonding, sp2 graphene in layers and multi-cage arrangements of known, and stable hexagon-pentagon combinations. These materials have been shown to have tribological properties superior to the natural materials in many instances. Recent studies including some by our group with a collaborative partnership at Tokyo Institute of Technology indicate that CNOs have superior coefficient of friction and endurance lifetimes in ultrahigh (vacuum regime characterized by pressures lower than about 10^{-7} pascal or 100 nanopascals) vacuum [19]. This is a significant improvement over graphite lubricants which collapse in vacuum environments. Multiwall carbon nanotubes (MWCNTs) have also demonstrated promising properties. Both CNOs and MWCNTs show better lubrication performance than C60s (Single cage buckyballs) and single wall carbon nanotubes (SWCNTs), which both display pronounced agglomeration that limits their lubrication performances. These results in air and in vacuum are reviewed in chapter 2 of this thesis.

Potential space and aeronautic applications of nanolubricants include the development of microelectromechanical systems (MEMS), and micromachines. Nanolubricants can be

applied to or grown on contacting surfaces in relative motion.Because the tribological properties of materials are extremely system dependent (i.e., the friction, wear, and lubricating ability are strongly dependent on such operating conditions as load, speed, type of contact, temperature, and atmosphere), it is imperative that technology testing simulate as closely as possible the particular space application. The vacuum, load, speeds, etc., can be simulated fairly easily on the ground, but it is not as easy to simulate radiation/atomic oxygen environment and zero gravity of low Earth orbit. Hence the importance of experiments at NSCL.

Despite the promise demonstrated by CNOs, the candidate's thesis results are among the very few investigations ingestions of radiation interactions with CNOs. In chapter 2 of this thesis, the heavy ion radiation effect study of carbon nano-onions is presented with state of the art comparisons given in Table 2.1, and space relevant anticipated effects on lubrication performance are extracted and presented in Table 2.2.

1.6 Electronics in Space Environments

Electronics in space face trapped protons and electrons in Earth's Van Allen radiation belts, solar disturbances that cause both the radiation with thermal loads and higher energy solar and cosmic rays with a highly penetrating heavy ion component [20]. Two types of damage usually occur in the case of electronic devices in the space environment, one being the single event effect (SEE) caused by heavy ions and high energy protons, the other being charge accumulation within devices due to long term space exposure [21].

Traditional silicon-based field-effect transistors including widely used MOSFETs, are embedded in almost all electronic device chipsets. Traditional MOSFET architectures are prone to radiation damage mainly in three key components. These are: the source and drain semiconductor-metal contacts, the semiconductor substrate channel and the insulating layer between the metal gate and the channel.

In the event of heavy ion radiation, highly energetic particles can pass through the carefully sandwiched MOSFET device, leaving a defect trail along their paths, as shown in Figure 1.4 . Among the three key component areas, the very thin insulting layer usually made from oxide is the most fragile since the on and off threshold in MOSFET is strongly capacitively coupled with the insulting layer [22] as demonstrated by the C dependence in the threshold voltage equations below.

$$V_{th} = V_{FB} + \varphi_s + \frac{Q_B}{C_i} \tag{1.1}$$

$$V_{FB} = \Phi_{ms} - \frac{Q_f + Q_m + Q_{ot}}{C_i} \tag{1.2}$$
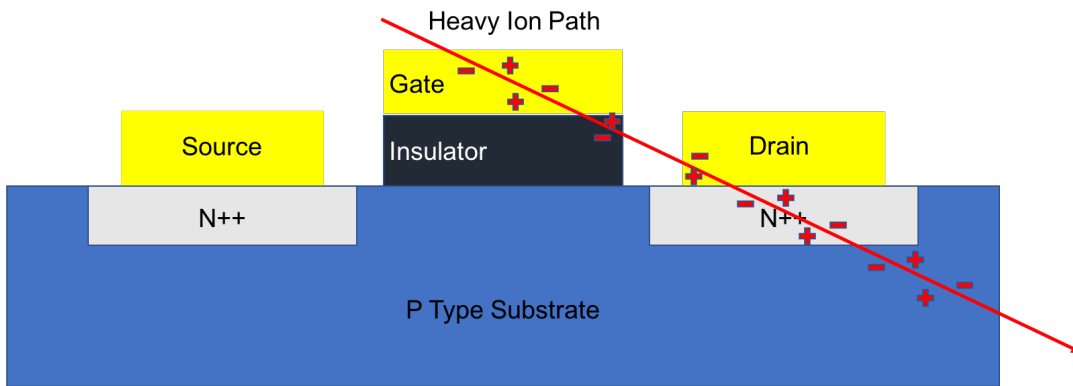
Figure 1.4 Heavy Ion Path in a n-type MOSFET, showing ion track through metal gate layer, insulator and metal drain, as well as the substrate layer.

To prevent or mitigate heavy ion radiation upset to electronic devices in space, three traditional approaches are used: shielding, commercial parts in redundant and duplicative configurations, and electronics hardened for radiation and environment exposure by fabrication of the oxide layer with minimal hydrogen traps ($< 10^{18}/cm^3$) [23, 24, 25, 26].Shielding such as the 14lb lead water cooled clamshells required for missions to Jupiter and redundant circuits are not practical for LEO spacecraft in the SmallSat through MicroSat classes. Nanomaterial enabled devices, especially nanowire-based FETs, are promising because their operating principles are different. NanoFETs use Schottky barrier modulation instead of

channel modulation to achieve ON/OFF functionality [27]. Furthermore, reported investigations indicates that the nanowire channel is largely decoupled from the oxide layer [28]. However, heavy ion radiation studies of nanowire and nanowire-metal contacts are difficult and incomplete, and the in-depth understanding of electron transport mechanism through the nanoFET are still ongoing as well. The results of this thesis are among the first and most accurate to date that address these issues. On a broader scale, the results in this thesis provide guidance for multiple Schottky-barrier driven nanoFET devices including those based on silicon [29], silicon carbide(SiC) [30], cadmium selenide (CaSe) [31] and others.

1.7 Metal-Semiconductor Contacts: A Schottky Barrier and its role in NanoFETs

When metal makes contact with a semiconductor, a barrier is formed at the metal-semiconductor interface. This barrier is responsible for controlling the current conduction as well as its capacitance behavior. In the case of the GaN nanoFET investigated in this thesis, this barrier dominates the current transfer characteristics in the system, hence a brief discussion and review of a Schottky barrier is provided below.

In an ideal case, when a high work function metal is connected to a semiconductor across a sharp junction, charge will flow from the semiconductor to the metal to reach equilibrium. As the result of electron movement, the Fermi level of the metal and the semiconductor will align, relative to the Fermi level in the metal. The Fermi level of the semiconductor is adjusted (lowered for n-type and increased for p-type) by the difference between the two work function. The work function is the energy difference between the vacuum level and the Fermi level [32].

A barrier is then formed, and the height of the barrier is defined as the difference between the metal work function and the electron affinity (the energy gap measured from the bottom of the conduction band to vacuum level) of the semiconductor. When the barrier has a

wide depletion region in the semiconductor that prevents most tunneling, a Schottky barrier exists. A Schottky barrier with a narrow depletion region that can be bridged by tunneling through the barrier is called Ohmic contact [33].

However, extensive measurements using photoemission spectroscopy indicate that Schottky-barrier formation is due mainly to defects generated near the interface by deposition of the metal [32], for most III-V compounds. In this case, the barrier height is essentially independent of the metal work function.

In the most common application of Schottky barrier as Schottky diodes, an n-type semiconductor formulated Schottky barrier is used to modulate the current transport in the device. Similar to a pn junction, when under forward bias, the thermally excited electrons are able to pass the barrier from semiconductor to metal causing current flow and this corresponds to the ON state of the device. When under reverse bias, the barrier height is increased to the point that prevents majority carrier to pass through, and this corresponds to the OFF state. Minority carriers as well as tunneling can also influence Schottky barrier transport under the right conditions [32].

Tunneling as a significant but not dominant contribution is referred to as Thermionic Field Emission (TFE). This is a physically realistic but mathematically challenging configuration, furthermore, ample evidence suggests that TFE becomes the dominant Schottky barrier transport mechanism when contact areas become nanoscale. This is investigated in chapter 3 of this thesis for the case of GaN nanoFETs.

1.7.1 Schottky Barrier modulated NanoFETs

In the earlier part of this introduction, I have discussed how radiation, especially SEE heavy ions, can impact traditional MOSFET architectures based on the silicon native oxide structure. One of the main disadvantage of such a device is that the on/off threshold is dependent on the insulating oxide layer which enables the gate field effect operation. This is the fundamental design and operation of the device and current technology has not found a solution

for space applications other than using a radiation hardened oxide layer that is susceptive to penetrating heavy ion damage, using shielding from the radiation source or using redundant design, none of which are applicable for CubeSat missions.

NanoFETs on the other hand, have been shown to operate as barrier modulated devices. In recent experiments with carbon nanotube based nanoFETs (NT-FETs), whenever there is a substantial Schottky barrier (SB) at the contact, NT-FETs operate as unconventional Schottky barrier transistors, in which switching occurs primarily by modulation of the contact resistance rather than the channel conductance. The gate induces an electric field at the contact, which controls the width of the barrier and hence the current. A sharper contact leads to focusing of the electrical field, allowing operation at lower gate voltages. Changes in work function, e.g. by adsorbed gases, affect the Schottky barrier and hence the device characteristics [32].

Further reported results indicate that the nanotube/nanowire conductance channel is largely decoupled from the oxide [34]. This lack of capacitive coupling implies that even if radiation damage is present in the oxide layer, its impact on the device may be minimal. These two fundamental difference between traditional MOSFETs versus NanoFETs, contact modulation and oxide decoupling make NanoFETs the ideal electronic setup for CubeSat missions in LEO. The possible ability to control current transport solely at the contacts by barrier modulation drives one of the main interests in this study, if the contacts and the nanowire (channel) themselves can survive radiation, then NanoFETs can indeed provide beyond traditional MOSFETs performance in a much smaller package without radiation shielding. The NanoFET setup used in this thesis is shown in figure 1.5 below.
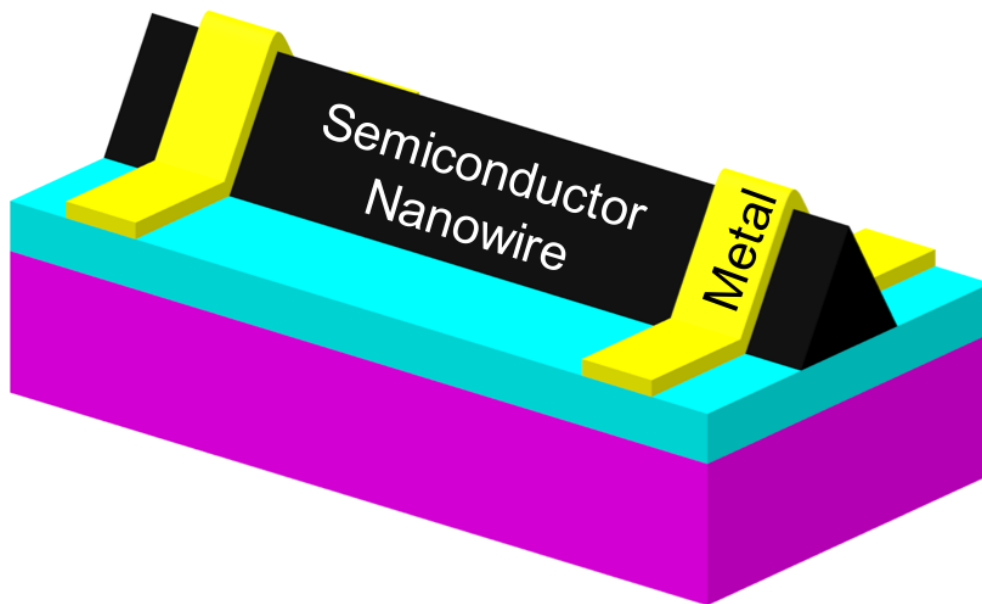
Figure 1.5 A demonstration drawing of the NanoFETs device setup used in this thesis, showing the isolated channel.

1.8 High energy heavy ion radiation studies of Gallium Nitride Devices

Chapter 3 in this thesis focuses on GaN nanowire based NanoFETs, GaN nanowires and GaN nanowire-based devices have been one of the unique and first known experiments pioneered by the candidate's lab. Information and results leading to the study topics of thesis are provided below, beginning with the simple question of why gallium nitride.

For many years, silicon has been at the heart of the vast majority of semiconductor devices. Now, however, wide-bandgap III-Nitrides have also become one of the most important semiconductor materials systems, with applications in visible- UV light emitting devices (LEDs) and laser diodes (LDs), high- power/high frequency transistors and power rectifiers [35]. Especially in the world of power electronics, GaN is replacing silicon as the material of choice for power transistors in industrial automation, motor drivers, high-frequency dc-dc conversion, and similar applications due to its superior performance over silicon in power applications. GaN has bandgap energy or 3.4 eV, compared to 1.1 eV for silicon. The wider

bandgap energy gives GaN power transistors a number of advantages[35], including:

1. Lower gate capacitance and output capacitance for higher switching frequency with lower switching losses.

2. Higher efficiency, resulting in lower conduction and switching losses, and low or zero reverse recovery losses.

3. Lower RDS(on) (Drain-source on resistance) for higher current operation.

4. A smaller footprint for higher-power-density designs.

These large body of work therefore supports, the idea that GaN can work as transistor building material. In the scope of this thesis, the study is focused on the unique application of GaN nanowires in a radiation environment. Directly comparable research work is very limited and hard to achieve and analyze, but one can gather some information based on studies of SEE in GaN high electron mobility transistors (HEMTs) which have been reported.

Single event upsets include both soft errors and hard errors. A soft error occurs when a heavy ion strikes a semiconductor substrate, creating electron-hole pairs, and charge collects at nodes in the circuit, resulting in transient signals. Sometimes catastrophic failures, or hard errors occur when a heavy ion strikes a sensitive region in the device and permanently causes increased leakage current or renders the device inoperable.

The effects of single event particle strikes in GaN HEMTs have only recently been investigated [36]. Bazzoli et al. [37] were the first to study SEEs in GaN HEMTs. They reported soft errors using heavy ions (Fe, Br, Xe) with linear energy transfer (LET) up to $39 \text{MeV.mg}^1.\text{cm}^2$ identified as temporarily increased gate leakage current. This would be classed as soft damage. This work also reported catastrophic failures using Xe ions at a LET of $60 \text{ MeV.mg}^1.\text{cm}^2$, ie. the device can be destroyed with only one interaction with an ion. These phenomena appear to be similar to single event gate rupture (SEGR), despite a lack of gate oxide. No single event burnout (SEB) could be induced. The same HEMTs

were unaffected by 14 MeV neutron irradiation and heavy ions with LETs of 1.8 and 18.5 MeV.mg^1.cm^2.

Kuboyama et al. [38] reported several different types of permanent damage in Al-GaN/GaN HEMT devices irradiated with Kr, Ne or Ar heavy ions from an accelerator at fluencies up to 10^8cm^2 GaN HEMTs using heavy ions. They observed enhanced charge collection with Ne ions and increased leakage current with Ar and Kr ions. A new damage mode, which introduced the leakage paths between the drain and source, was observed with Kr ions at high drain voltages [38] and also new leakage paths emerged between the drain and source terminals without any damage signature to the gate.

Rostewitz et al. [39] evaluated the Single Event Burnout (SEB) and SEE of HEMTs under DC and RF operations during high energy Ar, Xe or Kr ion irradiation. They found that SEBs are correlated to enhanced Single Event Transients (SETs) close to the gate region and that no SEBs occurred under RF operation. Onoda et al. [38]showed the drain currents increased when relative high energy Ni ions impacted the gate electrode and demonstrated that 18 MeV-Ni ions can cause positive charge buildup in the AlGaN layer even at room temperature [39]. The drain current did not increase when ions struck the HEMT other than at the gate electrode. Since there was no charge buildup in the AlGaN layer when ions traversed any region other than the gate electrode, only back-channel effect contributed to the enhanced charge collection. The largest charge enhancement was found when 18 MeV-Ni ions impacted the center of the gate electrode in the pinch-off bias condition due to an enhanced charge collection [38]. The key point of the back-channel effect is the positive charge accumulation in the GaN layer under the gate. The positive charges reduce the potential barrier between the source and the channel, resulting in the current from the source to the drain. A decrease in the saturation drain current and a positive shift of the threshold voltage were observed as a result of the relative high energy Ni irradiation [38] and the transient drain and source currents were strongly affected by the change in I-V characteristics caused by displacement damage. There were two different failure modes, namely increased drain

and gate leakage at high drain voltage, and SEB using drain voltage of 155 V and particle LET of 48 MeVmg^{1}cm^2.

Scheick [40] examined the susceptibility of enhancement mode GaN HEMTs to heavy ion induced SEE. This study noted that the susceptibility to SEE was dependent on ion type, angle, circuit capacitance and manufacturing lot. These preliminary results suggest GaN transistors are less vulnerable to single event burnout than Si MOSFETs. In AlGaN/GaN MOSHEMTs, simultaneous charge collection was observed at the gate and the drain or the source, depending on strike location. Heavy ion data coupled with device simulations show that the introduction of a thin HfO_2 layer in the gate stack introduces only a small valence band barrier, reducing but not preventing collection of holes at the gate in HfO_2 gate devices. Furthermore, using Al_2O_3 gate oxide increases the valence band barrier over that of the HfO_2, to the point where the radiation-induced transient is not detectable. Analysis of the band structure of the HEMT using simulations showed that hole collection at the gate is favorable under off-state conditions, even for devices with an HfO_2 gate dielectric while use of an Al_2O_3 dielectric produced a valence band barrier that reduced hole collection to a level below the resolution of the test setup[40]. This suggest that device design will be important in reducing the susceptibility of GaN-based MOS transistors to SEE.

These results are summarized in Table 1.2

1.9   Previous Work Done by Our Group

When it comes to heavy ion radiation studies of Carbon Onions and GaN nanowires and NanoFETs, the candidate′s group has pioneered research in these areas. Here the review is on the previous work that has been done which leads to the research work in this thesis.

Table 1.2 Summary of Previous work on GaN Radiation

Material	Ions	Energy	Source	LET $(MeV * cm^2/mg)$	Range (μm)	Reference
GaN	N Fe Br Xe	139(Ni) 523(Fe) 236(Br) 1217(Xe)	SAMES, CEA Valduc, France. TRI-UMF, Van-couver, Canada	1.3(Ni) 14(Fe) 32(Br) 47(Xe)	202(Ni) 97(Fe) 31(Br) 89(Xe)	SEE Sensitivity of a COTS GaN Transistor and Silicon MOS-FETs
AlGaN/GaN	Ke Ne Ar Xe	74(Ne) 147(Ar) 315(Kr) 443(Xe)	Japan Atomic Energy Agency (JAEA)	4.9(Ne) 11.8(Ar) 30.6(Kr) 52.9(Xe)	21.3(Ne) 20.0(Ar) 20.09(Kr) 19.9(Xe)	Single-Event Damages Caused by Heavy Ions Observed in Al-GaN/GaN HEMTs
AlGaN/GaN	Ar8+ Kr17+ Xe26+	316(Kr) 459(Xe)	The Heavy Ion Facility (HIF) in Louvain la Neuve, Belgium	13(Ar) 31(Kr) 48(Xe)	16.9(Ar) 16.4(Kr) 15.4(Xe)	Single Event Effect Analysis on DC and RF Oper-ated Al-GaN/GaN HEMTs
AlGaN/GaN	Ni	18(Ni)	Focused Ion Beam	N/A	N/A	Enhanced Charge Collection by Single Ion Strike in Al-GaN/GaN HEMTs

1.9.1   Structural studies of Gallium Nitride Nanowires

The GaN nanowires examined in this study were synthesized by a catalyst-free direct reaction of gallium vapor and ammonia [41]. Nanowires with two orientations were obtained using this growth method, which depended on the furnace growth temperature. At furnace growth temperatures between 850 and 950 °C, multiphase zinc blende/wurtzite GaN nanowires with triangular cross sections ranging between 60 and 150 nm in width, were commonly obtained. The growth orientation was along the 011 direction for zinc blende and the $2\bar{1}\bar{1}0$ direction for wurtzite. At 1000 °C, single-phase wurtzite GaN nanowires with hexagonal cross sections, ranging between 200 and 5000 nm in width, were commonly obtained. The single-phase wurtzite growth orientation was along the [0001] direction.

1.9.1.1   GaN nanowire grown at 850 °C and 950 °C

In this early study, evidence for a new biphasic crystalline homo-structure in GaN nanowire was found based on the analysis by cathodoluminescent (CL) and High Resolution Electron Microscope (HRTEM) with Selected Area Diffraction (SAED), Fast Fourier transform (FFT), Energy-Dispersive X-ray Spectroscopy (EDS), and Electron Energy Loss Spectroscopy (EELS). An inner wurtzite phase and outer zinc-blende phase crystal homo-structure with a sharp phase transition of ∼1- 3 atomic layers seemed apparent under TEM. Core-shell structures were thought to be represent a new class of electron waveguide structures with important applications in quantum transport at the time [42]. However, later studies with a Focused Ion Beam (FIB) system used to produce nanowire cross-sections that were analyzed using HRTEM proved that these nanowires were not core-shell biphasic. Instead, novel multiphase gallium nitride nanowire internal structure, with multiple zinc-blende and wurtzite crystalline domains that grow simultaneously that extend along the entire length of the nanowire, was identified. Coherent 0001 /111 interfaces between the zinc-blende and wurtzite phases were identified, and were assumed to be responsible for the structural

stability [43, 44].

1.9.1.2   GaN nanowires grown at $1000\,°C$

The cross-section studies for nanowires and grown at $1000\,°C$ revealed hollow core screw dislocations, or nanopipes, in the nanowires. The hollow core was located at or near the center of the nanowires, along the axis of the screw dislocation.

The observations were carried out in cross section with the electron beam parallel to the Burgers vector. Experimental evidence in two different nanowire systems obtained using complementary parallel and perpendicular TEM investigations strongly suggested that axial screw dislocation mechanisms may be an important aspect of nanowire formation at this growth temperature should be investigated for many nanowire material systems. If confirmed as a general trend, axial screw dislocation mechanisms, with the possibility of hollow core formation, can significantly impact nanowire device design [45].

1.9.1.3   Electronic Studies of GaN Nanowires

Further studies reported two- and four-point probe investigations of the GaN $850\,°C$ nanowires acquired using tungsten nanomanipulator probes during real-time SEM at the Zyvex corporate laboratory in Richardson, TX. These were the first two- and four-point probe reported for a zinc-blend wurtzite GaN nanowire system [44]. I-V characteristics were consistent, in each case indicating Schottky barrier formation at the Ti/Au-nanowire and probe-nanowire contacts. The current densities measured for the $850\,°C$ nanowires were very high, which was consistent with other published findings. A localized nanowire melting was observed as current was increased to the point of device failure during the two-point probe experiments, which might have indicated possible phase specific transport. This point remains under investigation [42].

The I-V characteristic behavior of a three-terminal GaN NanoFET was investigated sep-

arately. Electronic transport investigations found a consistent power law dependence that indicated possible space charge limited current dominance during injection into the multi-phase GaN nanowire system. However, carrier injection into nanowires was not explained at a fundamental level during these investigations. The present thesis contributes key results that address this area.

1.9.1.4 Combined Studies of Structural, Radiation and Electronic Behavior of GaN Nanowires

Early experiments investigated the heavy ion radiation response of 850 °C GaN nanowires and a GaN NanoFET to heavy ion irradiation, specially to Krypton-86. The majority of the GaN nanowires examined did not show strong evidence of radiation coupling. However, two GaN nanowires did show evidence of radiation interactions that resulted in the creation of plumes of material along the nanowire surface. All plumes investigated showed strong concentric ring patterns in corresponding FFTs, indicating amorphous material. However, no propagation or accumulation of defects at the internal zinc-blende/wurtzite interfaces were observed. Another type of nanowire surface feature resembling gouges was sometimes observed. FFTs of the gouges and their adjacent areas indicated largely crystalline material. As gouges were sometimes also been observed in non-irradiated GaN nanowires [46], this type of feature was not attributed to radiation interaction at the time but remains under investigation.

The I-V performance of a three-terminal GaN NanoFET under Krypton-86 irradiation was also investigated as a series of time points (irradiation stopped briefly while measurements were acquired). These early results were promising as they indicated good nanocircuit resilience to heavy ion radiation.

1.10 Quantum Communication SAW Device in Space

The third investigation in this thesis is a recent contribution to the area of CubeSat telecommunications, a vital part of the CubeSat architecture.

The CubeSat missions of today have enabled new data collection and analysis opportunities that are re-writing current understanding of terrestrial geospace and atmospheric conditions [47]. The CubeSat missions of tomorrow will play a vital role in guiding extraterrestrial planetary insertions around Mars, Jupiter, and their satellite moons. CubeSat architectures are challenging, with great emphasis on technical ingenuity and feasibility. The significant degree to which they advance and make use of emerging technologies while demonstrating satisfactory technological readiness or heritage is considered vital to their success stated in the NSF 2013 CubeSat Annual Report [48].

The current challenge of providing uplink/downlink/onboard communication via secure channels may be significantly improved using an emerging technology: solid state quantum communications. Quantum communications refer to communication systems that are based on quantum entanglement. Quantum entanglement may be realized using laser-based, atomic gas and solid-state designs; however, solid-state implementations are highly desirable for CubeSats given their space, mass, and thermal management restrictions. A role for CubeSats as secure nodes is envisioned [49].

1.10.1 Quantum Communications

Quantum communications refer to communication systems that are based on quantum entanglement. Quantum entanglement is a physical phenomenon that occurs when pairs or groups of particles are generated or interact in ways such that the quantum state of each particle cannot be described independently of the others. Even when the particles are separated by a large distance instead, a quantum state must be described for the system as a whole [50].

The once-controversial idea that electrons have wave-like properties and that photons have particle-like properties is now well documented experimentally. Superposition of wave-like electrons underlies practical applications such as electron diffraction. The quantum state of a single electron refers to its description regarding quantized (i.e., integer counting) of fundamentally conserved variables energy (n), angular momentum (l), the projection of angular momentum (m) and spin (s). An electron is therefore described as a wavefunction Φ_{nlms}, which is a solution to a wave equation that describes conservation of energy for the physical system. Additionally, Φ_{nlms} satisfies relationships for the conservation of angular momentum, its projection, and the Pauli exclusion principle (spin up/spin down electrons).

Superposition of electron quantum states can involve any of the conserved variables n, l, m, and s. Spin states in electrons, which are binary spin up or spin down, are a target of recent research including the research in this thesis. The novelty, power, and controversy of entanglement in addition to superposition of its prediction of correlated behavior even when the (formerly superposed) particles are separated by a large distance. This implies that entangled electron spin state pairs and their predicted action-at-a-distance correlated behavior can be used as a physical source of 0/1 bits called qubits and used to enable quantum cryptography and secure quantum communications [51].

As previously stated, quantum communications systems based on quantum entanglement may be realized using solid-state and laser-based implementations (in laser systems, polarization states replace spin). Solid-state implementations are preferred whenever space, weight, and power (SWaP) and/or thermal restrictions are vital to operations, while laser-based implementations are preferred for high-speed, long-distance operations. Initial solid-state implementations include investigations of heterostructure-based devices [52], quantum dot devices [53], and superconducting devices [54]. These applications have shown great promise but currently suffer from non-robust qubit generation and significant active cooling requirements [55]. Investigation on dynamic local environments that can enhance entanglement and/or improve coherence times (the time over which an electron spin state is predictable)

25

are therefore of great interest. Surface Acoustic Waves (SAW) have experimentally demonstrated the ability to create a dynamic local environment that confines and transports electrons between quantum dots over a several microns distance [53]. Furthermore, this "flying qubit"approach has been theoretically investigated for entangled electron qubits based on spin states Ref [56]. As stated in Ref [56], there is only an incomplete understanding of the mechanism by which electrons are captured and transported. This capture process is intrinsically time-dependent; it involves the Coulomb interaction between many particles; and includes quantum-mechanical confinement, tunneling, coherence and transport issues.

1.10.2 Design for SAW-based Quantum Communication System

A "flying qubit "design for an ideal heterostructure-based 1D channel was explored in Ref. [52] and found to be viable; however, many details of the interactions between the dynamic potential induced by propagating SAW wave with electron spins in a reduced dimensionality situation were not investigated. One key aspect not previously reported is that a SAW wave consists of a longitudinal as well as a transverse component. In the present work, the focus is on the effects of the interaction of a SAW wave longitudinal component with a reduced dimensionality electron pool produced at the interface of a GaAs-AlGaAs heterostructure with a further reduction to a one-dimensional electron channel via fabrication of a split-gate. Early results indicate that such structrure can significantly influence both transport uniformity and transmission. Furthermore, the present analysis is developed for a realistic finite width 1D channel.

1.11 Summary of Research Contributions

The thesis work of Kan Xie presents the study of nanomaterials and devices that can be implemented within small spacecraft systems that operate in space environments. This work covers three advanced nanomaterials and nanomaterial-enabled device architectures

that show promise for applications in small spacecraft systems [57] .

The first part of this thesis work is related to the study of carbon onions as a promising candidate for solid lubricant for spacecraft systems. Moving forward from the good high vacuum performance shown by the previous studies, my work demonstrates the effects of heavy ion interactions with this unique carbon system. The results here represent some of the first heavy ion radiation study in this area. The interconnection between stored mechanical energy, and observed structural transformations is also investigated with a possible mechanism is given and discussed.

The second part of the thesis is focused on the analysis of a unique data set that is the only known record of real-time NanoFET I-V performance while running for 30 minutes under heavy ion irradiation at the NSCL at MSU, which accurately simulates the heavy component of space radiation. This experimental and theoretical investigation provides unique insights on how radiation affects electronic properties and performance of NanoFETs, which are candidates for small satellite electronics. Furthermore, this study enables a new look at how nanoscale contact barrier modulation is affected by radiation as well.

Prior to this study, carrier transport through the Schottky barrier that provide device modulation was mainly modeled by thermionic emission concept for a semiconductor-metal Schottky barrier set-up [58]. However, this approach did not explain the observed high diode ideality factor or consider the possibility of transport by tunneling which several reports indicated are present for nanoFET architectures. The work in this thesis demonstrates the exact electron transport mechanism and implements a full metal-semiconductor-metal [32] structure analysis along with the thermionic field emission model [59] to generate the first mechanistic understanding of how NanoFETs may behave in space. Another key part of this work was the development of a new mathematical stability approach needed to enable the evaluation of the multivariate TFE parameters at Schottky barriers. The method is general, requiring only the effective mass and relative dielectric constant for a given semiconductor.

The combined [stability + TFE + MSM] approach produced the first-time analysis of

the barrier heights, tunneling probabilities and potential drops for changes in the Schottky barriers of GaN NanoFETs in a long-duration heavy ion radiation extreme environment. This investigation yielded fundamental insights into behavior that would be challenging to predict a priori.

The third part of this thesis is devoted to early work on a concept quantum communication relay based on the SAW (surface acoustic wave) device as a qubits carrier. Qubits or entangled two-states are the basis for quantum communications as well as quantum computation. Qubits can be generated in multiple electronic and photonic mediums [60, 61]. However, the critical problem with current state of the art is that the coherence of an entangled state during transport is easily comprised by scattering interactions [62]. In this thesis, quantitative investigation of the flying qubit approach [52] is presented. A "flying qubit" provides additional and dynamic confinement, achieved through use of a SAW carrier device.

A SAW device [63] built for quantum communication relay is designed, fabricated and tested in this thesis, shown in Figure 1.6. The work done here is to provide the preparatory step to construct a quantum communication relay for CubeSats investigation in the near future.
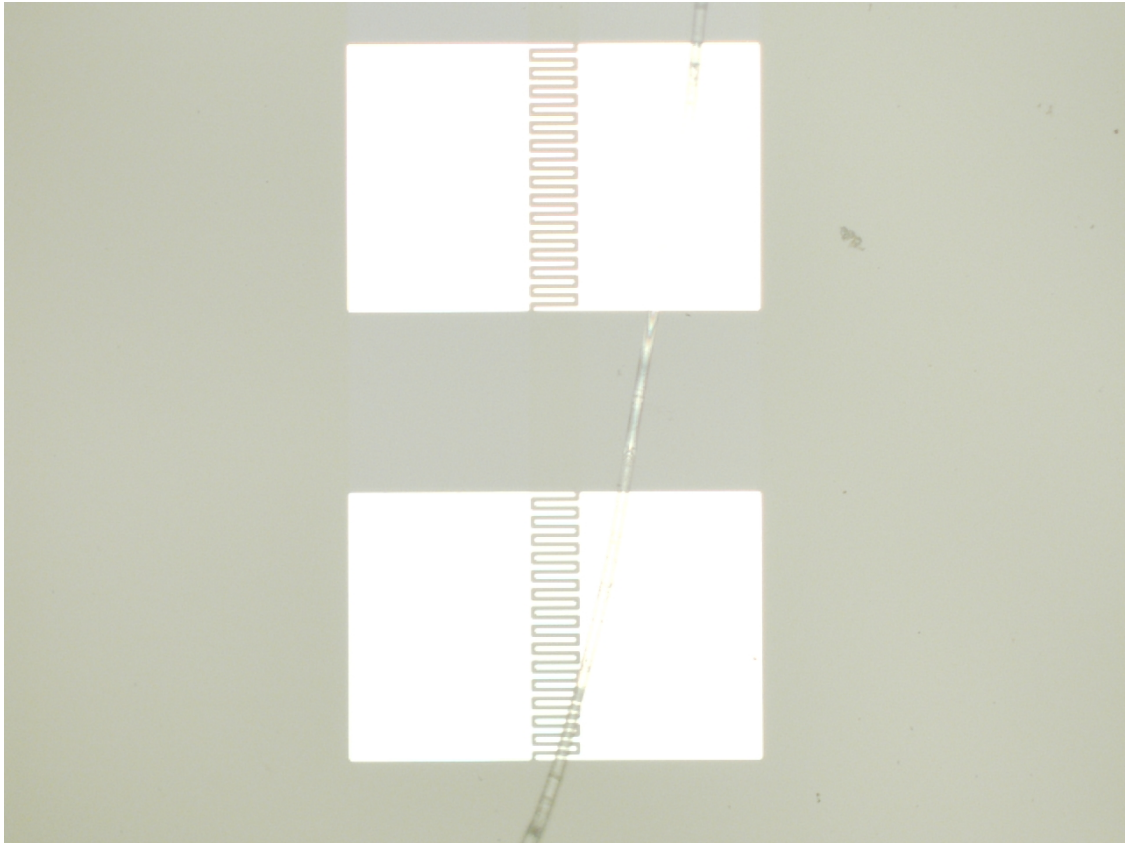
Figure 1.6 One of the fabricated SAW device under microscope. 12 devices were fabricated on the same wafer.

1.12 Dissertation Outline

This thesis reports three key investigations in Advanced Nanomaterials and Devices for Space Applications, structured into four Chapters that follow the timeline of the research. Following this introductory chapter, chapter 2 starts with the study of carbon onions under heavy ion radiation with application targeting to solid lubricants in space. Chapter 3 focuses on the data analysis and modeling of GaN nanoFETs under heavy ion radiation. The design and fabrication of a SAW-based quantum communication relay is then presented in chapter 4. The thesis work and its contributions are summarized in Chapter 5 and future works in the areas are identified.

CHAPTER 2

RADIATION STUDY OF NANO-CARBON FOR SPACE LUBRICANTS

2.1 Introduction

Use of Nano-carbons is a promising new approach to resolve space-based lubrication challenges [64, 65, 66]. As discussed in the introduction of this thesis, nano-carbon lubricant materials including carbon onions [19] and carbon nanotubes [51], have shown robust performance in vacuum environments [65]. Hence, these materials are under investigation as nano-property enabled solid lubricants that maintain performance in space environments.

Research at Tokyo Institute of Technology has investigated the vacuum tribological performance of nano-carbons including carbon onions (multi-wall concentric shells), C60 (buckyballs) and multi-wall carbon nanotubes with graphite and vapor grown carbon fibers investigated as controls. The results are summarized in Table 2.1 below. The best vacuum tribological performance was achieved with carbon onions, and the second-best performances was achieved with multi-walled carbon nanotubes (MWCNT). In this study, C60 films displayed evidence of aggregation, leading to film discontinuities and lubrication failure. Similar aggregation issues is have been reported for single walled carbon nanotubes [67]. Theoretical and experimental work also indicates that nano carbon materials have high tolerances for thermal stress [19]. Therefore, CO and MWCNT have immense potential as solid lubricants in space and particle collider applications if they also display radiation resiliency. In these thesis, the work is focused on the study of irradiation effects on carbon onions as the most promising candidate.

Carbon onions were supplied by Tokyo Institute of Technology for heavy ion investiga-

Table 2.1 Carbon Lubricants Performances in Air and Vacuum [19, 68]

Friction Coefficient	Carbon Onions	Carbon Nanotubes	C60	Graphite	vapor grown carbon fibers (VGCF)
Air	0.1-0.2	0.5	0.5	0.2	0.5
Vacuum	0.04-0.06	0.2	0.6	0.6	0.2

tion with pre and post radiation characterization by high resolution transmission electron microscope (HRTEM). The responses of carbon onions to heavy ion irradiation were investigated at the National Superconducting Cyclotron Laboratory (NSCL) at Michigan State University. The heavy ions used in these experiments were primary beams of fully stripped calcium–48, and argon–40 primary beams with 140 or 70 MeV per nucleon kinetic energies. Evidence was found suggest that multi-layer carbon onions respond to heavy ion irradiation with linking of neighboring concentric graphene layers rather than by amorphization generated via knock-on collision. A possible mechanism based on dislocation migration [69] is discussed.

2.2 Material and Methods

2.2.1 Synthesis Conditions

Three sets of carbon onion samples were synthesized at Tokyo Institute of Technology from crystalline diamond nanoparticles having an average diameter of 5 nm. The diamond nanoparticles were heated in inert ambiance in an infrared gold image furnace. A graphite holder filled with 10 mg of diamond nanoparticles was placed inside the furnace, which was evacuated to approximately 1.3 Pa with a rotary pump, and slowly heated in argon gas flow at 1.5×10^5 Pa to 1700 °C, 2000 °C and 2300 °C, respectively. The furnace temperature was held for one minute and then gradually cooled to room temperature in argon flow. These temperatures in the stated conditions produced the known [70, 71] spherical to polygonal transition of carbon onion morphology as a function of synthesis temperature as shown in Figure 2.1. The carbon onion temperature series enabled investigation of the effects of heavy ion interactions at relativistic energies.
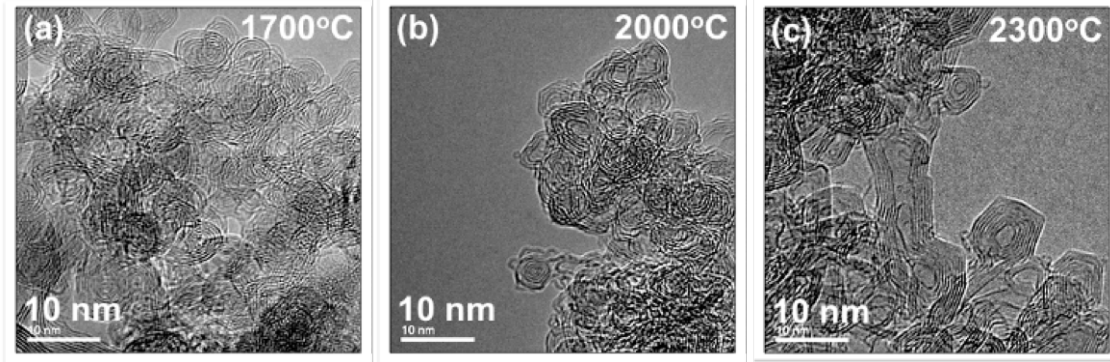
Figure 2.1 HRTEM images of carbon onions synthesized at temperatures 1700 °C, 2000 °C and 2300 °C (a-c).

2.2.2 Irradiation Parameters

As there is no relevant guidance for appropriate dose for carbon nanomaterials in space applications, mid-range charge to mass ratio calcium-48 and argon-40 primary beams with space relevant initial kinetic energies of 140 MeV/nucleon (MeV/u) were used. Irradiation times that resulted in 10,000 Gray (Joule/kg) cumulative total doses for each sample, were selected based on data available from silicon investigations. This dose proved sufficient to introduce structural changes, without causing amorphization. The calcium-48 experiments were also performed with an initial kinetic energy of 70 MeV/u to investigate possible energy time equivalence for the same total dose. For each experiment, the on-target beam energies after passage through a 0.075 mm zirconium (Zr) exit window, a 420-500 mm air gap (exactly measured for each run), and a 0.2 mm quartz coverslip were calculated using the Stopping and Ranges of Ions in Matter (SRIM) Monte Carlo program [72]. After passage through stripper foils and the Zr exit window, almost all ions were fully stripped to +48 and +40 respectively, making these particles highly charged compared to particles from ion implantation or focused ion beam sources.

In each experiment, a beam spot of approximately 2×2 cm^2 was centered using the laser positioning system on a sample that was less than 1 cm in diameter and separated from other samples by at least 5 cm.

The mass of each sample was determined before irradiation using a Denver Instruments M-220D scale with 0.01 mg sensitivity. The approximate area and thickness of each sample were measured with Mitutoyo CD-6CS electronic calipers with 10^{-3} mm accuracy. The experimentally measured dimensions and densities were used in the SRIM calculations to determine the required exposure times to achieve a 10,000 Gray (Gy) total dose for each sample.

2.3 Characterization for Carbon Onion Samples Made with Temperature Variance

HRTEM experiments were performed in a JEOL 2200FS operated at 200 kV. Samples were suspended in ethyl alcohol and dispersed onto carbon lacey film 200 mesh copper grids (SPI). Care was taken to acquire images from samples that were well suspended over holes and not the carbon lacey film. This enabled quantifications measurement on number of layers, layer thickness and polygonal characters which were later used in this thesis to characterize the radiation results.

2.3.1 Effects of 140 MeV/u argon-40 on Temperature Series Carbon Onions

Relativistic heavy ion interactions with carbon onions synthesized at 1700 °C, 2000 °C and 2300 °C, were investigated using a primary beam of argon-40 at 140 MeV/u with an on-target beam energy of 134.0 MeV/u. Increasing polygonal character as a function of increasing growth temperature is a well-known characteristic of carbon onion synthesis. HRTEM images of the pre-irradiation synthesis temperature series reproduced toward the left in Figure 2.2 (a-c). Carbon onions synthesized at 1700 °C were spherical with defective graphene shells, while carbon onions grown at 2300 °C were polygonal with well-defined graphene sp^2 layers connected by sp^3 vertices. This is a general result for CO synthesis as a function of time [19, 3], and was confirmed using EELS by our group for these samples [73].

HRTEM images of the corresponding post-irradiation samples are shown on the in Figure 2.2 (e-f) toward the right. The 1700 °C carbon onions showed an increase in the polygonal character and fusion of adjacent onion pairs (arrow). The 2000 °C carbon onions showed fewer layer breaks in individual graphene shells and an overall increase in polygonal character that caused them to resemble pre-rad 2300 °C carbon onions. The 2300 °C carbon onions showed the greatest variety of rearrangements, with the development of large crystallites of planar graphite, long, 5-7 layer planar graphene ribbons, and occasional amorphous regions. The HRTEM image of Figure 2.2 (f) is an electron transparent corner of a large graphite crystallite.
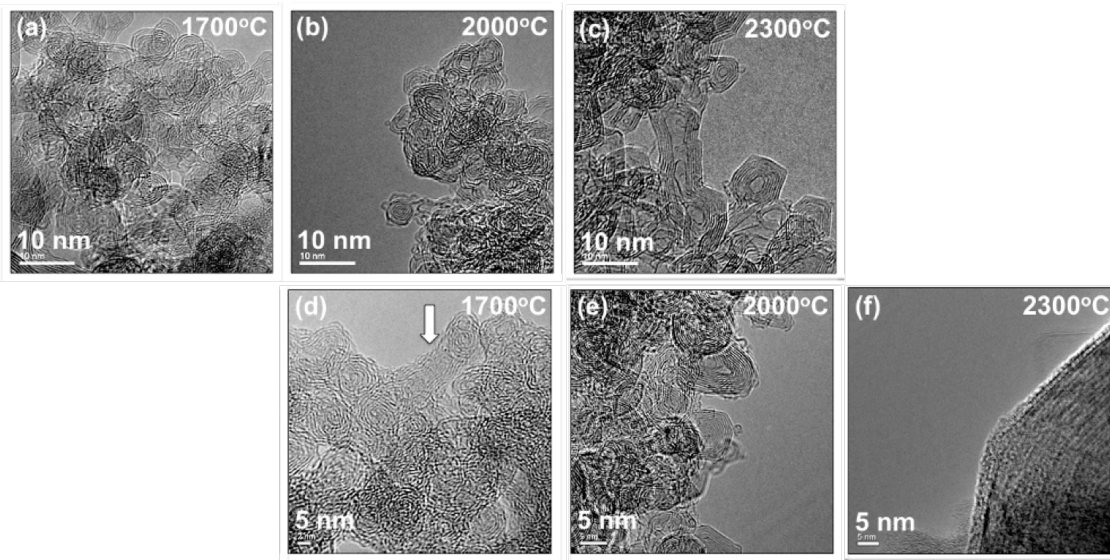
Figure 2.2 HRTEM images of carbon onions synthesized at temperatures 1700 °C, 2000 °C and 2300 °C for (a-c) pre and post (d-f) irradiated by 140 MeV/u argon-40.

2.3.2 Effects of 70 MeV/u versus 140 MeV/u calcium-48 on 1700 °C Carbon Onions

Relativistic heavy ion interactions with carbon onions synthesized at 1700 °C were investigated using a primary beam of calcium-48 at energies 140 MeV/u with an on-target beam energy of 134.5 MeV/u, and also 70 MeV/u with an on-target beam energy of 60.52 MeV/u. HRTEM images of the pre-irradiation 1700 °C and also 2300 °C carbon onions are repro-

duced in the top row of Figure 2.3 (a-b). HRTEM images of the post-irradiation 1700 °C carbon onions are shown in the bottom row of Figure 2.3 (c-d). At both energies, the post-irradiation 1700 °C carbon onions displayed a polygonal structure similar to that observed for pre-irradiation carbon onions synthesized at the higher 2300 °C temperature. 2300 °C series also showed a decrease in the number of layer breaks in individual graphene shells compared to the pre-irradiation 1700 °C carbon onions.
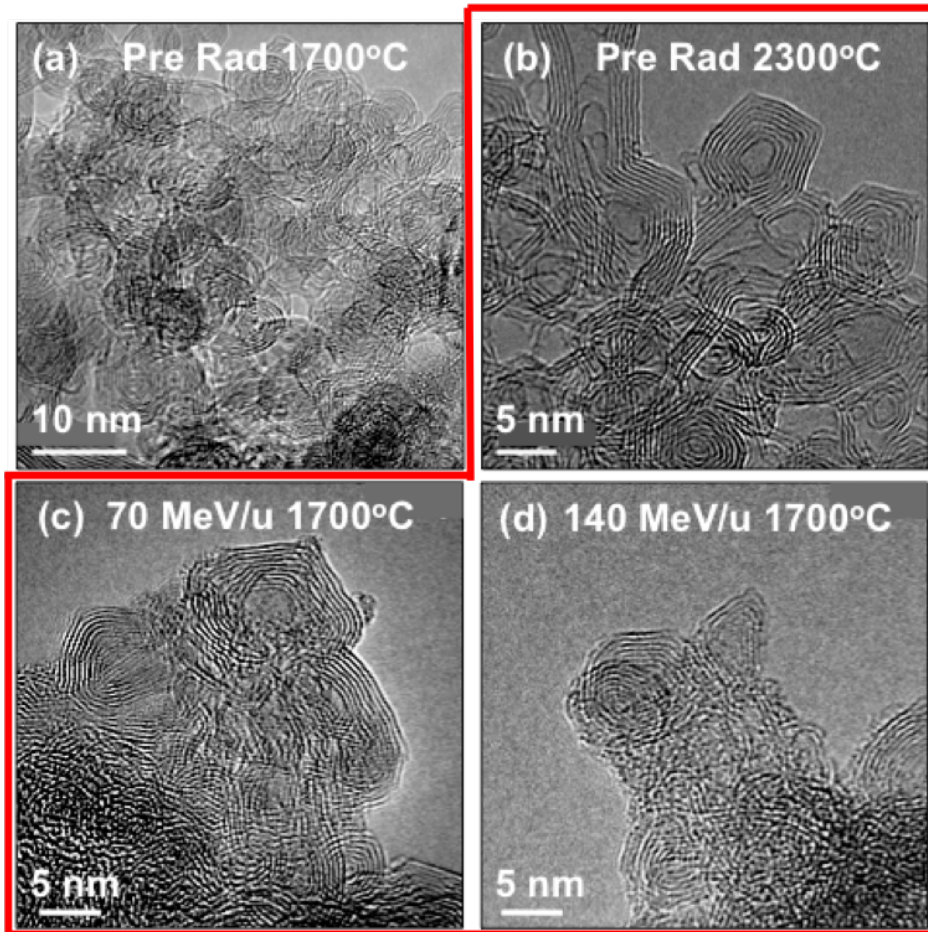
Figure 2.3 Pre-irradiation carbon onions synthesized at (a) 1700 °C and (b) 2300 °C. Post irradiation 1700 °C carbon onions at irradiation energies of (c) 70 MeV/u and (d) 140 MeV/u calcium-48 resemble 2300 °C pre-irradiation carbon onions.

2.3.3 Analyses of Results

Heavy ion interactions with carbon materials are generally assumed to proceed through carbon displacement or knock-on collisions [74]. In planar graphite, displacement collisions result in inter-layer aggregation of displaced carbon atoms into wedges, which eventually force the layers apart causing a local amorphous region [75] as shown in Fig 2.4. However, the anticipated effects of knock-on collisions were not observed in these experiments. The primary impact seen was an increase in polygonal character. Rearrangements such as fused carbon onions, and long 5-7 layer graphite ribbons were also observed. For 2300 °C carbon onions irradiated by on-target 134.0 MeV/u argon-40, a few large graphite crystallites developed in addition to long ribbons and what appeared to be the fusion of many neighboring onions. The number of layer breaks in individual graphene shells appeared to decrease compared to the pre-irradiation structure. By this measure, the post-irradiation arrangements were less defective than the pre-irradiation structures. Additional analyses were therefore performed as part of this thesis to account for the observed differences from the displacement model mechanism.

2.4 Additional Analyses of Carbon Onions Under Heavy Ion Irradiation

2.4.1 Energy Analyses

Monte Carlo SRIM calculations for total energy loss dE/dx, which included calculation of the individual nuclear and electronic interaction contributions, were carried out and analyzed. The results are shown in Figure 2.5. The peak of the nuclear contribution was at 2×10^{-4} MeV/u.

This was far from the beam-on-target 134MeV/u energy. The peak of the electronic contribution coincided with the peak of the total energy loss curve at 1 MeV/u, which indicated that energy deposition was mainly through electronic interactions. This value also
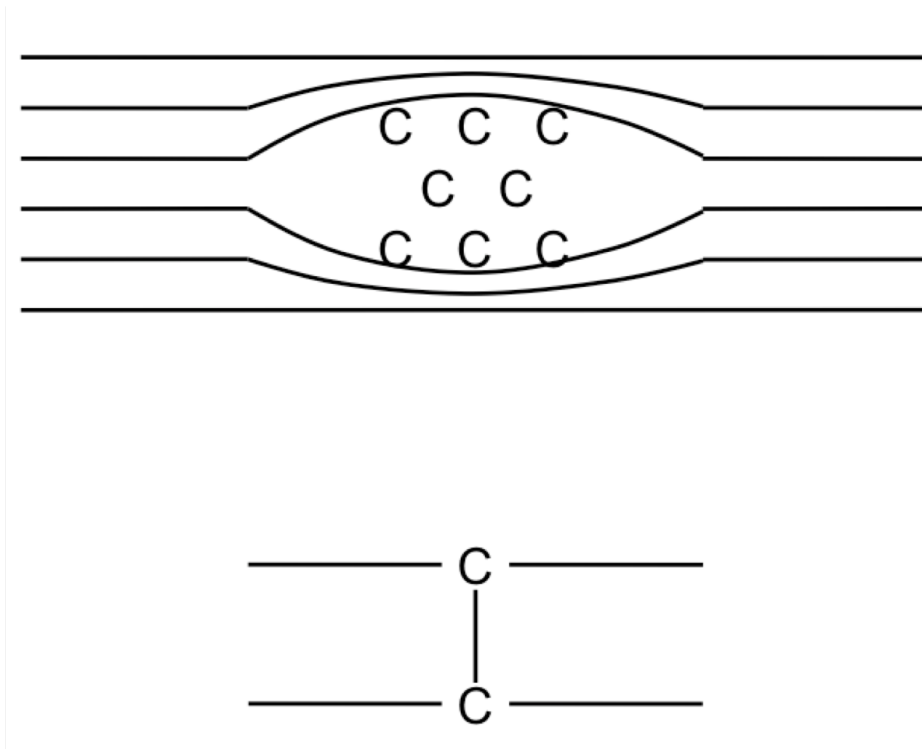
Figure 2.4 Classic knock-on collision creates free carbon atoms and vacanties in graphene layers. These amorphous regions or interstitial aggregates can coalesce to form local spot welds.

was not close to the beam on-target 134 MeV/u energy. The beam on-target 134 MeV/u energy was therefore in the tail of the energy loss curves for both contributions.

2.4.2   Model:Influence of Mechanical Stress

It has also been shown [76] that the addition of a polygonal corner to a spherical graphene shell of average elasticity E requires energy Ep~2 E t^2 (ζ^2/R). In this relationship t is the graphene layer thickness, R is the average radius of the spherical carbon onion equivalent, and ζ is the departure from sphericity measured as the distance between a polygon apex and R.

A study was done by measuring the average values of t, R and ζ using the HRTEM image of the Pre-Radiation Carbon Onion series. Images were post-processed by counting the pixel density of the scale bar, then actual measurement of distance was done by the scale bar vs.
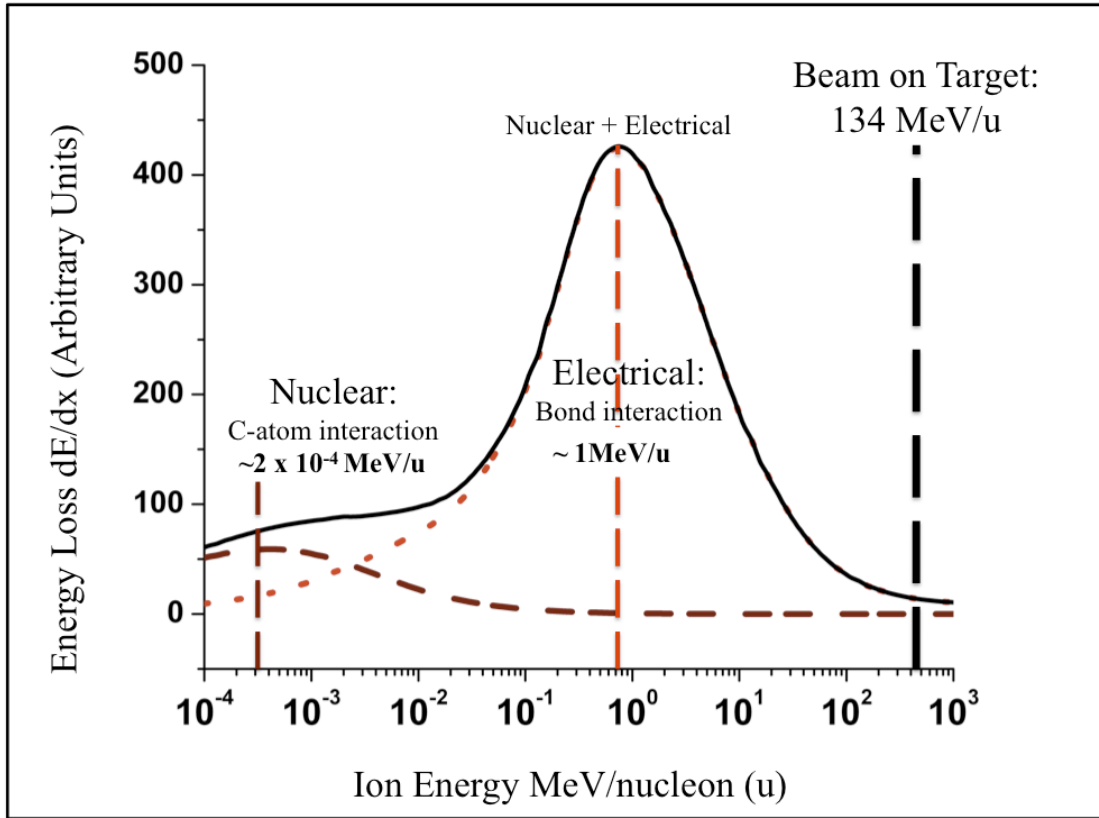
Figure 2.5 Monte Carlo SRIM energy loss calculations showed that the argon-40 heavy ion beam-on-target energies were in the tail regions for both nuclear and electronic interactions.

pixel count ratio.

10 carbon onions were chosen within each set of TEM image of the temperature series, with selection based on the ability to count number of layers clearly in the zoomed in image in post processing, see Fig 2.6. In the case of the two sets of high energy dose post radiation carbon onions with fewer countable specimen (Ar 2300 Post-Rad and Ca 1700 140MeV), 5 carbon onions were used from each set. The number of layers, layer thickness were measured using a scale ruler, the departure from sphericity (ζ)is calculated by taking the difference of maximum axis and minimum axis (radius). t^2 (ζ^2/R) can be then represented as the scaling factor for average elasticity E. Standard error of the mean is also given. Complete data results are shown in Fig 2.9 as a whole page image at the end of this chapter.The summary of these results is shown in table 2.2.

Table 2.2 Summary of measurements for Elasticity E Components (Data in Figure 2.9)

Variable/Spicement	1700 Pre-Rad	2000 Pre-Rad	2300 Pre-Rad	Ar 1700 Post-Rad	Ar 2000 Post-Rad	Ar 2300 Post Rad	Ca 1700 70MeV	Ca 1700 140MeV
Avg.ζ (nm)/STDEOM	0.7061/0.15524693	0.942/0.12512385	1.4025/0.11630183	1.1558/0.22142718	1.5905/0.21435258	1.708/0.21417364	1.1406/0.14550206	1.403/0.13806502
Avg.# of Layers /STDEOM	6.4/0.37118429	5.7/0.3	6.3/0.3	6.3/0.21343747	7.8/0.95219046	7.2/0.41231056	6.7/0.55876849	7.2/0.51961524
Avg. Layer Thickness (nm) /STDEOM	0.3461/0.3285647	0.4535/0.02724182	0.4626/0.03317971	0.4331/0.03092336	0.3791/0.01772409	0.3492/0.01681725	0.4345/0.02394914	0.441/0.02740164
Avg. Radius (nm) /STDEOM	2.5024/0.19652482	2.9225/0.16589308	3.0928/0.17612431	2.6427/0.19578543	3.4322/0.33539204	3.1408/0.26335987	2.787/0.55876849	3.0568/0.28105661
t^2 (ζ^2/R)	0.02386596	0.06244347	0.1361022	0.09481868	0.10592594	0.11326192	0.08812707	0.12523494

As the results indicate, one can observe that as the growth temperature increases, the stored elastic energy increases as well. This is represented by the scaling factor of t^2 (ζ^2/R). One can also discover that the post-radiation number for a lower temperature synthesis onions (1700 °C) are similar to the pre-radiation carbon onion grew at higher temperature (2000 °C). This study indicate that as the radiation dose increase, the carbon onions tend to store more mechanical energy, which reproduces a mechanical property of growth at a higher temperature. Another property that possibly changed was the number of layers. This increase in numbers of layers not consistently the case of all post-rad COs examined, and the average numbers do not show much change. However, individual specimens and increased standard error of the mean value could support this observation.
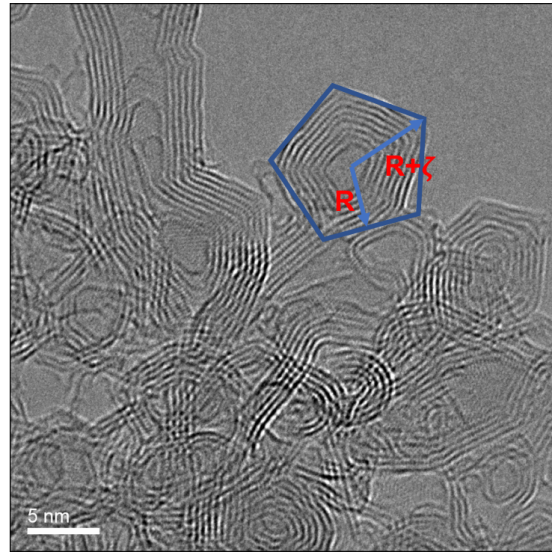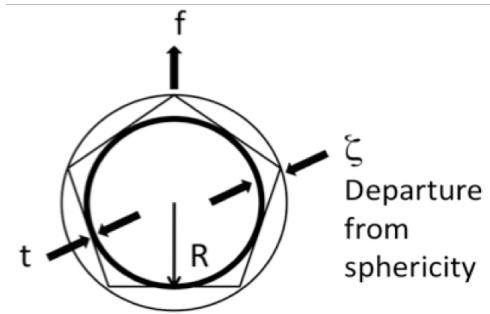
Figure 2.6 Siagram showing the measurement locations for R and ζ with real HRTRM image example.

2.4.3 Thermogravimetric Analysis

The interpretation of a stored energy that increases with increasing polygonal character is further supported by the results of Thermogravimetric Analysis [77] shown in Figure 2.7. A nonlinear increase in ease of dissociation with increasing polygonal character was observed. This was clearly evident when the derivative weight loss was examined. Hatch marks on the temperature axis identity the peak locations, which were increasingly close together. Thermogravimetric analysis was performed using a Rigaku TG8120 in air ambient.
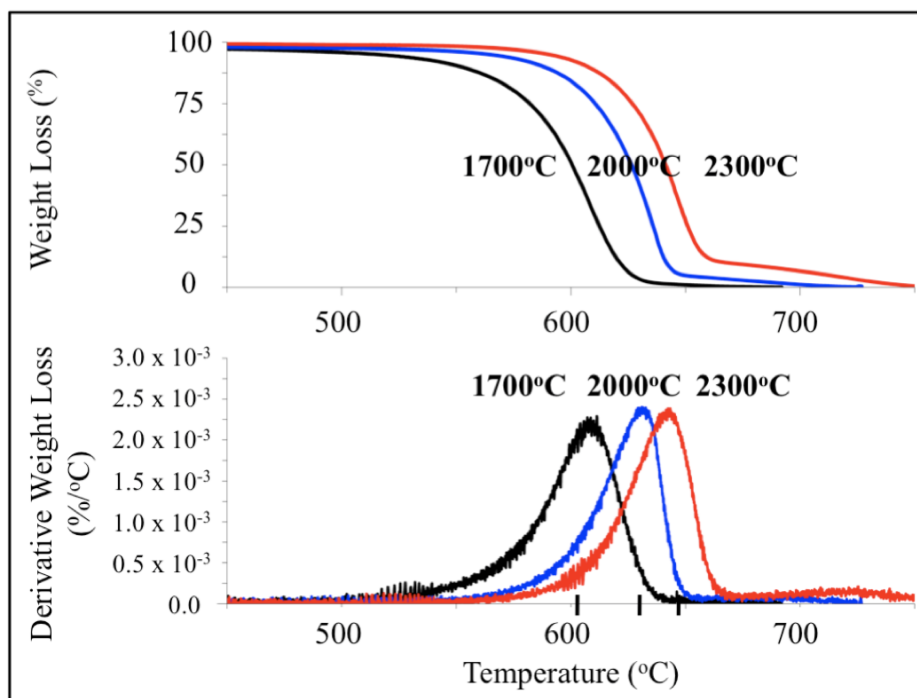
Figure 2.7 Thermogravimetric analysis of pre-irradiation carbon onion samples showed a nonlinear increase in ease of dissociation with increasing polygonal character.

2.5   Possible Mechanism for observed effects of heavy ion irradiation with Carbon Onions

The best-studied model for radiation interactions with graphene is interaction through displacement knock-on collisions between beam particles and carbon atom nuclear cores [78, 79, 80, 81, 82]. This produces dangling bonds and interstitial carbon atoms, which

then rearrange into energy lowering configurations. The following observations have been interpreted using the displacement model: holes in graphene layers manifested as a defective wavy appearance in TEM images, inter-layer spot-welds, and interstitial aggregations of displaced carbon atoms. This model has been mainly studied through interactions of electron beams from transmission electron microscopes with single and multiwalled carbon nanotube samples [83]. However, this model did not match our observations.

A new model for graphene layer rearrangement through zipping, which is driven by dislocation migration mechanisms that are only available in multi-layer radial situations, has been proposed recently [69]. As demonstrated in Fig 2.8, in this model, the migration of an edge dislocation near the outermost shell to the carbon onion core is driven by the imbalances that are inherent in the carbon onion radial geometry when a dislocation becomes mobile. Dislocation migration can result in both the linking and unlinking of large numbers of graphene shells, depending on whether edge plus strain energy, or strain energy alone, is released in each given situation. This model has been studied using the combination of heat administered by a local scanning tunneling microscope tip and interactions with electron beams from a transmission electron microscope with carbon onion samples. The carbon onion samples appeared to be spherical with a slight polygonal character and 15-20 layers thick. The following observations have been interpreted using the dislocation migration model: linking and unlinking of shells that changed the number of observed layers in individual carbon onions.

2.6   Discussion

The energy loss analysis suggested that knock-on collisions, which are nuclear core interactions, were not dominant at our experimental energies. A limited interaction would be expected for large mass heavy ions compared with small mass electrons from electron beams.

The energy loss analysis further indicated that the ion beam energies would not be
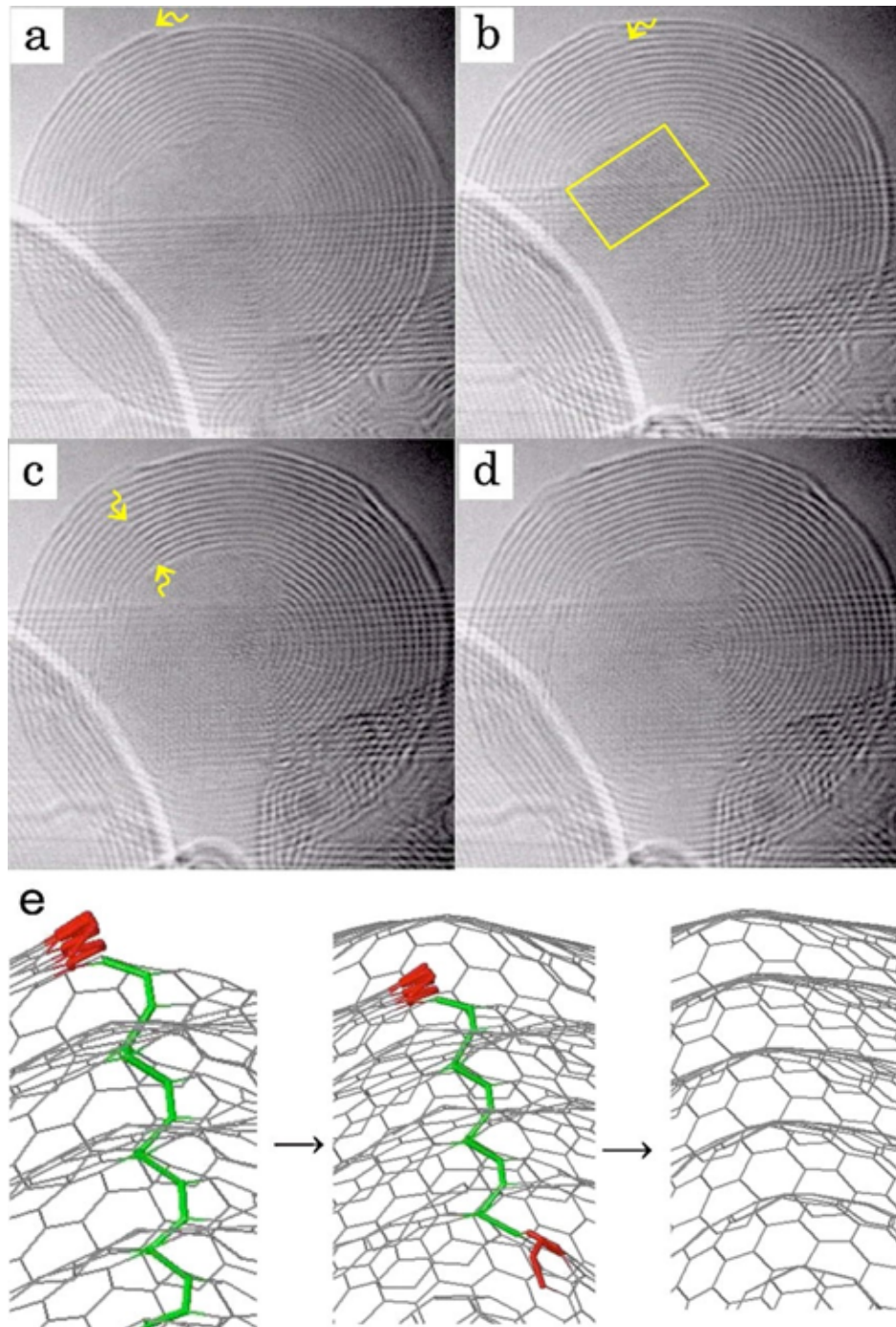
Figure 2.8 (a)-(d) In situ observation of dislocation annihilation. Arrows point out the dislocation edge. In (b), a cubic-diamond region is visible in the highlighted rectangle. (e) An atomic structural model of the annihilation process accompanied by unlinking of the shells. The atoms in dark gray (red) [light gray (green)] belong to the edge [screw] component of the dislocation loop. Image adapted from Ref [69]

expected to generate a strong electronic interaction. Yet the HRTEM analysis showed that with a limited amount of energy transfer, several interactions took place that resulted in distinctive graphene layer rearrangements. Outer layer linking of multiple onions, changes in polygonal character, changed number of layers of graphene shells, and changes from radial to linear graphene layer arrangements were all observed.

These changes seemed to be progressively more radical with the increased polygonal character of the starting sample. The TGA analysis demonstrated a nonlinear increase in ease of dissociation with increasing polygonal character. Recent modeling also indicates that extra energy may have been stored in the more highly polygonal onions [84]. The HRTEM results suggest that energy could be released by radiation interactions to help drive graphene layer rearrangements. A practical conclusion is that the polygonal character of a carbon onion sample should be quantified before any structure-changing investigation [69].

Recent theoretical research indicates that dislocation migration in the multi-layer radial carbon onion system will produce graphene layer linking and unlinking. Our experiments showed evidence of both. Dislocation migration is typically activated at relatively low energies, which also fits well with the results of the energy loss analysis [77].

Energy loss calculations shown in Figure 2.5 indicated that heavy ion interactions including knock-on collisions and also bond ionizations should have been comparatively rare at the 140 MeV/u and 70 MeV/u energies used for the primary beams in the nano-carbon materials investigation. However, the amount of energy required for dislocation migration is much less than the amount of energy needed for knock-on collisions or bond ionization. The present observations of graphene layer rearrangements in an energy regime where little interaction would be expected may be a physical manifestation of the new predicted dislocation migration pathways in multi-layer carbon nanotubes and carbon onions.

Graphene layer rearrangement could have both positive and negative implications for the tribological performance of multi-layer nanocarbons in a heavy ion radiative environment. Ongoing rearrangement into nanocarbon that retained the excellent tribological features of

the originals would be a self-healing way of dealing with radiation-induced defects. However, rearrangements that resulted in the formation of planar graphite could have negative consequences for tribological performance. Therefore, this suggest that for lubrication applications, the lower temperature synthesis carbon onions are more resilient to rearrangement under radiation.

2.7   Summary

This research results suggest that the newly identified dislocation-driven mechanisms may play a significant role in graphene layer linking and unlinking rearrangements induced by heavy ion interactions with carbon onions. These changes to carbon onions should, therefore, be anticipated in radiation situations that involve heavy ions, including space and particle accelerator environments. This results indicates the need for pre-investigation of the polygonal character of the onions prior to investigation of their tribological properties. The results further suggests that highly polygonal COs typically considered more perfect, may not be the best starting point for use in space lubrication situations. Planned further experiments will combine mechanical loads with radiation, addition thermal load will also be investigated as well.

	Num	layer	t(nm)	tal	R	max R		avg tal	avg layer	avg t	avg R		t^2(tal^2/R
1700pre1	1	6	0.307	0.74	3.1	3.84		0.7061	6.4	0.3461	2.5024		0.02386596
1700pre1	2	6	0.327	0.207	2.545	2.752	STDEV	0.49093391	1.17378779	0.10390214	0.62146604		
1700pre1	3	6	0.268	1.781	2.532	4.313	STDEOM	0.15524693	0.37118429	0.03285674	0.19652482		
1700pre2	4	8	0.45	1.24	3.01	4.25							
1700pre2	5	4	0.436	0.74	1.991	2.731							
1700pre2	6	7	0.305	0.452	2.437	2.889							
1700pre3	7	6	0.492	0.829	2.266	3.095							
1700pre3	8	7	0.451	0.501	3.591	4.092							
1700pre4	9	8	0.23	0.256	2.161	2.417							
1700pre4	10	6	0.195	0.315	1.391	1.706							
2000pre1	1	7	0.478	1.402	3.212	4.614		0.942	5.7	0.4535	2.9226		0.06244347
2000pre1	2	6	0.625	0.26	3.691	3.951	STDEV	0.39567635	0.9486833	0.08614619	0.5246		
2000pre1	3	7	0.373	1.541	3.737	5.278	STDEOM	0.12512385		0.3	0.02724182	0.16589308	
2000pre2	4	5	0.493	1.056	2.561	3.617							
2000pre2	5	6	0.429	1.107	3.35	4.457							
2000pre3	6	5	0.56	0.449	2.521	2.97							
2000pre3	7	4	0.427	0.729	2.362	3.091							
2000pre3	8	6	0.402	0.871	2.47	3.341							
2000pre3	9	6	0.354	0.875	2.727	3.602							
2000pre3	10	5	0.394	1.13	2.595	3.725							
2300pre1	1	7	0.425	0.988	2.959	3.947		1.4025	6.3	0.4626	3.0928		0.1361022
2300pre1	2	6	0.294	1.029	2.858	3.887	STDEV	0.36777869	0.9486833	0.10492346	0.55695398		
2300pre1	3	5	0.485	1.541	2.905	4.446	STDEOM	0.11630183		0.3	0.03317971	0.17612431	
2300pre1	4	7	0.382	1.701	3.217	4.918							
2300pre2	5	8	0.437	1.226	4.441	5.667							
2300pre2	6	6	0.658	1.2	3.528	4.728							
2300pre2	7	5	0.558	1.237	2.538	3.775							
2300pre2	8	7	0.402	1.178	3.134	4.312							
2300pre1	9	6	0.426	2.064	2.655	4.719							
2300pre1	10	6	0.559	1.861	2.693	4.554							
Ar													
1700-0001	1	6	0.455	1.47	1.824	3.294		1.1558	6.3	0.4331	2.6427		0.09481868
1700-0001	2	7	0.401	0.702	2.946	3.648	STDEV	0.70021422	0.67494856	0.09778826	0.61912789		
1700-0002	3	6	0.545	1.044	2.75	3.794	STDEOM	0.22142718	0.21343747	0.03092336	0.19578543		
1700-0002	4	7	0.509	1.707	3.324	5.031							
1700-0003	5	7	0.515	2.578	3.667	6.245							
1700-0004	6	6	0.553	1.778	2.825	4.603							
1700-0006	7	6	0.414	0.515	2.511	3.026							
1700-0006	8	5	0.338	0.573	1.698	2.271							
1700-0006	9	7	0.283	0.639	2.178	2.817							
1700-0006	10	6	0.318	0.552	2.704	3.256							
Ar													
2000-0001	1	6	0.34	1.421	2.554	3.975		1.5905	7.8	0.3791	3.4322		0.10592594
2000-0001	2	5	0.376	0.86	2.621	3.481	STDEV	0.67784237	3.01109061	0.05604849	1.06060274		
2000-0001	3	6	0.338	1.243	2.985	4.228	STDEOM	0.21435258	0.95219046	0.01772409	0.33539204		
2000-0002	4	7	0.439	1.964	3.242	5.206							
2000-0002	5	5	0.414	0.689	2.618	3.307							
2000-0002	6	7	0.373	1.673	2.529	4.202							
2000-0004	7	11	0.498	1.416	4.56	5.976							
2000-0004	8	13	0.333	3.007	5.364	8.371							
2000-0004	9	6	0.319	2.237	3.061	5.298							
2000-0005	10	12	0.361	1.395	4.788	6.183							
Ar													
2300-0010	1	8	0.335	1.457	4.097	5.554		1.708	7.2	0.3492	3.1408		0.11326192
2300-0011	2	9	0.313	2.4	3.672	6.072	STDEV	0.67727653	1.30384048	0.05318082	0.83281703		
2300-0011	3	6	0.399	1.597	1.899	3.496	STDEOM	0.21417364	0.41231056	0.01681725	0.26335987		
2300-0016	4	7	0.289	2.326	2.965	5.291							
2300-0018	5	6	0.41	0.76	3.071	3.831							
Ca 1700 70MeV													
70_1	1	6	0.391	0.741	2.194	2.935		1.1406	6.7	0.4345	2.787		0.08812707
70_1	2	5	0.413	0.826	1.546	2.372	STDEV	0.46011791	1.7669811	0.07573382	0.95983031		
70_2	3	7	0.432	1.67	3.203	4.873	STDEOM	0.14550206	0.55876849	0.02394914	0.30352499		
70_6	4	9	0.421	1.204	3.07	4.274							
70_6	5	10	0.351	2.032	4.869	6.901							
70_6	6	5	0.574	0.833	1.919	2.752							
70_7	7	5	0.503	0.755	2.162	2.917							
70_7	8	8	0.511	0.782	3.481	4.263							
70_9	9	6	0.424	1.561	3.009	4.57							
70_10	10	6	0.325	1.002	2.417	3.419							
Ca 1700 140MeV													
140_1	1	7	0.476	0.787	2.747	3.534		1.403	7.2	0.441	3.0568		0.12523494
140_2	2	10	0.359	1.84	4.255	6.095	STDEV	0.43659993	1.64316767	0.0866516	0.88877905		
140_10	3	6	0.571	1.452	3.329	4.781	STDEOM	0.13806502	0.51961524	0.02740164	0.28105661		
140_11	4	7	0.429	1.167	3.14	4.307							
140_10	5	6	0.37	1.769	1.813	3.582							

Figure 2.9 Data used to calculate elastic energy within carbon onions.

CHAPTER 3

NANOFETS AS SPACE-BASED ELECTRONICS

3.1   Introduction

Nanocircuits based on semiconductor nanowires, carbon nanotubes, and graphene are all under intense investigation to determine how the superior electronic, thermal and mechanical properties of the component nanomaterials may translate into devices with enhanced capabilities. Research suggests that use of nano-materials within devices may offer inherently better radiation tolerance and thermal performance [68, 85]. Experiments and analyses of radiation and thermal interactions in nanomaterials and corresponding nanocircuits are therefore vital to understand the basis for the promising results, as these would be enabling if they can be reliably exploited.

Amongst radiation situations, those that involve heavy ions are highly destructive for the current state of the art electronics [86] and require the most massive shielding. In the present work, the real-time electronic performances of two gallium nitride (GaN) nanowire-based field effect transistors (nanoFETs) were investigated at 5-minute intervals during 30 minutes of continuous irradiation by xenon-124 relativistic heavy ions. This is the most prolonged real-time nanowire nanoFET investigation under high-energy heavy-ion irradiation to date. The experimental results continued to display serious promise, in that two completely unshielded devices both ran for the full 30 minutes (they were not expected to). New and exciting details about where and how heavy ion radiation couples to nanoFETs were identified for the first time. In this Chapter, the results of the investigations of heavy ion interactions with the Schottky barriers that form between the nanowires and the FET circuit, and that enable device function, are presented. In Chapter 51, results to date of heavy ion interactions with the nanowires themselves, and also the oxide layer, are presented.

The most significant outcome of the investigations in this area are the threshold voltages

shifts as a function of time that were observed and reported by this thesis work[87]. The shifts observed immediately upon beam exposure and within the first 5-minute interval indicated a current surge, i.e., device improvement. The immediate and improved nature of the response suggests Schottky barrier manipulation, as radiation damage to the nanowires and/or the oxides would be expected to be cumulative and consistently negative. The subsequent electronic behavior from 5-30 minutes indicated the action of one or more competing mechanisms.

Three models were investigated as part of this thesis to explain the initial current surge and subsequent electronic behavior. It was shown that the experimental behavior can be successfully modeled using the combined thermionic emission-tunneling approach, leading to new and quantitative information about barrier height, carrier concentrations, expected temperature behavior, and tunneling.

3.2 Material and Methods

3.2.1 NanoFET Fabrication

Two previous students (BW.Jacobs and K.McElroy) prepared more than 75 back-gated GaN nanoFET devices using the method described here. A highly doped p-type silicon wafer ($\sim 5\text{M}\Omega$-cm) was used as the nanoFET substrate with a 100 nm layer of thermally grown silicon dioxide as the gate dielectric. The backside of the wafer was stripped of silicon dioxide (SiO2) using hydrofluoric acid, and Ti/Au (10/70 nm) was thermally evaporated (Edward Auto306) to form the global back gate. GaN nanowires synthesized by a catalyst-free [41] direct reaction of gallium vapor and ammonia at 850 °C were dispersed from an ethanol solution onto the substrate. Extensive HRTEM studies [86] showed that nanowires are grown at 850 °C had a triangular profile with base widths 60-120 nm [44] Source and drain contacts to photo-lithographically (PL) pre-fabricated contact pads were patterned using electron beam lithography (EBL, JEOL 840A SEM). After exposure to a 100W oxygen

plasma (March Instruments PX-250) for 30 sec to remove any electron beam resist residue, Ti/Au (10/30 nm) was thermally evaporated for the conducting source and drain contacts. Subsequent metal lift-off was performed in acetone. The nanoFET architecture and a top-view SEM image of the nanocircuit are shown in Figure 3.1 (a-b).
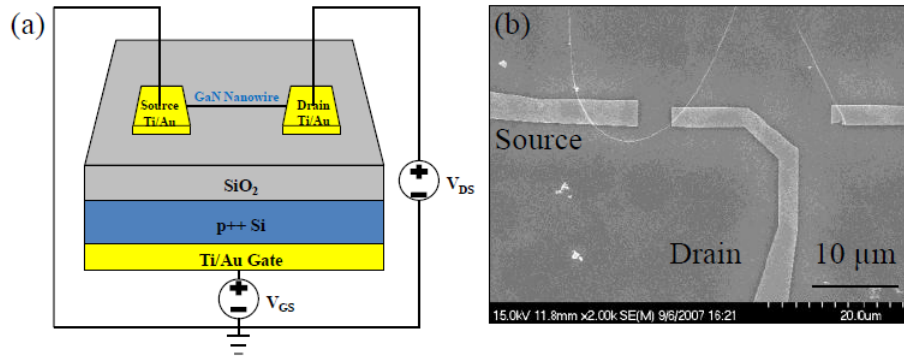
Figure 3.1 (a) NanoFET architecture and (b) top view SEM of EBL contacts and Nanowire taken by BW. Jacobs.

Two nanoFETs were positioned vertically in the direct beam path by installing a custom-built non-charging mounting plate with rear openings for electrical connections to the grounded dual in-line package on a robotic arm. A robotic arm, with computer-driven control and laser alignment, was used to center the nanocircuit within the beam path. The source and drain PL contact pads were connected by ultrasonic wedge wire bonding (West Bond 7400B) to the individual pins of a dual in-line package. Remote connections between the NSCL Single Electron Event Test Facility (SEETF) vault and a control room enabled real-time electronic control, data recording, and video viewing.

3.2.2 Beam Parameters

The experiments were performed at the NSCL at Michigan State University using a well calibrated xenon-124 primary beam. A xenon-124 53+ beam with an energy of 140 MeV/nucleon was focused to uniformly irradiate a ~10 mm x 10 mm area and measured from known dimensional markings on a beam-viewing scintillator plate before the experiments. After

passing through a 0.075 mm zirconium (Zr) foil exit window and a 485 mm air gap, the beam-on-target energy was 127.33 MeV/u for both nanoFET. The beam-on-target charge state was determined to be 75% 54+ (fully stripped), 23% 53+, and 2% 50-52+, calculated by GLOBAL [88]. The beam was blocked at 31:10 min: sec for nanoFET1 and 31:08 min: sec for nanoFET2.

3.3   Real-Time I-V Characteristics during Continuous Irradiation

The prior(pre), and real-time I-V performances of two individual nanoFETs were recorded.

3.3.1   Pre-Radiation Performance

Before radiation, the two nanoFETs were individually tested for I-V performance using a Keithley 4200 Semiconductor Parameter Analyzer System. Both nanoFETs showed diode-like behavior. NanoFET1 showed an efficient turn-on voltage of around 5 volts for current output in the micro-amp range. However, nanoFET2 has suffered from considerable turn on voltage around 20 volts for $\sim$100s of nano-amp current output. These experiments were repeated daily in the week preceding the NSCL experiments, and consistent results were obtained. VGS curve families for -1.0, 0, +1.0 V bias voltages were collected and confirmed for n-type transport behavior.

Due to the pre-radiation behavior, one would expect the good performance of nanoFET1 and poor performance nanoFET2 would carry over into the radiation tests. The real-time experiment was initially designed to observe the radiation resilience of the two pre-analyzed good versus bad devices with an expectation of bad device failure.

Compliances for the real-time experiments were set to low values to minimize electrical stress during the full 30-min experiment duration. (1.0 uAmp for nanoFET1 and 100nAmp for nanoFET2). V_{GS} curves -1.0, 0.0, +1.0 V were collected during the real-time measurements with a collection time of about 30 sec per family. V_{GS} bias voltage values were also

kept low to minimize electrical stress. Only minor variations in the I-V curves were observed as a function of gate voltage, therefore only the VGS = -1.0 V results are reported here as the first curve in each family, eliminating possible recording hysteresis effects that can occur when collecting curve family.

3.3.2 Real-Time Performance under Radiation

Upon radiation, both of the nanowires showed current surge behavior immediately upon beam interaction (0 sec). Surprisingly nanoFET2 demonstrated substantial improvement over its PR performance. This improvement necessitated compliance change first to 500nA at 5 min then to 1uA for the remaining time in the beam. The improvement in I-V characteristic held throughout the radiation duration with small variations as discussed below, which indicates that the beneficial radiation effect on nanoFET2 was permanent than temporary.

For both nanoFETs, the I-V characteristic shifted to the left (lower turn-on threshold) immediately upon exposure (0 sec) to the heavy ion beam, as shown in Figure 3.2 (a). For nanoFET1, the leftward shift continued, with the lowest turn-on threshold observed for the 5 min measurement. After that, the I-V characteristic shifted to the right in small increments for the 10 to 25 min measurements, with a more significant increase between the 25 and 30 min measurements, as shown in Figure 3.2 (b). The immediate post-irradiation characteristic showed no apparent changes. Figure 3.2 (c) shows the reverse bias measurement for nanoFET1.

In the case of nanoFET2, shown in Figure 3.3, the turn-on threshold voltage reduces by substantial amount under the beam from the immediate radiation. From $V_{DS} \sim 20V$ to $V_{DS} \sim 1V$, this improvement stabilizes itself similar to nanoFET1 with the lowest turn-on voltage also 5 min measurement. It is worth pointing out that even at ~ 30 mins region, nanoFET2 maintained low threshold with $V_{DS} \sim 3V$ for micro-Amps of current. Figure 3.3 (c) shows the reverse bias measurement for nanoFET2.
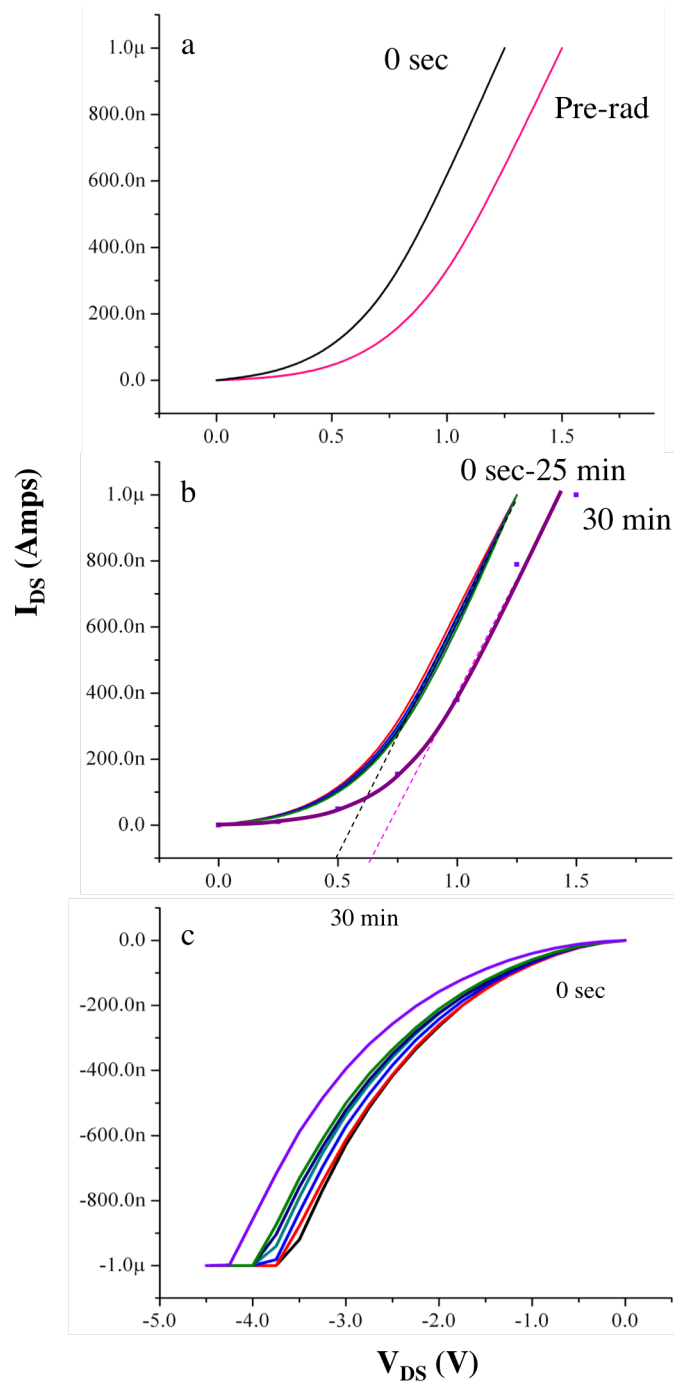
Figure 3.2 Characteristic shifts as a function of time for nanoFET1 under heavy ion radiation (a) Pre-rad to 0 second (b) forward bias and (c) reverse bias.
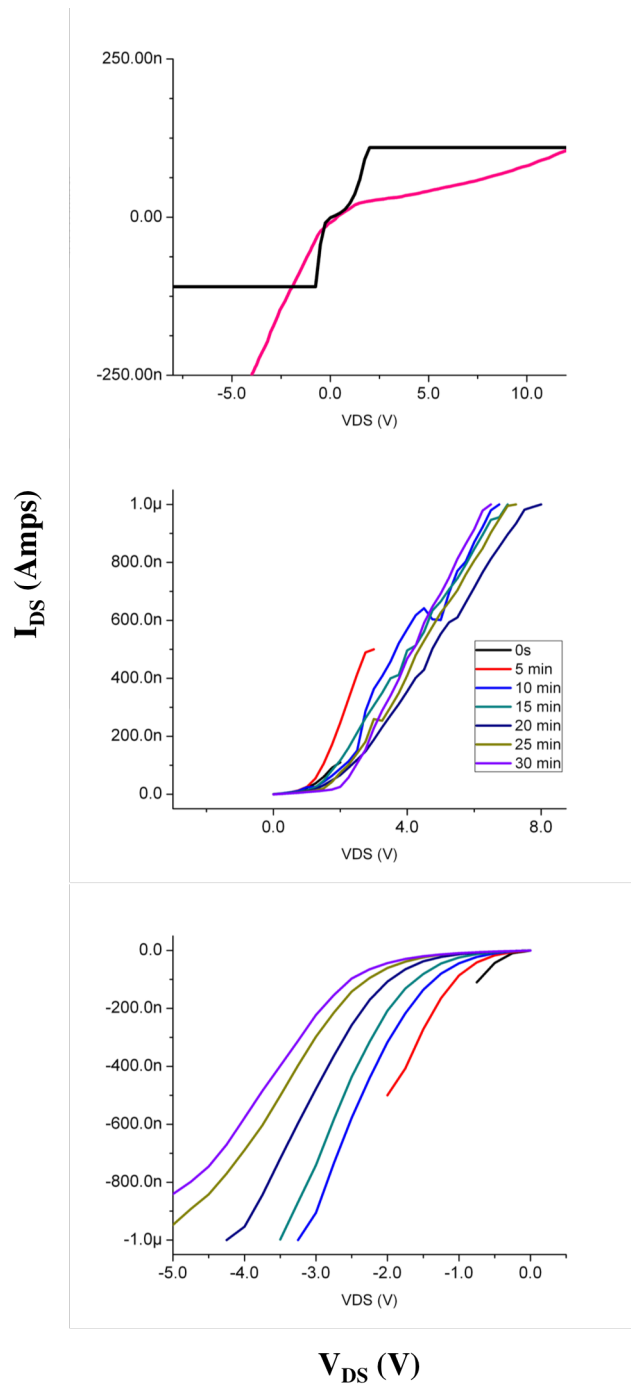
Figure 3.3 Characteristic shifts as a function of time for nanoFET2 under heavy ion radiation (a) Pre-rad to 0 second (b) forward bias and (c) reverse bias.

3.4 Investigation of Theoretical Interpretations for Experimental Data

To start with, the immediate of the response between at 0 min continuing through 5 min strongly indicated that contacts as the most likely source of the observed alterations. Changes to the nanowire and/or the oxide layer would be expected to be cumulative over the full ~30 mins time periods.

Following the idea of contact modulation. I investigated three models to interpret the experimental results: the space charge limited model, the thermionic emission model, and the thermionic field-emission model. Field emission (ohmic contact) was ruled out by the nonlinear shapers of the I-V characteristics.

3.4.1 Interpretation by Space Charge Limited Model

Space charge limited (SCL) transport has been previously reported for GaN nano-rod two-point measurement [32, 89].SCL current transport in the mobility regime has a power-law dependence, L is the thickness of the pure region.

$$J = \frac{9\varepsilon_s \mu V^2}{8L^3} \tag{3.1}$$

Therefore, a linear result is expected when I_{DS}/V_{DS} is plotted versus V_{DS}. However, all I_{DS}/V_{DS} versus V_{DS} plots were also nonlinear as shown in Figure 3.4. This suggests that the observed nonlinear IV characteristic results from a Schottky barrier rather than SCL transport.

3.4.2 Interpretation by Thermionic Emission Model

The current data was then fit exponentially using $A\exp(BV_{DS})$ and interpreted using a thermionic emission model [32]

$$J = \frac{1}{\text{Area}} = J_{TE}(e^{\frac{qV_D S}{nkT}} - 1) \tag{3.2}$$
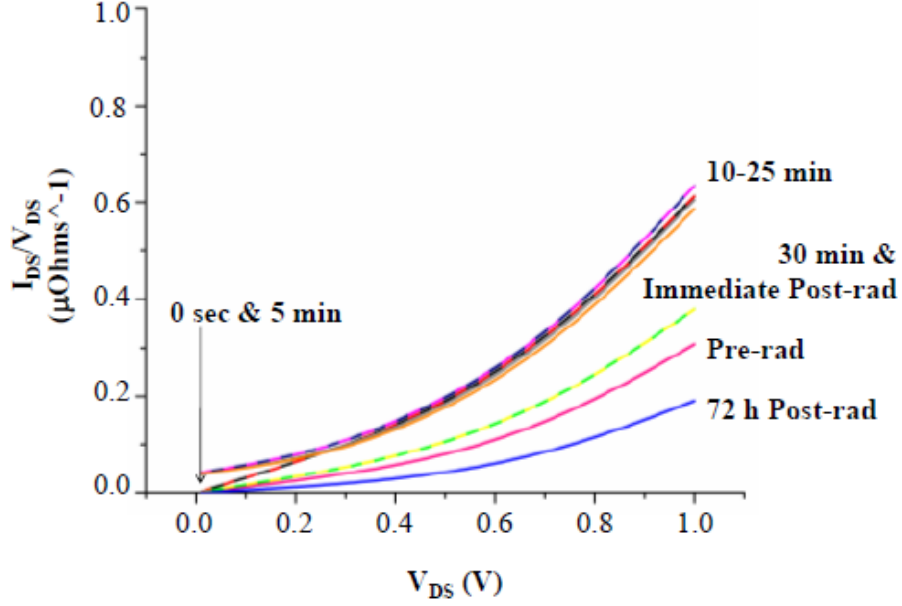
Figure 3.4 Nonlinear relationships between I_{DS}/V_{DS} versus V_{DS} observed for all data sets eliminated space charge limited model.

$$J_{TE} = A^* T^2 e^{\frac{-q\varphi B_n}{KT}} \qquad (3.3)$$

A^* is the effective Richardson constant $= 120 \text{ A/cm}^2\text{-K}^2$, $T = 300$ K was assumed. A diode ideality factor n was extracted from fitting parameter B and a scaled barrier height $q\varphi_{Bn}$ was extracted from fitting parameter A. These are shown plotted together as a function of irradiation time in Figure 3.5 for the forward current data. Ideality factor values ranged from about 13 to 18 with corresponding increases/decreases in effective barrier height. While these results are consistent with values reported for GaN nanowire devices [90], typically interpreted as indicative of tunneling, the thermionic emission model does not accommodate tunneling. When tunneling is a significant contribution, it is correct to use the thermionic field emission model for transport through a Schottky barrier.

3.4.3   Interpretation by Thermionic Field Emission Model

Thermionic field emission current includes tunneling of thermally excited carriers that see a thinner barrier. A criterion for thermionic emission versus thermionic field emission versus
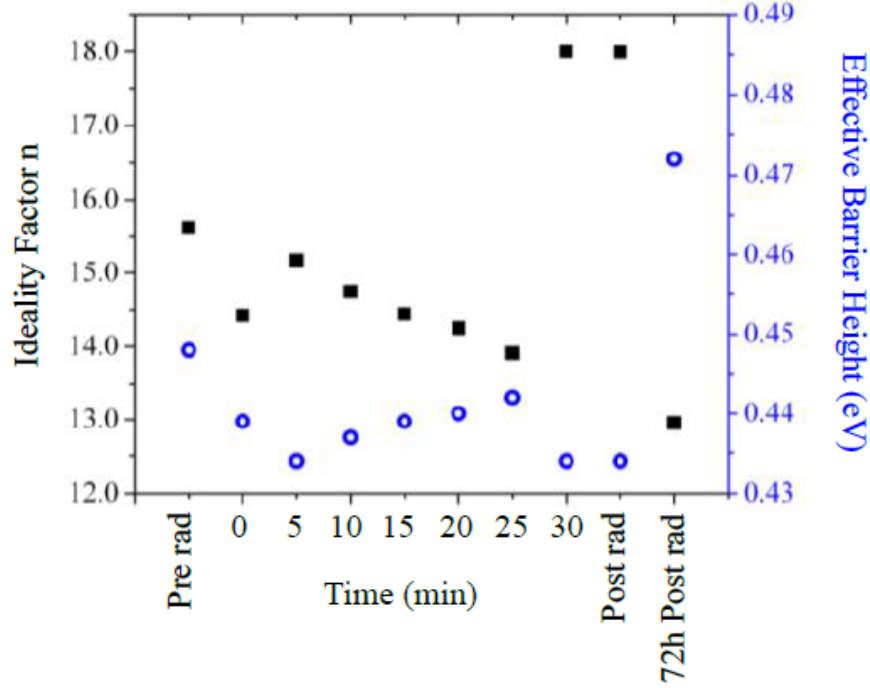
Figure 3.5 Ideality factors and scaled barrier heights from thermionic emission model.

field emission is found by comparing the thermal energy kT to E_{00} defined as

$$E_{00} = \frac{q\hbar}{2}\sqrt{\frac{n}{m^*\varepsilon_s}}$$ (3.4)

E_{00} is a reference energy that emerges naturally in a Wentzel-Kramers-Brillouin (WKB) treatment of transport through an arbitrarily-shaped Schottky barrier, described in section 3.5 below. The ratio of kT to E_{00} is related to the amount of tunneling across the Schottky barrier. For thermionic emission (TE: no tunneling), kT $\gg E_{00}$. For thermionic field emission (TFE: significant but not dominant tunneling), kT$\sim E_{00}$. For field emission (FE: dominant tunneling), kT $\ll E_{00}$. GaN nanowires are intrinsically n-type with a reported n range [8] of $10^{18\text{-}19}$ cm^{-3} or greater. It is simple to calculate that for n = $10^{18\text{-}19}$ cm^{-3}, E_{00}-wurtzite-GaN = 0.0138-0.0438 eV and E_{00}-zinc-blende-GaN = 0.0165-0.052 eV. These values are all $\sim$ kT = 0.0259 eV, which indicates that use of the TFE model is correct for GaN nanoFET devices. As high current densities are typically observed for most semiconductor nanowire

56

based devices, use of the TFE model is generally indicated.

Following these indications that TFE was the correct model. Initial investigation of its parameter dependences to determine if this model could accommodate the experimentally observed shifts is performed, For Thermionic Field Emission, the forward current density is defined as

$$J_{TFE} = \frac{A^{**}T\sqrt{\pi E_{00}q(\varphi_{Bn} - \varphi_n - V_F)}}{k\cosh(\frac{E_{00}}{KT})}\exp[\frac{-q\varphi_n}{kT} - \frac{q\varphi_{Bn}}{kT} - \frac{q(\varphi_{Bn} - \varphi_n)}{E_0}]\exp[\frac{qV_F}{E_0}] \quad (3.5)$$

$$\varepsilon_0 = \frac{E_{00}}{\frac{E_{00}}{kT} - \tanh\frac{E_{00}}{kT}} \quad (3.6)$$

Where A^{**} is now the reduced effective Richardson constant that includes tunneling and also reflections at the barrier [32]. The square root factor relates the barrier height with image charge reduction to experimentally observed device operation thresholds. The following factors: N, T, A^{**} and electron energy $q\varphi_{Bn}$ are all potentially significant. In this work, each of these elements was varied over an experimentally-identified range, and the effect of shifting J_{TFE} to the left or the right was investigated.

Concentration N was varied from $10^{19\text{-}20}$ cm^{-3} in $10^{19+n*0.25}$ cm^{-3} increments. The remaining parameters were set as follows: $q\varphi_{Bn}$ = 2.0 eV and $q\varphi_{Bn}$ = 0.2 eV, consistent with experimental operation; T = 300 K; and A^{**}= 14.7 A cm^{-2}K^{-1}, experimentally determined for Au on GaN [9]. The result shown black to red in Figure 3.6 (a) indicates that increasing n shifts the characteristic to the left.

Temperature T was varied from 250-450 K in 50 K increments. The result showed black to red in Figure 3.6 (b) indicates that increasing T would continue to shift the characteristic to the left.

Reduced effective Richardson Constant A^{**} was varied from 15.0 down to 3.0 cm^{-2}K^{-1} in increments of 3.0 A cm^{-2}K^{-1}, shown black to red in Figure 3.6 (c). Other parameters were set as before with the addition of T = 300 K. Decreasing A^{**} shifted the characteristic to the right.
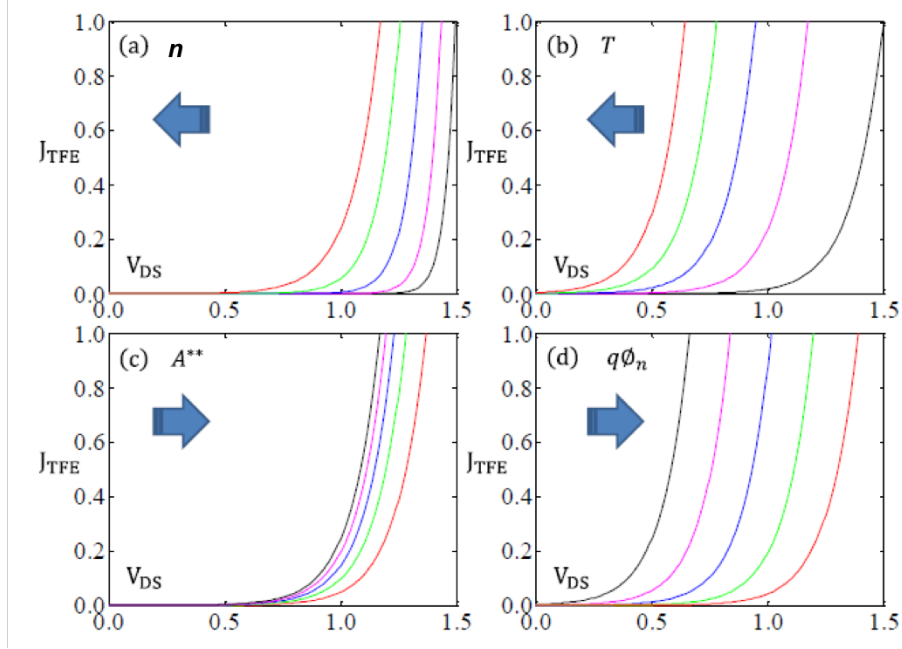
Figure 3.6 J_{TFE} Forward shifts for (a) Concentration N (b) Temperature T (c) Reduced Effective Rchiardson Constant A^{**} and (d) Electron energy $q\varphi_{Bn}$.

Increasing the electron energy would enable electrons to perceive a thinner Schottky barrier and would also facilitate tunneling. Electron energy $q\varphi_{Bn}$ was varied from 0.05 to 0.25 eV in 0.05 eV increments. Other parameters were set as before with the addition of $A^{**} = 12.0^{-2}K^{-1}$. Increasing $q\varphi_{Bn}$ also shifted the characteristic to the right, as shown in Figure 3.6 (d).

Therefore, use of the TFE model was indicated as correct, based on high correct densities and its ability to provide interpretation of the experimentally observed shifts. The full analysis requires to incorporate forward and reverse TFE Schottky barrier transport models within a Metal-Semiconductor-Metal structure of the device.

3.5   Modeling for TFE Transmission through Schottky Barrier

Nanowire, nanotube and graphene nanocircuits operate as Schottky barrier devices, in which functional capability is achieved through barrier manipulation [91, 92, 93]. The general

theory for Schottky barriers based on a WKB description of transport through an arbitrarily shaped Schottky barrier was developed by Sze [94], Stratton [59] and Crowell [95] among others. The transmission coefficient T(E) for tunneling through a finite potential barrier of width W and constant barrier height is well-known [96]. The equivalent transmission coefficient for tunneling through a finite potential barrier with a slowing varying barrier height such as a Schottky barrier can be found using the WKB approximation [96] to be the following, which shows the dependence of tunneling on effective mass m*.

$$T(E) = \exp^{-2\int_0^W k_x dx} \tag{3.7}$$

$$\hbar k_x = \sqrt{2m^*(E_{\varphi x} - E)} \tag{3.8}$$

The barrier height $E_{\varphi(x)}$ and the free carrier energy E can be conveniently normalized to the thermal energy kT:

$$h = \frac{E}{kT} \tag{3.9}$$

$$\zeta = \frac{E_{\varphi(x)}}{kT} = \frac{q}{kT}\varphi(x) = \beta\varphi(x) \tag{3.10}$$

leaving

$$k_x = \frac{1}{\hbar}\sqrt{2m^*kT(\zeta - h)} \tag{3.11}$$

which introduces a dependence on temperature T. Following the approach of Zhang et al. [97], the free carrier charge density is related to the barrier potential using the Poisson equation:

$$\frac{d\varepsilon(x)}{dx} = -\frac{d^2}{dx^2}\varphi(x) = \frac{\rho}{\varepsilon_r\varepsilon_0} \tag{3.12}$$

$$\rho = qn(1 - \exp^{\frac{q\varphi(x)}{kT}}) = qn(1 - \exp^{\beta\varphi(x)}) = qn(1 - \exp^{-\zeta}) \tag{3.13}$$

which shows the dependence on free carrier concentration n and relative dielectric constant ε_r. Integration once by parts shows that the variation of normalized barrier height with distance is given by

$$\frac{d\zeta}{dx} = \pm\sqrt{2\alpha\beta(\exp^{-\zeta} + \zeta)} \tag{3.14}$$

59

$$\alpha = \frac{nq}{\varepsilon_r \varepsilon_0} \tag{3.15}$$

and therefore

$$dx = \pm \frac{d\zeta}{\sqrt{2\alpha\beta(\exp^{-\zeta} + \zeta)}} \tag{3.16}$$

The final result for the transmission coefficient for tunneling through a slowly varying Schottky barrier is therefore

$$T(h) = \exp^{-\frac{kT}{E_{00}} \int_h^{\zeta E_b} \frac{\sqrt{\zeta - h}}{\sqrt{\exp^{-\zeta} + \zeta}}} \tag{3.17}$$

$$E_{00} = \frac{q\hbar}{2} \sqrt{\frac{n}{\varepsilon_r \varepsilon_0 m^*}} \tag{3.18}$$

The ratio kT/E_{00}, therefore, sets the scale for the amount of tunneling. When kT/E_{00} is large, the tunneling coefficient is small, and the TE description is accurate. As kT/E_{00} decreases, the tunneling coefficient increases. Ratio values of $kT/E_{00} \sim 10$, 1 and 0.1 are typically used to indicate the regimes in which TE, TFE and FE transport is dominant, respectively [97, 98]. **Therefore, high free carrier concentrations n typically reported for nanowire nanoFETs [99] will typically drive Schottky barrier transport into the TFE regime.** Figure 3.7 shows the the transport regime using an energy band diagram.

Figure 3.7 Energy-Band Diagram showing transport regimes through the reverse biased Schottky barrier.

However, TFE regime analysis is difficult due to its multivariate nature. This is why Schottky barrier-based nanoFET devices have been analyzed using the mathematically tractable TE model even when a too-high ideality factor indicates that tunneling is present [90]. This thesis work is deeply involved in the development of a novel self-consistent mathematical stability approach that enables determination of the vital TFE fitting parameters by first identifying stable ranges for those parameters (Along with Professional Assistant Steve A Hartz). This study also provides a new fundamental picture of how the fitting parameters approach the TFE regime limits. The new stability approach was developed for and first demonstrated in the analysis of the barrier heights, tunneling probabilities and potential drops on this unique dataset: changes in the Schottky barriers of gallium nitride (GaN) nano-field effect transistors (nanoFETs) in a long-duration heavy ion radiation extreme environment. This investigation is yielding fundamental insights into nanocircuit behavior in this extreme environment that would be challenging to predict a priori.

3.6 Thermionic Field Emission through GaN NanoFET Schottky Barrier

The nanoFET circuit is described below using a full metal – semiconductor – metal(MSM) circuit formulation with reverse TFE and forward TE Schottky barriers at the entry and exit contacts. As will be shown, device performance is primarily controlled by the entry contact for the voltage ranges in these experiments.

3.6.1 Ideal model for TFE I-V Characteristics

The equation for reverse TFE [100] is

$$J = [\frac{A^{**}T}{k}\sqrt{\pi E_{00}q(V + \frac{\varphi}{\cosh^2\frac{E_{00}}{kT}}}\exp(\frac{-q\varphi_{Bn}}{E_0})]\exp(\frac{qV}{\varepsilon'}) \tag{3.19}$$

$$E_{00} = \frac{q\hbar}{2}\sqrt{\frac{n}{m^*\varepsilon_s}} \tag{3.20}$$

$$E_0 = E_{00}\coth(\frac{E_{00}}{kT}) \tag{3.21}$$

$$E' = \frac{E_{00}}{(\frac{E_{00}}{kT} - \tanh(\frac{E_{00}}{kT}))} \tag{3.22}$$

with reduced effective Richardson constant A^{**}, temperature T, effective barrier height $q\varphi_{Bn}$ and carrier concentration n [100].

3.6.2 Overview of Approach to Successfully use the Thermionic Field Emission Model

Any attempt to use equation 3.19 to fit experimental data thus directly requires that four variables be known or well-guessed. Lousy trial guesses can lead to unstable fittings that do not represent experimental results. Furthermore, using experimentally determined values for guidance can also lead to problematic fits, if those values were acquired under non-nanoscale experimental conditions, as discussed below.

Stable ranges for each TFE parameter needs to be identified, and only then perform fits to experimental data within those ranges. The steps are as follows. A reverse TFE I-V curve is generated using known (generation) values for temperature T, carrier concentration n, and effective barrier height $q\varphi_{Bn}$. Fits performed on the generated curve using the Levenberg-Marquardt Algorithm [101, 102] are used to identify stable parameter ranges for these parameters. The reduced effective Richardson constant A^{**} can be treated separately, as discussed below.

When the TFE model was used to fit experimental data within the identified parameter ranges, a stable solution resulted that was optimized using a least squares fit. The asymmetric Schottky barriers at both contacts and carrier concentration n were then determined, and a temperature dependence investigation was performed. The transmission probabilities at each Schottky barrier as a function of time in the beam, and the potential drops across the Schottky barriers and also across the nanowire as a function of time in beam and V_{ext}, were also determined, following the recent approaches of Zhang [100] and Peng [97].

3.6.3   Determination of the TFE Parameter Ranges

In what follows, the effective mass m* was equal to 0.27 m_0 and the relative dielectric constant ε_S was equal to $10.4\varepsilon_0$ (wurtzite GaN). The reduced effective Richardson constant is a multiplicative factor in Equation 3.19 that shifts the J-V characteristic and was therefore assigned a previously determined experimental value [103] of 14.7 A/K cm^2.

Fits were first performed on a generated reverse TFE J-V curve using the Levenberg-Marquardt Algorithm [104], which performs a least-squares fitting for a model equation to a dataset. The goal was to identify the range of guess values for which the fit values matched the hidden generation values as a key first step towards finding parameter ranges for stable solutions. After each successful fit of the data, the initial generation-value guesses were set farther from the correct values. Values both well above and well below the generation values were tested. When the algorithm failed to fit the data, the guess parameters were brought in closer to the generation values until the algorithm converged onto the correct parameter values once more. In this manner, a range of parameter values was found in which the fit self-consistently identified the generation parameters. Furthermore, information about how the fit failed, whether gradually, abruptly or through location of local minimum, was obtained. This is a general method that requires only effective mass and dielectric constant for a given semiconductor.

For temperature T, generation values of 250-350 K were precisely reproduced by a broad range of guess values from 200 K through 2800 K, the melting point of GaN. Fits to the TFE equation below 200 K abruptly became unstable over a narrow range of values 199.5 K through 199.0 K, shown in Figure 3.8. As active cooling was not employed in the beam experiments, the volatile region was never reached. A temperature parameter range of 300-350 K was used to fit the experimental data using the TFE model, allowing room temperature and possibly higher behavior.

Fits to the TFE model were more restrictive for carrier concentration n. Catastrophic
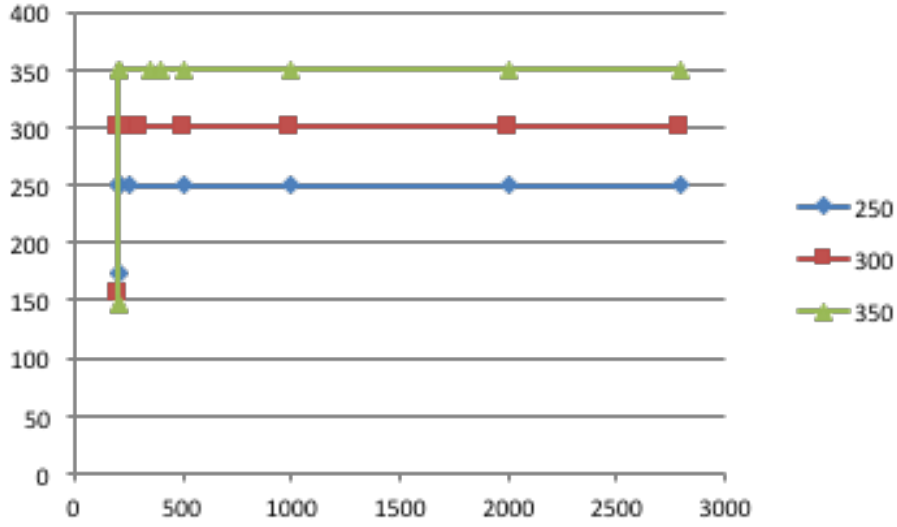
Figure 3.8 Ranges for which fitted results match generation value for temperature T.

fit-failure observed at low guess-concentrations, and gradual divergence was observed at high guess-concentrations, as shown in Figure 3.9 (a). Since the precise edge of the continuous divergence region will not be known for experimental data, guess-concentrations near this region should especially be avoided.
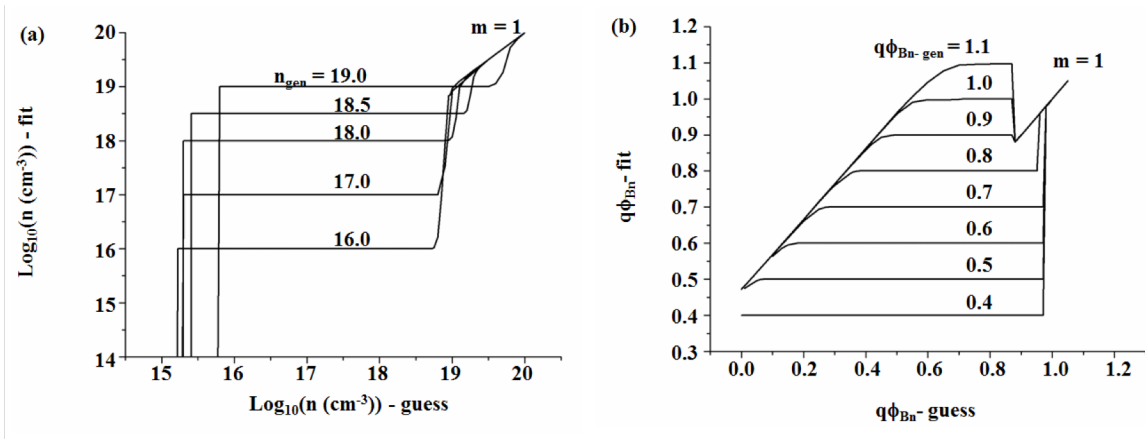
Figure 3.9 Ranges for which fitted results match generation value for (a) carrier concentration and (b) effective barrier height.

At sufficiently high guess-concentrations, the algorithm failed to fit the curve and simply returned the initial guess as the fit value, shown in Figure 3.9 (a) as the linear region with slope m=1. Fits to the TFE equation also abruptly became unstable over a narrow range of

64

values for each generation concentration at guess-concentrations below 10^{16}cm^{-3}, consistent with the TFE condition kT/E$_{00}$ $\sim$ 1 [98, 100]for GaN. Generation values of $10^{19.5}$ cm^{-3} and above produced spurious local minima at low guess-concentrations (not shown) that established n $\sim$ 10^{19}cm^{-3}as the upper limit. The constraints and limits therefore identified 10^{16}-$10^{18.5}$ cm^{-3} as the stable parameter range for TFE model fits in GaN.

Results for effective barrier height qφ_{Bn} are shown in Figure 3.9 (b). The range of guess values for which the fit reproduced the generation values was broad for low barrier heights but became increasingly restrictive as barrier height increased. The fit value diverged from the generation value without immediately evident catastrophic fit-failure at low guess-barrier heights and abruptly became unstable at high guess-barrier heights, ultimately jumping to the m = 1 line. The parameter range that would safely fit all effective barrier heights for a TFE mechanism was therefore restricted to 0.7-0.8 eV.

3.6.4 Fitting to Experimental Date Set to Actual Parameters

The TFE model was then used to fit the experimental data shown in Figure 3.2 and Figure 3.3 and optimized using a least squares fit within the parameter ranges identified above.

The values for effective barrier heights qφ_{Bn1} and qφ_{Bn2} and carrier densities n were then obtained by least squares fits of the reverse TFE model to the exponential regions of the I-V curves at low bias. The exponential and linear regions were identified for each I-V curve and individually fit, following the approach of Peng et al. [97].

The experimental contact areas required to convert J-V to I-V were estimated using scanning electron microscope images. The EBL-fabricated contact areas had similar values, and the smaller values were used in the present study, pending further investigation of the actual sub-surface contact environment. The contact areas were 7.5 x 105 nm^2 for nanoFET1 and 5.2 x 105 nm^2 for nanoFET2. The values for nanowires resistances R were obtained by least squares fit of an ohmic model to the linear regions of the I-V curves at high bias. The

average values were: 0.7 MΩ for nanoFET1 and 5MΩ for nanoFET2, consistent with the pre-radiation (PR) device performances.

When the metal electrodes are referred to as contacts 1 and 2 [94, 97], a positive bias on the contact 2 metal electrode corresponds to forward bias of the nanocircuit. In this study, contact 1 was the reverse-biased Schottky barrier, modeled by reverse TFE, and contact 2 was the forward biased Schottky barrier modeled by forward TE as demonstrated with Figure 3.10. When a negative bias was applied to contact 2 during the voltage sweep, the nanocircuit was in reverse bias, and contact 2 was the reverse-biased Schottky barrier, modeled by reverse TFE, while contact 1 was the forward biased Schottky barrier modeled by forward TE. Fitting the forward and reverse bias I-V curves, therefore, enabled extraction of both $q\varphi_{Bn1}$ from the Schottky barrier at contact 1 and $q\varphi_{Bn2}$ from the Schottky barrier at contact 2.
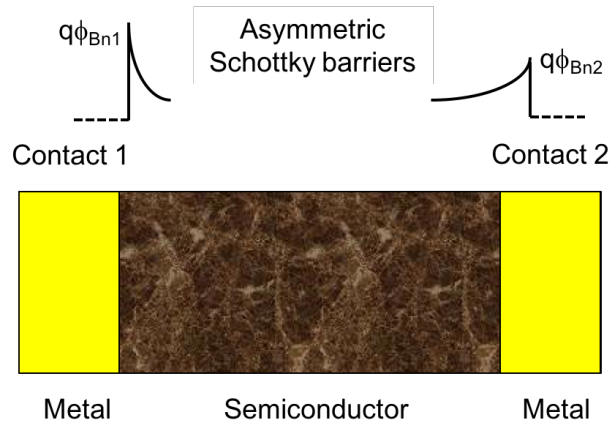
Figure 3.10 Metal-Semiconductor-Metal Structure with Asymmetric Schottky Barriers.

The experiments were carried out at room temperature. Investigation of the TFE equation for its stable parameter range showed that the J-V curve shifted to the left as a function of increasing temperature. As this did not match the experimental results for the 5-30 min time periods, and as no other indications of substantially increased temperature were present, T = 300 K was assumed.

Effective barrier heights $q\varphi_{Bn1}$ and $q\varphi_{Bn2}$ and the carrier densities n were evaluated

Table 3.1 Effective Barrier Heights and Carriers Concentrations for Time in Beam

NanoFET1	$q\varphi_{Bn1}$(eV)	$q\varphi_{Bn2}$(eV)	Log(n) forward	Log(n) reverse	n_{ave}	kT/E_{00}(Avg)
Pre-rad	0.482	0.482	18.33	17.77	1.12E+18	2.22
0 min	0.437	0.437	18.23	18.00	1.29E+18	2.06
5 min	0.434	0.434	18.26	18.00	1.35E+18	2.02
10 min	0.434	0.434	18.26	18.00	1.29E+18	2.02
15 min	0.433	0.433	18.27	17.99	1.34E+18	2.03
20 min	0.440	0.440	18.28	18.01	1.39E+18	1.99
25 min	0.444	0.444	18.28	18.01	1.40E+18	1.98
30 min	0.494	0.494	18.35	17.96	1.44E+18	1.96
NanoFET2	$q\varphi_{Bn1}$(eV)	$q\varphi_{Bn2}$(eV)	Log(n) forward	Log(n) reverse	n_{ave}	kT/E_{00}(Avg)
Pre-rad	0.420	0.466	16.87	17.73	0.18E+18	5.53
0 min	0.458	N/A	17.92	N/A	0.82E+18	2.59
5 min	0.449	0.471	17.80	18.13	0.93E+18	2.43
10 min	0.451	0.487	17.79	18.11	0.88E+18	2.50
15 min	0.453	0.508	17.76	18.13	0.88E+18	2.50
20 min	0.448	0.521	17.69	18.12	0.88E+18	2.62
25 min	0.451	0.511	17.69	18.04	0.73E+18	2.75
30 min	0.449	0.516	17.63	18.05	0.69E+18	2.82

from reverse TFE model fits as given in Table 3.1. Both nanoFETs exhibited asymmetric ($q\varphi_{Bn1} \neq q\varphi_{Bn2}$) effective barrier heights with values $\sim 0.4 to 0.5 eV$. The TFE analysis, therefore, suggested that the effective barriers may be lower than previously reported values based on TE analysis of GaN nanowires [18, 22, 23]. The carrier densities n were $\sim 10^{18}$ cm^{-3}, consistent with previously reported experimental results for GaN nanowires [99]. The differences between the carrier density values obtained in forward and reverse bias may be due to the lack of precise information about the actual contact areas. In subsequent calculations, the arithmetic mean $n_{ave} = (n_{for} + n_{rev})/2$ was used for n as a function of time in beam.

3.6.5 Transmission Probability

Evaluation of effective barrier heights $q\varphi_{Bn1}$ and $q\varphi_{Bn2}$ and the carrier densities n further enabled determination of the transmission probabilities at each Schottky barrier as a function of time in the beam. The transmission probability T_f appropriate [100] for the TFE mechanism is given by

$$T_f \approx \exp[-\frac{kT}{E_{00}}y_1(\zeta_b, h)] \tag{3.23}$$

$$y_1(\zeta_b, h) = \sqrt{\zeta_b(\zeta_b - h)} - h \ln\left(\frac{\sqrt{\zeta_b} + \sqrt{\zeta_b - h}}{h}\right) \tag{3.24}$$

$$\zeta_b = \frac{E_b}{kT} = \frac{q\varphi_{Bn}}{kT}, h = \frac{E}{kT} \tag{3.25}$$

ζ_b and h are the normalized barrier height and carrier energy $E < E_b$, respectively. The expression for carrier concentration as an equivalent energy E_{00} [32, 100] is given in equation 3.21.

The transmission probabilities are shown in Figure 3.11. For the nanoFET1, the contact 1 Schottky barrier initially showed increased tunneling at lower energies, starting from the PR to 0 min transition and continuing until 15 min, as shown in Figure 3.11 (a). The probabilities is then increased over the 15-30 min period. This differed from the energy required for tunneling at the contact 2 Schottky barrier, which grew steadily (Figure 3.11 (b))

For nanoFET2, the contact 1 and 2 Schottky barriers both showed a new crossover effect during the PR to 0 min transition that resulted in ~20-50% transmission probabilities at lower energies. This was consistent with the unexpected improvement that required the compliance increase during the experiments. The 5 min result is shown in Figure 3.11 (d) as the unexpected improvement resulted in a collection of too few data points for reliable analysis.

3.6.6 Electron Transmission Mechanism Modeling by Metal-Semiconductor-Metal Approach

The Sze-Peng [97] formulation was used to determine the potential drops V_1 and V_3 across the Schottky barriers and V_2 across the nanowire as a function of Vext and time in beam. The voltage $V_{ext} = V_{DS}$ across the entire MSM structure is the sum

$$V_1 + V_2 + V_3 = V_{ext} \tag{3.26}$$

$$I_1 = I_2 = I_3 = J_1 Area_1 = J_2 Area_2 = J_3 Area_3 \tag{3.27}$$
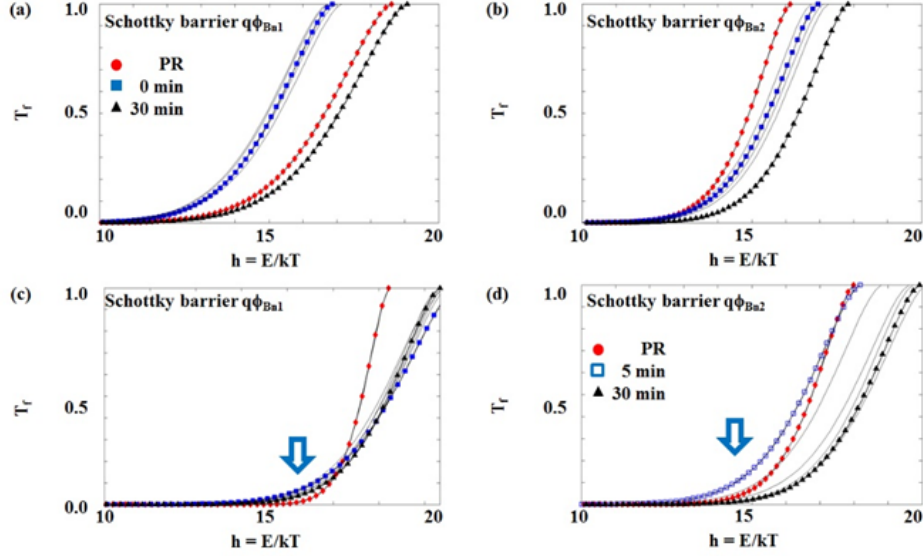
Figure 3.11 NanoFET1 transmission probabilities for (a) $q\varphi_{Bn1}$ and (b) $q\varphi_{Bn2}$. NanoFET2 transmission probabilities for (c) $q\varphi_{Bn1}$ and (d) $q\varphi_{Bn2}$.

Transport across the reverse Schottky barrier was modeled using reverse TFE as shown in equations 3.19-3.22. Transport across the nanowire was modeled

$$J_2 = [\frac{1}{R * Area_2}]V_2 \tag{3.28}$$

where $Area_2$ is the cross-sectional area of the nanowire. Transport across the forward Schottky barrier was modeled using TE

$$J_3 = [A^{**}T^2 exp\frac{-q\varphi_{Bn2}}{kT}]exp\frac{qV_3}{kT} \tag{3.29}$$

Equations 3.1-3.4 and 3.8-3.11 were used to evaluate V1, V2, and V3 in terms of V_{ext},

$$V_{ext} = V_1 + \frac{Area_1 RA^{**}T}{k}\gamma exp(\frac{qV_1}{\varepsilon,} - \frac{q\Phi_{Bn1}}{E_0})+ $$
$$\frac{kT}{q}\ln[1 + \frac{Area_1}{kTArea_3}\gamma * exp(\frac{qV_1}{\varepsilon,} - \frac{q\Phi_{Bn1}}{E_0} + \frac{q\Phi_{Bn2}}{kT})] \tag{3.30}$$

$$V_{ext} = \frac{\varepsilon,}{q}(\frac{q\varphi_{Bn1}}{E_0} + \ln[\frac{kV_2}{Area_1 * RA^{**}T\gamma}]) + V_2 + \frac{kT}{q}\ln[\frac{V_2}{Area_3 * RA^{**}T^2 exp\frac{-1\varphi_{Bn2}}{kT}} + 1] \tag{3.31}$$

69

$$V_{ext} = \frac{\varepsilon'}{q}\left(\frac{q\varphi_{Bn1}}{E_0}\right) + \ln\left[\frac{Area_3 * kT}{Area_1 * \gamma}\exp\left(\frac{-q\varphi_{Bn2}}{kT}\right)\left(\exp\frac{qv_s}{kT} - 1\right)\right] +$$
$$Area_3 RA^{**}T^2\exp\left(\frac{-q\varphi_{Bn2}}{kT}\right)\left[\exp\frac{qV_s}{kT} - 1\right] + V_3 \qquad (3.32)$$

$$\gamma = \sqrt{\pi E_{00}\left(qV_1 + \frac{q\varphi_{Bn1}}{\cosh\frac{E_{00}}{kT}}\right)} \qquad (3.33)$$

Equations 3.31-3.33 were solved numerically for the potential drops V_1, V_2, and V_3, with forward bias results shown in Figure 3.12. The voltage across the MSM nanocircuit is the sum $V_1 + V_2 + V_3$, with individual changes in V_1, V_2, and V_3. This implies that the slopes of V_1, V_2, and V_3 describe the behavior of the nanoFET. At voltage sweeps up to 5 V, V_3 with hole current contribution [59] was not observed and therefore the observed I-V behaviors were governed by the changes in V_1 and V_2. For both nanoFETs, V_1 dominated the sum at low voltages $V_{ext} \sim$ 0V - 1V and the device behaviors closely matched the reverse TFE exponential model. At higher voltages Vext $\sim$ 3V-5V, V1 contributed an almost-constant potential while V_2 changed almost exactly as V_{ext}, causing the I-V behavior to be similar to that of an ohmic device. The increasingly linear character of the I-V curves from 3-5 V was observed for nanoFET2 as shown in Figure 3.3. Observation of V_2 dominance for nanoFET1 from 2.5-5 V was restricted by the 1 A compliance, but a departure from a purely exponential behavior was observed $\sim$ 1.2-1.5V.

For nanoFET1, the changes in V_1 and V_2 shown in Figure 3.12(a) with corresponding inset boxes closely paralleled the increase/decrease in forward bias transmission probabilities shown in Figure 3.12(a). The results for nanoFET2 shown in Figure 3.13(b) demonstrated the PR V_1 dominance for all Vext within the voltage sweep. At 0 min, this immediately changed to V_1 versus V_2 behavior that paralleled the low energy part of the crossover transmission probability shown in Figure 3.13(c).

3.6.7 Barrier Modulation by Radiation

A first-time investigation of the Schottky barrier height and width described by potential drop V_1 as a function of time in the beam was then performed. The results indicated that the nanoFET1 $q\varphi_{Bn1}$ barrier decreased in both height and width up to 15 min and then increased, as shown in Figure 3.12 (a). NanoFET2 experienced a significant decrease in Schottky barrier width at 0 min (5 min shown) and a slow increase up to 30 min, as shown in Figure 3.12 (b). At 30 min, the barrier width was still less than its PR value. The nanoFET2 $q\varphi_{Bn1}$ barrier height increased slightly from PR to 0 min and then remained stable.
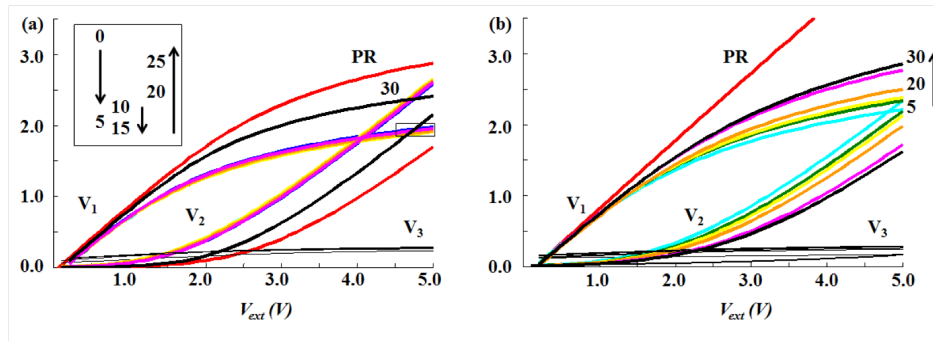
Figure 3.12 (a) Numerically solved potential drops V_1, V_2, V_3 as a function of Vext and time in beam for (a) NanoFET1 and (b) NanoFET2. Closely spaced V_1 variation (box) are shown inset.

3.7 Investigation of Additional Semiconductor Nanowires

Further investigation on the stability versus these materials properties for a range of real and simulated semiconductor nanowires in addition to GaN. Explore of the sensitivity of free carrier concentration n and temperature T to changes in effective mass m* and relative dielectric constant ε_r is also performed, as these quantities are all synergistically linked through a vital ratio kT/E_{00} that sets the scale of the tunneling contribution.
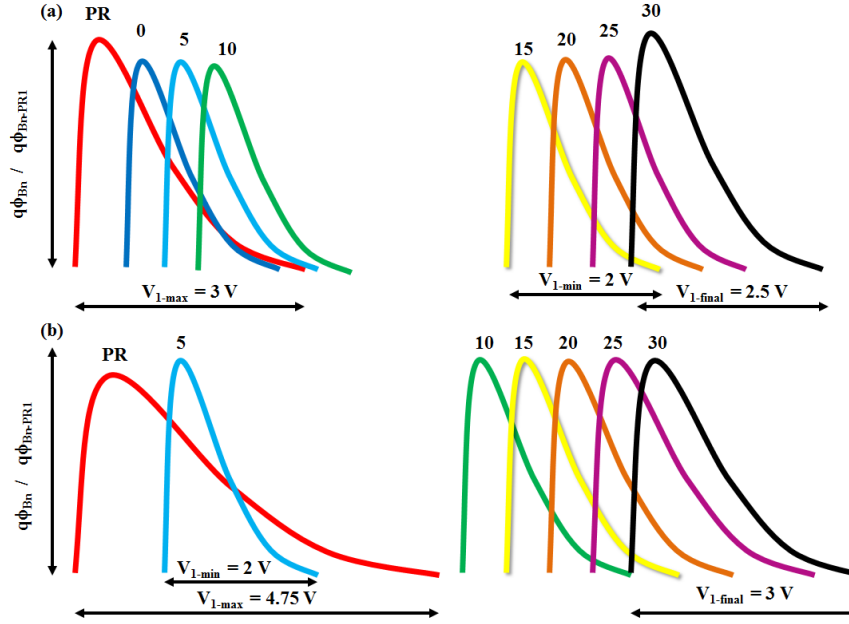
Figure 3.13 Effective barrier height and potential drop V_1 as a function of time in beam for (a) nanoFET1 and (b) nanoFET2. Barrier heights are accurately scled to the nanoFET1 PR height (Table 1). The maximum (-max), minimum (-min) and final (-final) V_1 values are identified.

3.7.1 Dependence on Effective Mass and Relative Dielectric Constant

MSM nanoFET devices present Schottky barriers at the contacts, and barrier manipulation is the key for electron transport through the device. Based on the work function of different material and the newly developed fitting method, one should be able to extract the ideal fitting range for each material. This study should lead to the more straightforward applications of thermionic field emission model for semiconductor nanowire devices.

3.7.2 Analysis of Reported and Simulated Semiconductor Nanowires

As discussed in detail in Refs. [87], a nanoFET is a metal-semiconductor-metal (MSM) device with reverse and forward biased Schottky barriers. The reverse bias metal-into-nanowire Schottky barrier dominates the transport when drain-source voltages are low to moderate, as was the case in this GaN experiments (5V). Using this stability approach, the

reverse TFE J-V curve is generated using known (generation) values for effective barrier height $q\varphi_{Bn}$ temperature T, and carrier concentration n. Fits performed on the generated curve using the Levenberg-Marquardt Algorithm are then used to identify stable parameter ranges.

$$J = [\frac{A^{**}T}{k}\sqrt{\pi E_{00}(V + \frac{\varphi_{Bn}}{\cosh^2(\frac{E_{00}}{kT})})\exp(\frac{-q\varphi_{Bn}}{E_0})}]\exp(\frac{qV}{\varepsilon,}) \tag{3.34}$$

$$E_0 = E_{00}\coth(\frac{E_{00}}{kT}) \tag{3.35}$$

$$\varepsilon' = \frac{E_{00}}{(\frac{E_{00}}{kT}) - \tanh(\frac{E_{00}}{kT})} \tag{3.36}$$

The materials properties effective mass m^* and dielectric constant ε_r appear together as the combined product $m^*\varepsilon_r$ in in E00, as shown in Equation 3.21. The impact of $m^*\varepsilon_r$ product variation on TFE stability was investigated over a realistic range from 0.1 to 8.0. The GaN, InP and PbTe choices were motivated by reported nanoFET investigations [87, 105, 106].

For barrier height $q\varphi_{Bn}$, stable regions and regions of catastrophic fit-failure progress toward lower values as a function. $m^*\varepsilon_r$ While for carrier concentration n, stable regions and regions of disastrous fit-failure progress toward higher values as a function $m^*\varepsilon_r$, as shown in Figure 3.14 (A-B). The results shown in Figure 3.14 demonstrate that an effective barrier height $q\varphi_{Bn} = 0.4$ eV and a carrier concentration of $\log(n) = 16.8$ could potentially be used to fit I-V data over the full range of Table 3.2 materials properties. These values were therefore used in the temperature sensitivity investigation.

Stable temperature regions exhibited no significant changes as a function of $m^*\varepsilon_r$ for values above GaN (simulated #2 and PbTe). Therefore, only GaN results are shown in Figure 3.14(c) as a starting point. However, increasing sensitivity to the decreases in $m^*\varepsilon_r$ was demonstrated for $m^*\varepsilon_r$ values below GaN (InP and simulated # 1). As $m^*\varepsilon_r$ values decreased, the temperature range for stable TFE curve generation contracted due to elimination of

Table 3.2 Real and Simulated Material Properties Used to Test the Stable Fitting Range

Material	$\frac{m^*}{M_0}$	ε_r	$m^*\varepsilon_r$
Simulated # 1	0.01	10	0.1
InP	0.077	12.4	0.95
GaN	0.27	10.4	2.81
PbTe	0.17	30	5.1
Simulated # 2	0.2	40	8.0

lower temperature values as stable solutions. For a $m^*\varepsilon_r$ value of 0.1, no temperatures were successfully fit. Decreasing the value of log(n) to 10 (to keep E00 constant) did not change the $m^*\varepsilon_r = 0.1$ outcome. Additional $m^*\varepsilon_r$ values between 0.95 and 0.1 were investigated and $m^*\varepsilon_r = 0.2$, with $m^* = 0.02$ and $\varepsilon_r = 10$, was established as a lower limit.
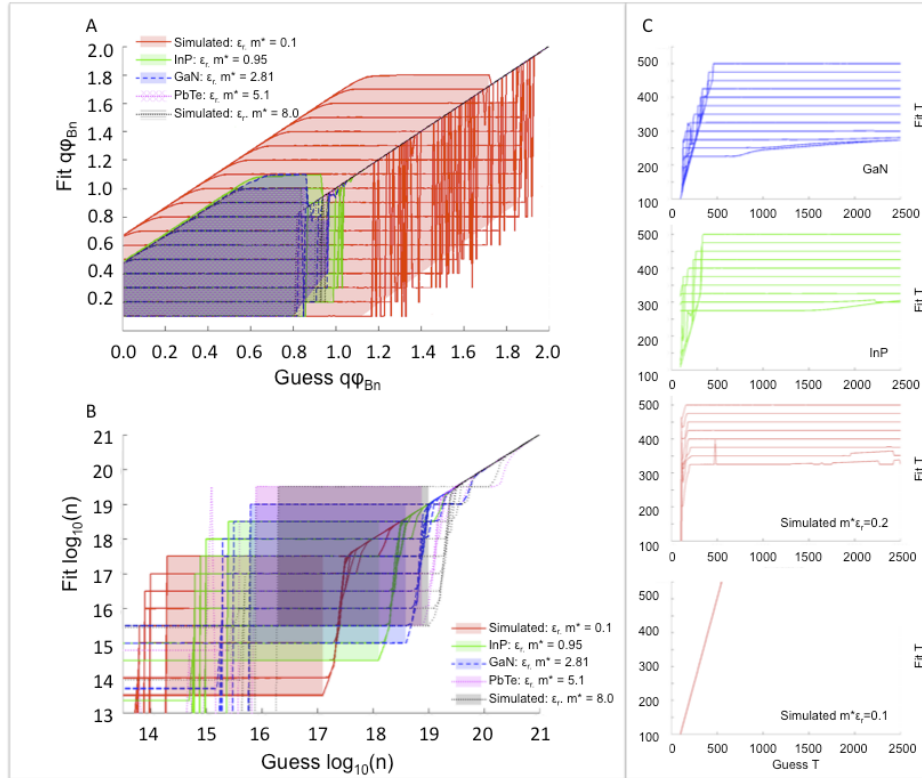

Figure 3.14 Graph show the stable fitting range for A) Barrier height B) Carrier Concentration and C) Temperature with varying material type.

3.8   Discussion

In recent work discussed here, development of a mathematical stability approach that greatly simplified the evaluation of the multivariate thermionic field emission parameters. This stability approach is a general method with potentially wide applicability, which requires only the effective mass m* and relative dielectric constant ε_r for a given semiconductor as inputs. A next step was to investigate the influence of these materials properties. Investigations indicated that stable TFE behavior may be achieved for a range of practical nanowires using $q\varphi_{Bn}$ = 0.4 eV, log(n) = 16.8 and T = 300K. These values could be used a safe starting point for TFE fits I-V data rather than literature values that may not have been acquired under TFE regime conditions. A previously unrecognized temperature sensitivity for stable TFE solutions as a function of decreasing m*ε_r was also identified. Finally, the first-time investigation of regime trends as a function of materials properties indicated that indicate that increasing values for m*ε_r for electronically heavier materials such as PbTe can shift Schottky barrier transport towards TE regime transport with less tunneling. This information can more precisely determine the circumstances under which a mathematically simpler TE fit may be safely used.

The electron transport in NanoFET is based on the ratio of E_{00} and kT. With a stable range of fitting established for a variety of materials, estimation of the transmission probability for each material with different m**ε_{00} value.

This is the report of a first investigation of the scaling ratio for tunneling kT/E_{00} over the stable carrier concentration ranges n for each nanowire type identified by its materials properties m*ε_r, beginning with InP. Temperature T was set to 300K to investigate room temperature behavior; this was within the stable range for all nanowires shown in Figure 3.18. At room temperature, the scaling ratio for tunneling is given by:

$$\frac{kT}{E_{00}} = 1.85 * 10^{-11} \text{eV} \sqrt{\text{cm}^3} * \sqrt{\frac{m^* \varepsilon_r}{n}} \tag{3.37}$$

The results for over the full n-stability range for each nanowire type are shown in Fig 2.14.

The high free carrier concentrations n typically reported for nanowire nanoFETs [97] (vertical dotted line) drives Schottky barrier transport into the TFE regime with kT/E_{00} values of about $1 < kT/E_{00} < 5$. The influence of materials properties $m^*\varepsilon_r$ indicates that increasing values for $m^*\varepsilon_r$ for electronically heavier materials such as PbTe will shift Schottky barrier transport towards TE region with less tunneling. Temperatures above or below 300K shift the Figure 3.14 curves up or down, which indicates an increase in the TE or the tunneling component.

3.9   Summary

The research in this chapter presents the only published real-time data for NanoFETs running under continuous high-energy heavy ion radiation for $\geqslant$ 30 minutes.This thesis study contributes successful development of a new stability approach that enables Thermionic Field Emission modeling of the electron transport mechanism through the Schottky barriers, which the experimental results indicated as key. The extracted device variables from the experimental data, plus a full metal- semiconductor-metal analysis, enables a detailed look at how the electrons are transported in a general Schottky barrier operation that applies to additional NanoFET device set-ups in other important radiation situations as well.

Experimental results shown in this thesis provide general as well as specific insights into how nanoFET designs, using barrier modulation and a capacitively decoupled nanowire channel, can survive SEE upset and continue to operate under heavy ion bombardment without shielding. As described in the Introduction chapter, radiation environments present enormous challenges to traditional-design electronics. Although cumulative ion effects can cause changes to device I-V characteristics, this does not diminish the potential of these devices to be used as replacements for future space missions. New design development is also in process, with a new radiation hardening emphasis on the non-oxide components such as the contacts and the nanowire surface states, as discussed in chapter 5 in this thesis.

CHAPTER 4

QUANTUM COMMUNICATION SAW DEVICE IN SPACE

4.1   Introduction

Despite the advancement in telecommunication technology in the recent years, space communications still live in the dial-up age as radio frequency driven modalities serve as the key communication method between spacecrafts and earth. Radio waves are mechanical waves, only reliable to a certain distance and bandwidth limited. Radio waves are also hard to secure or to repeat due to the long distances involved in space communication. Laser based space communication is the current cutting edge technology in development for the new generation telecommunication systems in space. Quoting from a recent NASAfacts release:

"During the past several decades, the volume of data from NASA′s missions has increased exponentially and is expected to continue at even greater rates. Although RF-based communications currently are the most reliable form of space communications, the radio and microwave portions of the electromagnetic spectrum are getting close to capacity. Laser communications will enable NASA to work within a new, less crowded section of the electromagnetic spectrum. Another motivation for exploring laser communications is the development of more efficient, cost effective space communications equipment. Because RF wavelengths are longer, the size of their transmission beam covers a wider area (about 100 miles); therefore, capture antennas for RF data transmissions must be very large. Laser wavelengths are 10,000 times shorter, allowing data to be transmitted across narrower, tighter beams. The smaller wavelengths of laser-based communications are more secure, delivering the same amount of signal power to much smaller collecting antennas[107]."

Laser transmission from the Earth to the moon and back again has recently been demonstrated [107]. It is anticipated that long distance space communication will be both laser and RF based.

By coincidental timing, quantum cryptography including both quantum communication and quantum computing is currently under intense development by several research groups and high-tech industries including Google, IBM and Microsoft. Quantum communication is of great interest to NASA for space communications, as it adds an additional layer of security. Quantum communication is under exploration for simultaneous insertion with the new laser communications methods. While long-distance quantum communication will be laser-based, the importance of a quantum communication relay is explained below, citing previous work done by the group of Applied Physics in University of Geneva [108].

Quantum cryptography is currently in the development stage. One implementation is to send bits as pulse position modulated (PPM) single photons down a fiber optic cable, and to use quantum complementarity to detect the presence of any eavesdropper. Experimental results are encouraging, including recent successful transmissions over a physical distance of 67km [109], and over 100km of fiber in the laboratory [110].

A limitation to the development of quantum cryptography is its performance over distance. Two effects come into play here. The first is the exponential loss of signal, and hence bit rate, with increasing distance. The second is the fundamental insecurity of the quantum crypto-system at long distances due to a roughly constant level of noise dominating the exponentially decreasing signal. Both these obstacles can be overcome in theory using a quantum repeater [111]. This is the idea of breaking up the channel into several short sections and creating a perfect entangled pair spanning each section, before using entanglement swapping to make a single entangled pair spanning the whole channel. The entangled pair can then be used to make a secret key, using for example the Ekert protocol [112]. In order to make a perfect entangled pair across a single section, it is possible to send many pairs, each of which arrives with a small amount of noise, and possibly not at all. A quantum memory, non-demolition measurement, and entanglement purification [113] could then be used to make one perfect entangled pair.

The main problem with such a scheme is precisely that it requires a complicated set of

quantum operations, a quantum memory and a photon non-demolition measurement. All these seem impractical in the near future.

A simpler scheme currently under investigation by our group and others is the quantum relay. This works in the same way as the quantum repeater, only without the entanglement purification, the quantum memory, or the non-demolition measurement. The exponential loss of signal with distance is accepted rather than combatted. An increase in the maximum distance over which secure quantum key distribution is achieved through an increase in the signal-to-noise ratio at each detector.

In this thesis work, the goal is to develop a simple quantum communication device to be implemented on a CubeSat platform to serve as a relay for quantum signals. In theory, the relay device is functional whether the signal is from traditional RF communication system or the new optical system. The research here is in an entirely new area and the work is still in an early stage, with focus on quantum bit (qubit) generation/entanglement, spatial and temporal coherence, and signature detection. Traditional communication protocol and measurement concepts such as overall bandwidth are not currently under investigation by any group; these issues will be addressed later when generation, transport and detection concepts are established. The candidate's work presented in this thesis is part of the public information allowed by agreements with our NASA collaborator. There is no detailed data on any similar devices to be compared or studied to our knowledge. The few reports of successful quantum communications in space all refer to long distance point-to-point laser-based experiments without relays. Also, this information is largely in the form of public news reports with limited scientific data provided, e.g China?s quantum communication satellite experiment launched in 2017.

As described in the introduction chapter, details of the initial prototype fabrication are presented here. The concept involves adding a propagating SAW wave as a "flying qubit" component to the quantum communication device layout shown in Figure 4.1. The idea is based on the "flying qubit" design for an ideal heterostructure-based 1D channel explored in

Ref. [52] and found to be viable. Many any details of the interactions between the dynamic potential induced by propagating SAW wave with the reduced dimensionality electron pool were not investigated. One key aspect not previously reported is that a SAW wave consists of a longitudinal as well as a transverse component. In the present work, the focus is on the effects of the longitudinal component interaction with the reduced dimensionality 1D electron pool and find that it can significantly influence both transport uniformity and transmission. Furthermore, the present analysis is developed for a realistic finite width 1D channel.
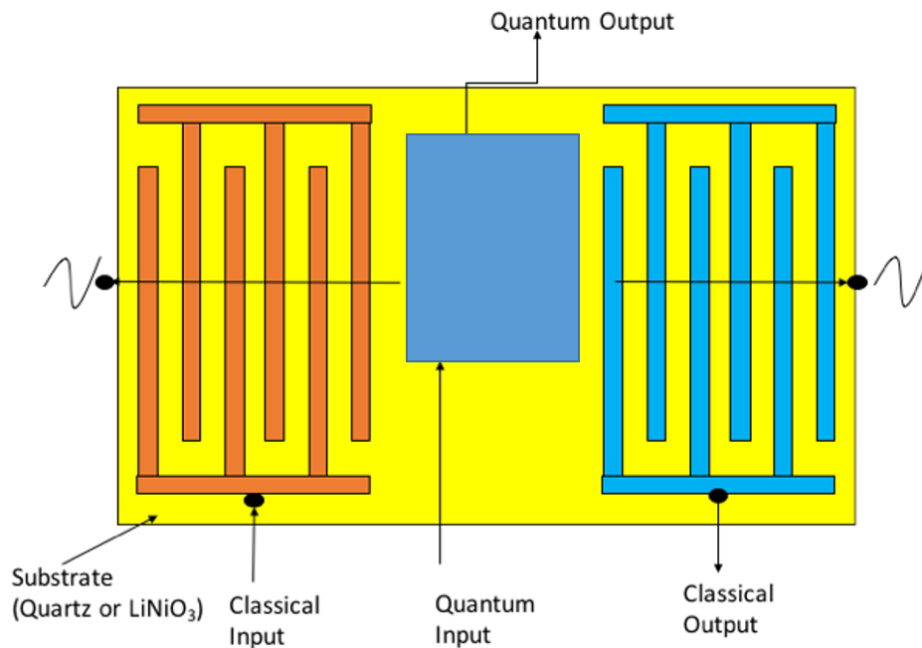
Figure 4.1 Solid State Quantum Relay Device. Qubit generation system is redacted and represented by blue box.

4.2 Surface Acoustic Wave Device

Surface acoustic wave (SAW) is a mechanical wave motion travel along the surface of the material, caused by the deformation of material, initially discovered by Lord Rayleigh in 1885[114]. This effect can be demonstrated with sound traveling on metal surface or ringing bell as low-loss propagation of acoustic waves in audible frequency range. In solid materials,

surface acoustic waves propagate in two directions, one moving longitudinal wave that is parallel to the displacement vector and the other standing wave which is a shear wave that is normal to the displacement vector.

In the case of piezoelectrical materials, the mechanical stress and strain of the material can be induced by electrical and mechanical disturbance, meaning an electric field in the form of voltage, can generate the necessary mechanical deformation represented by surface acoustic waves. This conversion between electric and mechanical energy is called transduction, this unique relationship combined with another critical property of the longitudinal part of the SAW is that the speed of the wave is strictly determined by the material itself, is the fundamental concept of a SAW device.

Piezoelectricity exists only in material that is anisotropic, meaning in general a crystalline is being used and the material properties is orientation dependent based on the atom arrangement of the crystal. Narrow down to SAW substrate, the SAW properties is then decided by the cut of the substrate from the original material.

Quartz, lithium niobite and lithium tantalite are the three-general material used to build commercial SAW devices. Standard orientations have been developed and used for the variety of applications, depends characteristics such as operational frequency range, temperature coefficient, electrical impedance etc. The following Figure 4.2 shows the different cut orientation on a quartz crystal.

SAW based device is widely used in todays electronics, mainly as filters in signal processing system builds due to nature of the SAW acting as band passing devices, or oscillators since SAW is easy to access (surface of material), can be easily interact with achieving wave feature such as transduction, reflection, wave-guiding and so on[116, 117, 118].

A standard SAW device consists two set of interdigital transducers (IDTs) made out of metal electrodes, invented in 1965 [119], these comb-like IDTs can be used to generate and detect SAW via transduction. For commercial and research requirements, electoral is then wired to the IDTs to provide inputs/outputs, wave reflector or absorber are also commonly
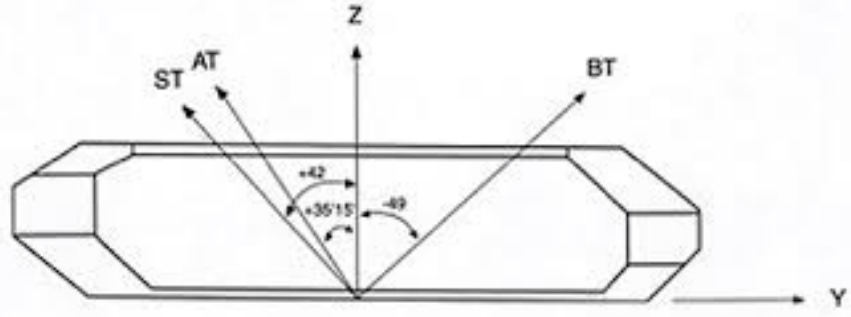
Figure 4.2 Standard crystal cut orientation on a quartz crystal. Image Credit: MEC Quartz Crystal[115].

used to provide boundary condition at each end of the device, Figure 4.3 shows the design of the SAW device used in this thesis. For this research, to server as electrons boats, the accurate acoustic resonance frequency as well as slow wave speed of the SAW make it the ideal candidate for an experimental quantum communication relay.
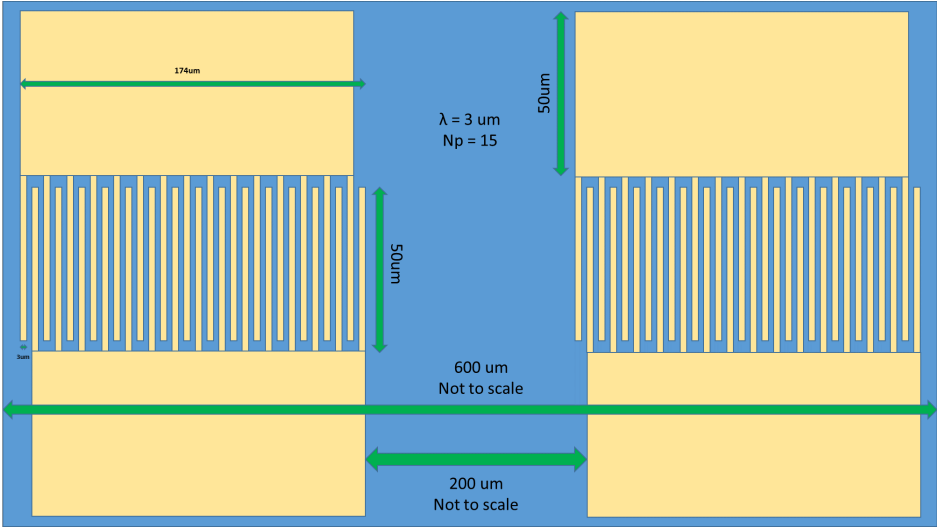
Figure 4.3 Designed SAW device with (3μm) minimum feature and 15 IDT pairs.

4.2.1   Design of SAW Device

Consider the capability of quantum encoding media and device operating frequency, a ST-X cut quartz is chosen to be the device substrate. Lithium niobite are known to have better

82

Table 4.1 Designed SAW device Resonance Frequency

λ	f
7μm	451.4 MHz
5μm	631.6 MHz
3μm	1.05267 GHz
1μm	3.158 GHz

SAW propriety but it is highly sensitive to heat treatment compared to quartz [120].

For this investigation, the quartz substrate was purchased from MTI corporation, the 10x10x0.5 mm substrate is >99% SAW grade with acoustic velocity of 3158 m/s. To achieve optimum amplitude of the surface wave, the wave length λ requires to be the same of the pitch length (separation) of the IDTs, λ also defines the acoustic resonances frequency of SAW device, this relationship is shown in equation 4.1 below. On the other hand, the number of IDT pairs Np determines the bandwidth of the device, this approximately given by equation 4.2.

$$\omega_{IDT} = 2\pi f_{IDT} = \frac{2\pi V_0}{\lambda} \tag{4.1}$$

$$BW = \frac{f_{IDT}}{N_p} \tag{4.2}$$

Due to the design requirement of the quantum communication relay and the fabrication capacity, the following design parameter based on resonance frequency and bandwidth is proposed, as shown in Table 4.1 and 4.2. Figure 4.4 shows the design diagram used for a single device with Figure 4.5 shows the final design diagram layout on the wafer substrate(mask) , four designs are chosen to be made in this fabrication batch, that is 3um and 5um width IDTs combined with 15 and 25 IDT pairs.

Table 4.2 Designed SAW device Bandwidth

N$_p$	Bandwidth(7μm)	Bandwidth(5μm)	Bandwidth(3μm)	Bandwidth(1μm)
15	30.07 MHz	42.1067 MHz	70.1778 MHz	210.533 MHz
25	18.044 MHz	25.264 MHz	42.1067 MHz	126..320 MHz
50	9.022 MHz	12.623 MHz	21.0533 MHz	63.160 MHz
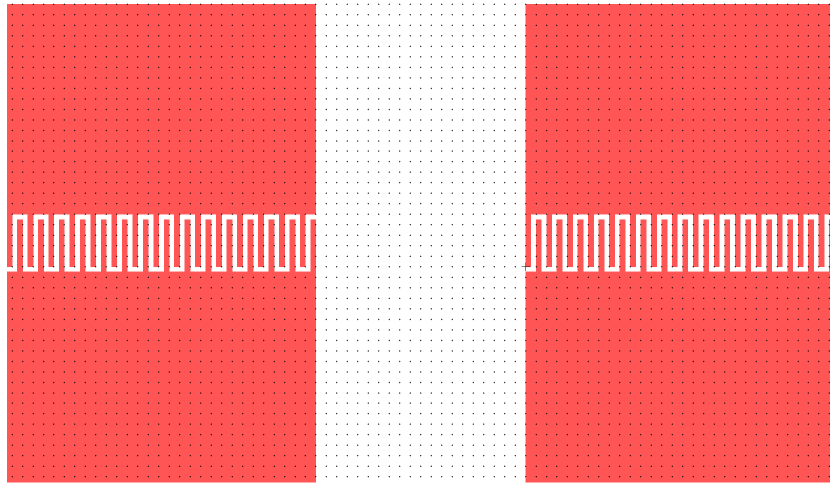
Figure 4.4 Mask design show (3μm) minimum feature and 15 IDT pairs on a single layer.
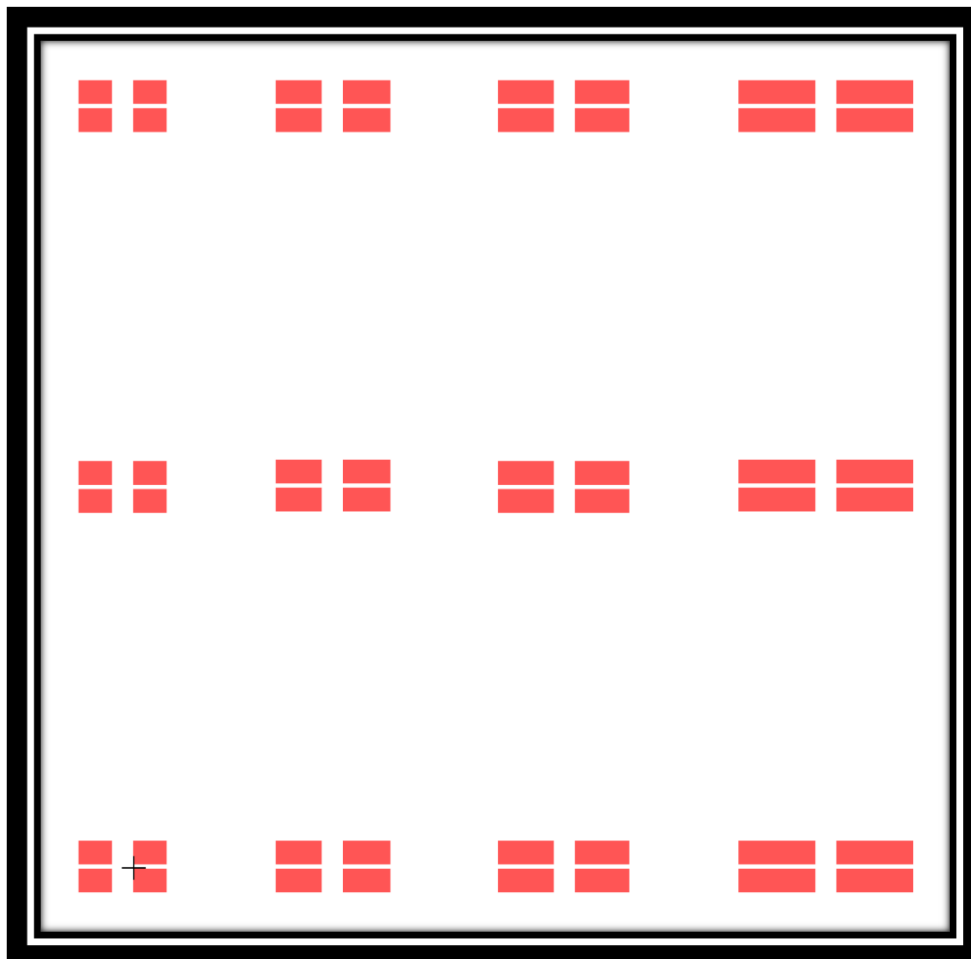
Figure 4.5 Full Mask Design showing all twelve devices on a single wafer surface.

4.2.2 Fabrication of SAW Device

The fabrication of the SAW device is done at Lurie Nanofabrication Facility (LNF) located at University of Michigan. LNF provides state art of the art clean room environments (down to class 10) and over 120 major state of the art tools for 4 and 6 inch processing, the primary cleanroom supports with silicon, compound semiconductors and organic material, for the fabrication of devices and microsystems (MEMS) with feature sizes down to 10 nanometers [121].

The recipe used for the fabrication follows a simple deposition and lift off process, a commercial lift off resist (LOR) is used as sacrificial layer to achieve high resolution required for the IDTs. The designed fabrication recipe is show in Figure 4.6.
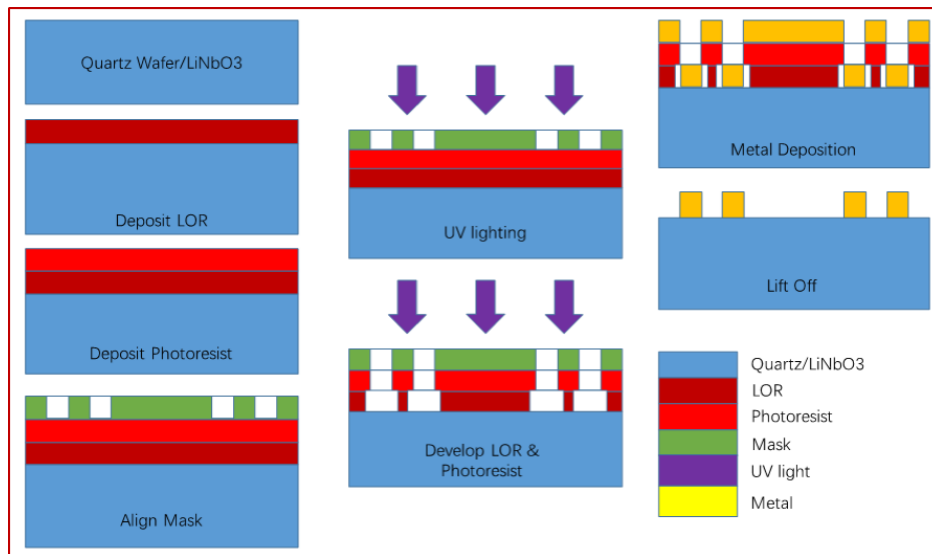
Figure 4.6 Fabrication Recipe for SAW device showing the process lift off using LOR layer.

4.2.3 Instruments used fabricate the SAW device

Heidelberg Upg Mask 501 Maker — This works as a micro pattern generator for low volume masking making, with minimum structure size of 1um in high precision writing mode. The mask maker contains a LED bulb with wavelength of 390 nm, this is used to expose the

photoresist on the masks after alignment. This system is also capable of creating 3D (grey scale) structures in thick photoresist in a single pass [122].

CEE 100CB Photoresist spinner — This is the general spinner used at LNF to cover sample substrate with photoresist, the spinner can achieve 5k rpm spin rates with capability of accepting wafer up to 6 inches [123].

MA/BA-6 Mask/Bond Aligner — Used to expose photo-definable materials, this is a contact lithography aligner, meaning the substrate is in direct contact with the top side of the mask surface, making a 1 to 1 ratio in mask feature size versus wafer feature size. The broadband light source in this unit is calibrated to 20mJ/sec with 405 nm peak, the minimum feature size can go down to 2μm [124].

YES-CV200RFS(E) — Produced by Yield Engineering Systems, this is a single wafer, downstream plasma strip/descum tool. This is used to fast plasma stripping of photoresists and other organic materials from the wafer, this tool mainly used oxygen plasma for organics removal but capable for using other process gases as well depends on the application [125].

Enerjet Evaporator — The electron beam evaporator used to deposit metal layer onto the wafer, uses a small point sources and long throw distances leads to very directional deposition with minimal heat transfer, this make the tool ideal to use for lift-off applications. This tool has high deposition rate up to 15 Å per sec on multiple wafers[126].

4.2.4 Fabrication Process

A ST cut Quartz wafer is cleaned with Piranha Solution (20% Hydrogen Peroxide 80% Sulfuric Acid) then inspected under optical microscope, mask is made with Heidelberg Mask Maker and cleaned with Nano-Strip.

Photo resist (Shipley 1800 Series) is coated and baked onto the wafer using CEE 100CB spinner and hotplate. Lithography is then done with a mask aligner. Fully developed device runs through a de-scum process to remove the organic residue.

Finally the wafer is put into EnerJet Evaporator for metallization, a layer of 100nm aluminum is deposited onto the wafer. The device is then lifted off using photoresist remover. The completed wafer is shown in Figure 4.7 with close ups showing clean edge IDTs in Figure 4.8.

Twelve SAW devices is made on a single quartz wafer, they are delivered to NASA and are currently under investigation and testing by our collaborators.
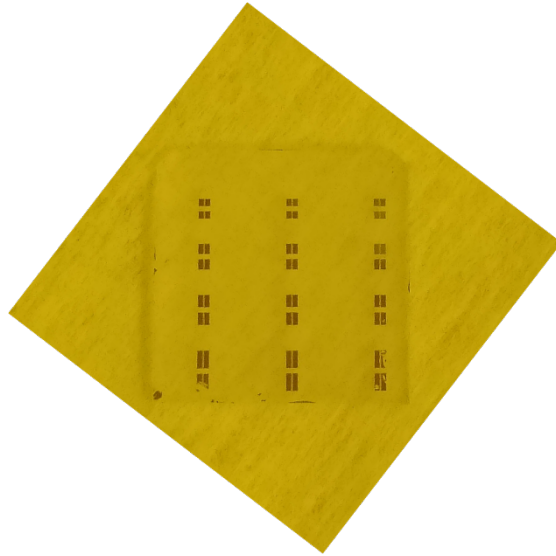
Figure 4.7 Completed Wafer with devices under optical microscope, yellow light is from clean room lighting on lab paper, substrate is transparent.
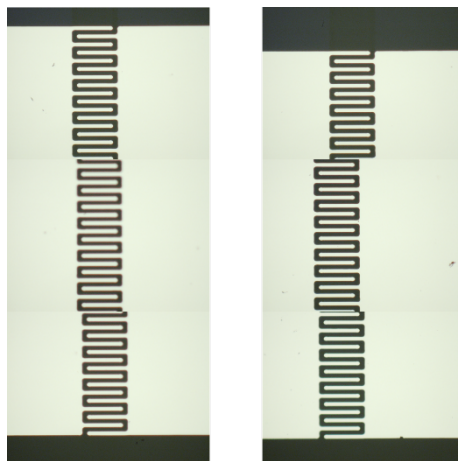
Figure 4.8 Image on IDTs under microscope, showing clean edges and separation in between each IDTs.

4.3 SAW integration with Quantum Wire Model

4.3.1 Finite Width Channel

Key features of the configuration are identified in Fig 3.9 GaAs-AlGaAs layers are used to create a 2D quantum well in the z-direction (dotted line) and a split gate introduces additional confinement in the y-direction that depends on width W (inset above). The actual motion of the GaAs substrate in response to the propagating SAW wave is a retrograde motion that includes both longitudinal and transverse components (inset above).
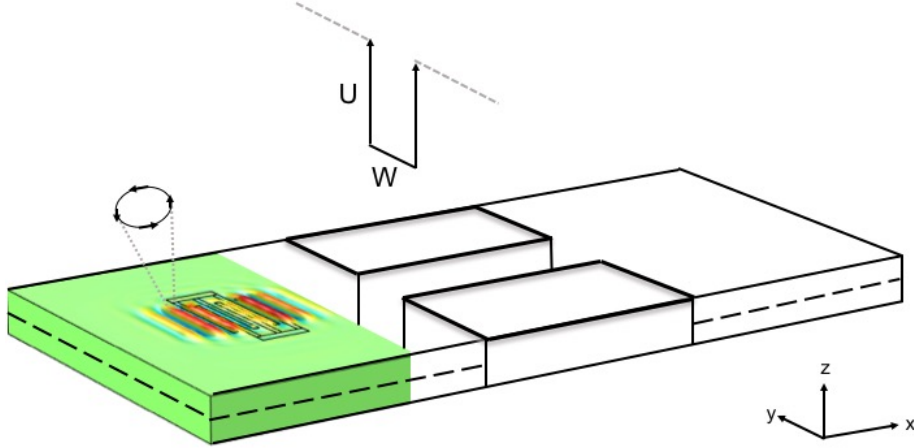
Figure 4.9 2D quantum well in z dotted line) with additional width W dependent quantum well in y (inset above). GaAs response to propagating SAW wave includes both longitudinal and transverse components (inset above). Modeling is done by Kan Xie using COMSOL.

One can formulate 1D number density n_L (#/length) for electrons in the channel and then investigate how this is impacted by the addition of the SAW wave potential longitudinal component. When the z- and y- confinements are modeled using an infinite potential well approximation, 3D unrestricted motion (equation 4.3) is reduced to 1D in the x-direction (equation 4.4). E_C is the GaAs band-gap energy, 1.43 eV.

$$E = E_c + \frac{h^2 k_x^2}{2m_x^\Phi} + \frac{h^2 k_y^2}{2m_y^\Phi} + \frac{h^2 k_z^2}{2m_z^\Phi} \tag{4.3}$$

$$E = E_c + \frac{h^2 k_x^2}{2m_x^\Phi} + \frac{n_y^2 \pi^2 h^2}{2m_y^\Phi L_y^2} + \frac{n_2^2 \pi^2 h^2}{2m_z^\Phi L_2^2} \tag{4.4}$$

If the lowest energy level 2D quantum well and the band-gap energy are combined in E_S, and the width W dependent 1D quantum well is investigated at its lowest energy level E_1, then:

$$E_S = E_c + \frac{1^2 \pi^2 h^2}{2m_z^\Phi L_Z^2} \tag{4.5}$$

$$E_1 = 1^2 \left(\frac{\varphi^2 \hbar^2}{2m_y^* W^2} \right) \tag{4.6}$$

$$E = E_S + \frac{\hbar^2 k_x^2}{2m_x^*} + i^2 E_1 \tag{4.7}$$

$$k_{x,i} = \sqrt{\frac{2m_x^*}{\hbar^2}(E - E_S - i^2 E_1)} \tag{4.8}$$

The number density n_L in the channel is investigated in the degenerate regime as the energy level limitations in the reduced dimensionality material force the fermi energy level E_f above the bottom of the conduction band:

$$n_L = \int N(E) O(E_f - E) dE \tag{4.9}$$

The total number density of states in k-space, when converted to E-space using equation 3.8, gives:

$$N_t(\bar{K}) = N_t(k_{x,i}) = \frac{2k_{x,i} x 2}{(n_x = 1)\frac{2\pi}{L_x}} \tag{4.10}$$

$$N_T(E) = L_x \frac{2}{\pi} \sum_i \sqrt{\frac{2m_x^*}{\hbar^2}(E - E_S - i^2 E_1)} \tag{4.11}$$

which produces an energy density of states N(E) and a number density nL given by:

$$N(E) = \frac{2}{\pi} \frac{d}{dE} \left(\sum_i \sqrt{\frac{2m_x^*}{\hbar^2}(E - E_S - i^2 E_1)} \right) \tag{4.12}$$

$$n_L = \int \frac{2}{\pi} \frac{d}{dE} (\sum_i \sqrt{\frac{2m_x^*}{\hbar^2}(E - E_S - i^2 E_1)}) O(E_f - E) dE \qquad (4.13)$$

$$n_L = \frac{2}{\pi} \sum_i \sqrt{\frac{2m_x^*}{\hbar^2}(E - E_S - i^2 E_1)} \qquad (4.14)$$

Conventionally, dimensionless $n_L W$ is investigated through multiplication by $1 = E1/E1$ while using the effective mass near equality $m_x^* = m_y^* = m_z^*$ in GaAs as a direct band-gap material.

$$n_L W = 2 \sum_{i=1} \sqrt{\frac{(E_f - E_S)}{E_1} - i^2} \qquad (4.15)$$

and plotted with x = (Ef ES)/E1 as a running variable as shown in Fig 4.7. Specific values can be identified by matching the 2D-1D boundary conditions:

$$E_f - E_S = \frac{nS}{\frac{m^*}{\pi \hbar^2}} \qquad (4.16)$$

The dotted lines in Figure 4.10 show GaAs results for $n_S = 5 * 10^{11} cm^- 2, m_* = 0.07 m_0$. The E_1 values (equation 4.4) correspond to widths W = 1000 Angstroms (Å), 500 Å and 100 Å. For 1000Å and 500 Å, there are, respectively, 5 and 3 channels available for transport. For 100 Å, there is no transport because $E_f - E_S/E_1$ is below the cut-off for the i = 1 channel.

4.3.2   Longitudinal Perturbation

If nL is not normalized as dimensionless as in equation 3.15, then the number density is given by:

$$n_L = \frac{2}{\pi} \sum_i \sqrt{\frac{\pi 2}{W^2} (\frac{E_f - E_S}{E1} - i^2)} \qquad (4.17)$$

The width-dependent number densities for W = 1000 Å and 500 Å are shown in Figure 4.8(a) and 4.8(d). As expected, nL is higher in the narrower channel. Another effect of the finite width W seen in both Figure 4.8(a) and 4.8(d) and also in Figure 4.7 is the rounded nature of each step, in contrast to a textbook 1D flat-step staircase [56].
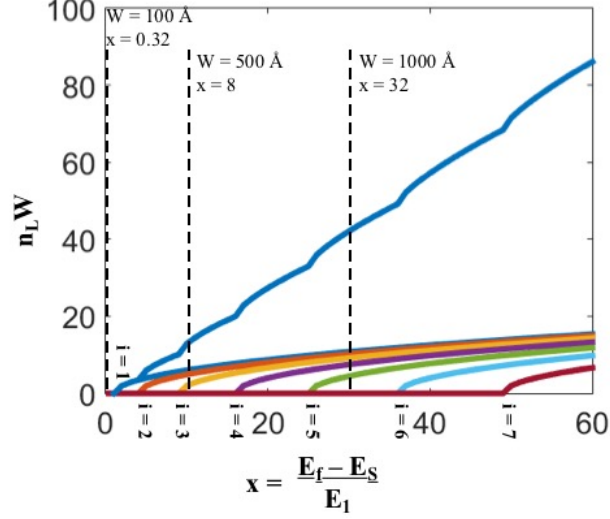
Figure 4.10 Normalized 1D electron number density. The number of channels available for transport has dropped from 5 to 3 to none as a function of the channel width.

The effect of the SAW wave longitudinal component is to introduce a perturbation to the local potential that can impact the x-momentum:

$$p_x \Rightarrow p_x + dp_x \tag{4.18}$$

$$\hbar k_x \Rightarrow \hbar(k_x + \varepsilon) \tag{4.19}$$

When the derivation of n_L is repeated with this perturbation included, a new quadratic expression for kx is found in which equation (4.24) replaces equation (4.8):

$$\frac{\hbar^2 k_x^2}{2m^*} \Rightarrow \frac{\hbar^2}{2m^*}(k_x^2 + 2\varepsilon k_x + \varepsilon^2) \approx \frac{\hbar^2}{2m^*}(k_x^2 + 2\varepsilon k_x) \tag{4.20}$$

$$E = E_S + \frac{\hbar^2}{2m^*}(k_x^2 + 2\varepsilon k_x) + i^2 E_1 \tag{4.21}$$

$$k_{x,i}^2 + 2\varepsilon K_{x,i} = \frac{2m^*}{\hbar^2}(E - E_S - i^2 E^1) = C(i) \tag{4.22}$$

$$k_{x,i}^2 + 2\varepsilon k_{x,i} - C(i) = 0 \tag{4.23}$$

92

$$k_{x,i} = \frac{-2\varepsilon \pm \sqrt{(2\varepsilon)^2 - 4(1)(-C(i))}}{2(1)} = -\varepsilon \pm \sqrt{\varepsilon^2 + C(i)} \tag{4.24}$$

This produces an energy density of states N(E) and a number density nL given by:

$$N(E) = \frac{1}{L_x} \frac{d}{dE} (L_x \frac{2}{\pi} \sum_i (-\varepsilon \pm \sqrt{\varepsilon^2 + C(i)})) \tag{4.25}$$

$$n_L = \frac{2}{\pi} \sum_i (-\varepsilon \pm \sqrt{\varepsilon^2 + [\frac{\pi^2}{W^2}(\frac{E_f - E_S}{E_1} - i^2)]}) \tag{4.26}$$

Equation (4.26) reduces to equation (4.17) when ε goes to zero.

4.3.3 Effects on Uniformity and Transport

The effects of perturbation on transport in the $+kx$ direction are considered in this paper:

$$n_L = \frac{2}{\pi} \sum_i (-\varepsilon + \sqrt{\varepsilon^2 + [\frac{\pi^2}{W^2}(\frac{E_f - E_S}{E_1} - i^2)]}) \tag{4.27}$$

Because the second term under the square root is scaled by π^2/W^2, the numerical value of can be large yet remain small in comparison. Values of $\varepsilon = \pm 10^8$ were used to investigate this effect. Both positively and negatively signed perturbations $\pm \varepsilon$ are shown to influence n_L, through the introduction of shifts that affect both quantum channel accessibility and number density n_L allowed occupation. The results for physical channel width $W = 1000$Å are shown in Figure 4.11. The quantum staircase is shifted toward lower values on the normalized energy x-axis by an amount equal to 10.1 for both $\pm\varepsilon$.

Further shifts dominated by $\pm\varepsilon$ appear on the number density n_L y-axis. For the previously investigated normalized energy of $(E_f E_S)/E_1 = 32$, the $-\varepsilon$ longitudinal perturbation reduces the number of quantum channels (staircase steps) available for transport from 5 to 3, although a higher n_L occupancy is allowed. For the $+\varepsilon$ longitudinal perturbation part of the retrograde motion cycle, the number of quantum channels available for transport is reduced from 5 to 1, with a lower allowed n_L occupancy.
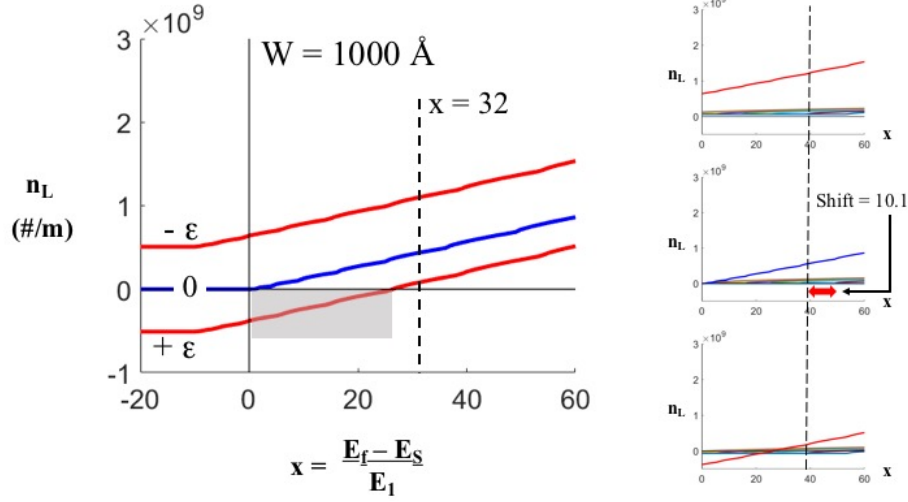
Figure 4.11 For width W = 1000Å, longitudinal perturbations shift the quantum staircase up or down by approximately by $\pm\varepsilon$ and towards lower normalized energy values by an amount 10.1, reducing the quantum channel accessibility and changing the number density n_L allowed occupation.
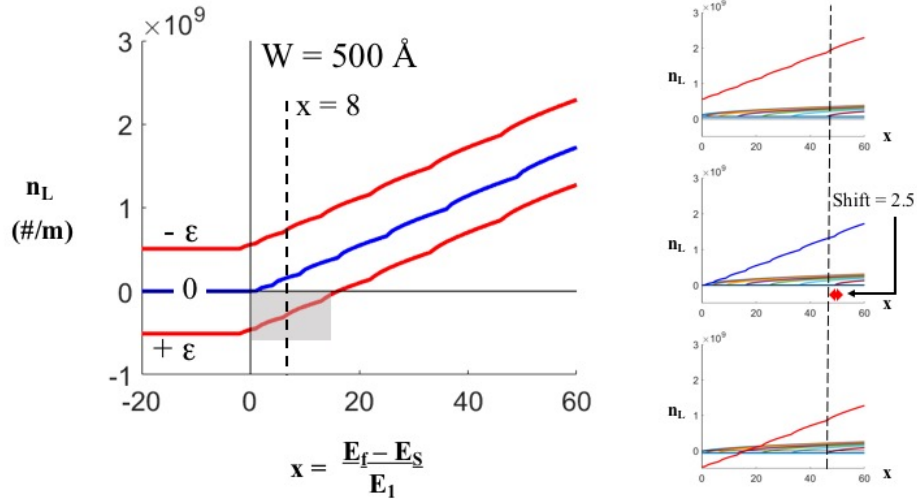
Figure 4.12 For width W = 500Å, longitudinal perturbations shift the quantum staircase up or down by approximately by $\pm\varepsilon$ and towards lower normalized energy values by an amount 2.5, reducing the quantum channel accessibility, to 0 for the $+\varepsilon$ longitudinal perturbation, and changing the number density nl allowed occupation.

The results for physical channel width W = 500Å are shown in Figure 4.12. The quantum staircase is shifted toward lower values on the normalized energy x-axis by an amount equal to 2.5 for both $\pm\varepsilon$, and up and down on the number density n_L y-axis by approximately$\pm\varepsilon$.

94

For the previously investigated normalized energy of $(E_f E_S)/E_1 = 8$, the $+\varepsilon$ longitudinal perturbation reduces the number of quantum channels available for transport from 3 to 1, with a higher n_L occupancy. From a uniformity perspective, this may be a desirable outcome. For the $+\varepsilon$ longitudinal perturbation part of the retrograde motion cycle, there are 0 quantum channels available for transport.

4.4 Conclusions

Flying qubit designs have emerged as a new approach for adding a dynamic control to solid-state qubit implementations including heterostructure-based electron gas implementations. The flying qubit approach utilizes the potential minimum of a SAW wave for the capture and transport of a single or few electron(s) from a reduced dimensionality electron pool. Many precise details of the interactions of the dynamic potential induced by propagating SAW wave with the reduced dimensionality electron pool remain to be investigated. In the present work, investigation of the SAW wave longitudinal component modeled as a perturbation to the local potential that can impact the k_x momentum in the transport direction. This led to the derivation of a new quadratic expression for k_x (equation (3.24)) and a new expression for n_L (equation 4.26).

A significant effect of positive or negative longitudinal perturbations on $+k_x$ electron transport is the introduction of shifts that can affect both quantum channel accessibility and number density nL allowed occupations. This indicates that the longitudinal component of SAW wave retrograde surface motion needs to be taken into account in heterostructure-based flying qubit designs. Furthermore, the reduction in quantum channel accessibility indicated by this research results could, with careful device engineering, lead to implementations with a more uniform electron pool, which can be more easily aligned into uniform spin states for entanglement. Work is continuing in the group to explore increasingly accurate SAW wave-electron pool interaction models to guide experimental tests.

CHAPTER 5

CONCLUSIONS AND FUTURE WORK

5.1 Summary of Contributions

In this thesis work, three types of nanomaterial and nanomaterial-enabled devices targeted to space applications have been investigated. Unique radiation studies were performed at the National Superconducting Cyclotron Laboratory at Michigan State University on two sets of GaN nanowire-based Field Effect Transistors. The analysis and interpretations developed in this thesis enabled a brand new look at heavy ion interactions with these nanoscale materials and devices. Heavy ions are an extremely penetrating component of space radiation that require massive shielding to exclude. However, the current trend in space exploration is strongly toward the new generation of spacecraft with significantly reduced size, weight, and power (SWAP) that cannot carry the traditional complements of radiation and thermal shielding. Work in this thesis supports the conclusion that nanomaterials and devices offer inherent resiliencies.

The Carbon Onion investigations of Chapter 2 have identified key information regarding the influence of initial polygonal character and stored mechanical energy on radiation performance. Previously, increase in polygonal character was the accepted standard for good Carbon Onions. For use as space lubricants however, this thesis work revealed that less polygonal Onions are a better starting point. The probable mechanism for radiation interaction was also identified, facilitating further investigations.

Chapter 3 of this thesis presents the only published real-time data for NanoFETs running under continuous heavy ion radiation for more than 30 minutes. This thesis study contributes successful development of a new stability approach that enables Thermionic Field Emission modeling of the electron transport mechanism through the Schottky barriers, which the experimental results indicated as key. The extracted device variables from the experimental

data, plus a full metal- semiconductor-metal analysis, enables a detailed look at how the electron are transported in a general Schottky barrier set-up that applies to similar device set-ups in other important radiation situations as well.

In Chapter 4, initial results from ongoing research that shows that how a surface acoustic wave (SAW) device can be implemented as a quantum Qubit carrier is presented. In a field dominated by theoretical studies, actual SAW devices were designed, simulated, and fabricated and tests by NASA collaborators are proceeding.

5.2   List of Problems Solved in This Thesis

This work addresses the following:

1. Study on carbon onion interaction with heavy ions, present experimental results of how carbon onion grew in different temperature take on heavy ion damage.

2. Based on experimental result, show possible mechanism that leads to carbon onion breakage under heavy ion radiation.

3. Analysis of the first ever real-time nanoFET I-V data obtained under 30 minutes of continuous heavy ion radiation that accurately simulates space energies and charges.

4. In-depth study of the correct Thermionic Field Emission model for electron transport through metal-semiconductor Schottky barrier, including contribution to development of new stability approach that enables multivariate Thermionic Field Emission model use. This is a contribution for analysis of other Schottky barrier devices as well.

5. Investigated how heavy ion radiation can modify Schottky barrier, in terms of barrier heights, widths and transmission probabilities, as a function of time in beam.

6. Constructed full metal-semiconductor-metal model of NanoFET devices and extracted voltage drops across internal regions. Provided first-time analysis of how voltages

drops evolved changed as a function of time in beam and also potential difference, which changes during device operation.

7. Explored the possibility of using a surface acoustic wave set up to carry few electrons between distances in a coherence-preserving state.

8. Designed, simulated, and fabricated SAW devices on a Quartz Substrate, which are currently under test at NASA.

5.3 Future Work

5.3.1 Radiation Study for Carbon Lubricant in Space

The radiation effect study for nanocarbon-based sold lubricants continues with further investigations of the sp2/sp3 composition as well as the further research on energy analysis. Two area of interest still exists. First, the exact dislocation mechanism and how it is initiated by heavy ion interaction is yet to be determined. Graphene layer linking and unlinking and other types of rearrangement have been simulated and studied by other groups [73, 74]. However, the data in the present research is unique because the linking/unlinking effects was the result of heavy ion radiation. This calls for further investigation on how the changes are related to heavy ion interaction.

Initial work has been performed using EELS showing sp2/sp3 ratio difference between COs synthesized at different temperature in pre and post radiation conditions. Additionally, to achieve desired lubricant performance in space, problems such as packaging and lifecycle under irradiation are still due for further investments in research.

5.3.2 NanoFETs as Space-Based Electronics

Three key nanoFET components can be affected by radiation. These are the metal-semiconductor contacts, the nanowire itself and the insulating layer. In traditional MOSFET devices, radi-

ation damage is most likely to manifest itself in the insulating layer by changing the insulator capacitance C_i and introducing unwanted threshold voltage shifts. This is because the on/off threshold voltage in a MOSFET is strongly capacitively coupled to the insulating layer, and any change to the Ci severely affects the device performance as shown in equation

$$V_{th} = V_FB + \Psi_S + \frac{Q_B}{C_i} \tag{5.1}$$

$$V_{FB} = \varphi - \frac{Q_f + Q_m + Q_{ot}}{C_i} \tag{5.2}$$

This thesis work is the first to investigate radiation resilience in a GaN nanoFET architecture. The immediate nature of the observed response to beam exposure indicates that, for GaN nanoFET devices, the contacts are the components most likely to be affected by radiation instead of the insulating layer[42].

The analysis for radiation resilience in the current work in chapter 3 is focused on the radiation effects at the nanoFET contacts. In continuing work, using extraction of V_1 form the MSM formulation to guide the investigation of a charge layer model(s) at the contacts. This will enable the further extraction of depletion region width as a function of time in beam.

Future work will also include investigation of the oxide/insulating layer and the nanowire itself. The thermal oxide volume in the active nanocircuit region received 0.0228 Gray (Gy: Joules/kg) per ion calculated by SRIM2008 [127]. The active nanocircuit area was about $250x250$ μm^2. The number of ions in the 10×10 mm^2 beam intercepted by the active nanocircuit area over ~ 30 min was, therefore, $\sim 3.5 \times 10^6$ ions. The thermal oxide in the active nanocircuit region, therefore, received $\sim 8 \times 104$ Gy $= 8 \times 10^6$ Rad. In conventional MOSFETs in radiation environments, charging/discharging of oxide layer traps is a primary reason for deleterious changes in device performance. Radiation-hardening research for conventional MOSFETs focuses on the creation of radiation-resistant insulating layers, such as

high-k dielectrics or ultra-defect-free SiO_2. A typical goal for radiation-hardened ultra-pure SiO_2 is 10^6 Rad. The thermal oxides used in the present nanoFETs were good quality, but they were not radiation hard. Therefore, this investigation indicates the capacitive coupling of the oxide to the nanowire, was reliably weak, which could result in increased circuit resilience. Investigations of whether the charging or discharging of oxide traps could have caused field manipulation of the Schottky barriers resulting in the observed shifts of the IV characteristics to the right are continuing.

Recent and earlier SEM work indicates that heavy ion interactions with the nanowire itself can take the form of puffs of amorphization[128, 129], demonstrated in Figure 5.1. This is under investigation currently by the present author aiming to further understand the nanoscale material properties and their reaction to radiation which will be published separately. Increased extent (diameter) of the amorphous regions was observed for the nanowire in nanoFET2 compared with the nanowire in nanoFET1. As described in this thesis, a fundamental study based on energy loss and extracted voltage values provides information on potential drop V_2 across the nanowire itself and also about the sum of all voltage values $V_1 + V_2 + V_3$. It is worth noting that the sum of all voltage value does not add up to the external bias value for nanoFET2, which indicates that energy is lost elsewhere in the system. An investigation of the extent of amorphization versus the amount of energy loss is ongoing.

The effects of radiation interactions with reduced dimensionality materials and devices is a new research area with fundamental interest motivated by the novel phenomenon that can result from energy and momentum scattering mechanisms that are restricted by quantization.

The extent of this work includes using thermionic field emission model to investigate other nanowire/nano-channel based nanoFET devices as indicated in chapter 3. In the world of fabrication, however, new and advanced NanoFET based on different semiconductor and metal contacts are studied and built with the purpose of making shorter and more efficient devices for a variety of applications[130, 131, 132, 133, 134]. The use of the stability approach
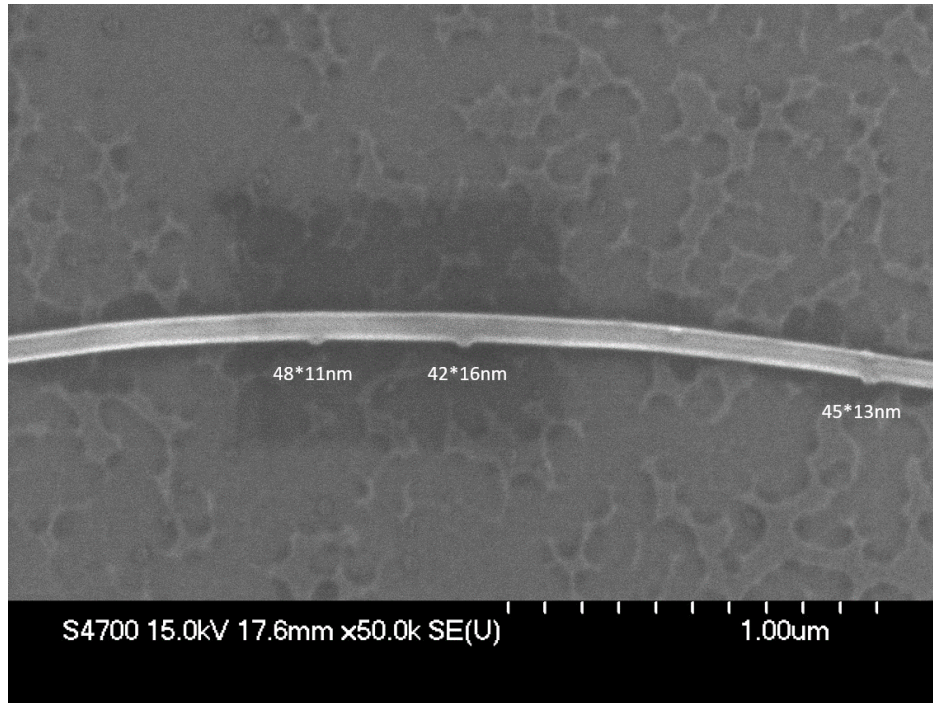
Figure 5.1 nanowire with Puff Ball on surface Post radiation.

as parts of the fitting method for thermionic field emission model can easily be carried into the study of the newer generations of NanoFET devices as can the Metal-Semiconductor-Metal formulation. The Schottky barrier itself is a universal barrier type independent of device structure and fabrication technique.

5.3.3 Quantum Communication SAW device in Space

As the fabricated SAW are undergoing tests at the NASA Goddard Spaceflight Center, a significant amount of research is still needed to make this quantum communication relay a reality. The study continues to investigate how SAW is interacting with the qubit encoding medium, [54] the build of read-in and read-out circuitry, and the interference and boundary condition of the device. Density functional theory analysis for the qubit medium and for its interaction with the SAW is in progress at the Electrical and Biological Nanostructure Laboratory.

BIBLIOGRAPHY

BIBLIOGRAPHY

[1]   K. Jones and J. Gross, "Reducing size, weight and power (swap) of perception systems in small autonomous aerial systems," *Aviation Conference*, 2014.

[2]   R. L. Fusaro, "Lubrication of space systems," *NASA Technical Memorandum*, no. 106392, 1994.

[3]   J. Xiao, G. Ouyang, P. Liu, and G. Yang, "Reversible nanodiamond-carbon onion phase transformations," *Nano Letters*, no. 14, 2014.

[4]   "Cubesats overview." `https://www.nasa.gov/mission_pages/cubesats/overview`. Accessed: 2018-04-15.

[5]   K. A. LaBel, "Radiation effects on electronics 101: Simple concepts and new challenges." `https://nepp.nasa.gov/DocUploads/392333B0-7A48-4A04-A3A72B0B1DD73343/Rad_Effects_101_WebEx.pdf`. Accessed: 2018-06-20.

[6]   "Radiation hardening." `https://en.wikipedia.org/wiki/Radiation_hardening`. Accessed: 2018-06-20.

[7]   A. H. Siedle and L. Adams, *Handbook of Radiation Effects*. Oxford University Press, 2002.

[8]   "http://www. nscl. msu. edu/tech/index. html."

[9]   R. Ladbuty, R. A. Reed, P. Marshall, K. A. LaBel, R. Anantaraman, R. Fox, D. P. Sanderson, A. Stolz, J. Yurkon, A. F. Zeller, and J. W. Stretson, "Performance of the high energy single event effects test facilirty (seetf) at michigan state university national superconducting cyclotron laboratory (nscl)," *IEEE T Nucl.Sci*, 2004.

[10] E. E. Bisson, "Lubrication and bearing problems in the vacuum of space," 1966.

[11] E. McMurtrey, "High performance solid solid and liquid lubricants-an industrial guide," *Noye Data Corporation*, 1987.

[12] E. Zaretsky, "Liquid lubrication in space," *Tribology International*, no. 23, 1990.

[13] A. Babecki, W. Grenier, and C. Haehner, "An evaluation of liquid and grease lubricants for spacecraft applications," *NASA TM*, no. 82275, 1976.

[14] F. Delaat, R. Shelton, and J. Kimzey, "Status of lubricants for manned spacecraft," *Lubr.Eng*, no. 23, 1967.

[15] P. Conley and J. Bohner, "Experience with synthetic fluorinated fluid lubricants," *Proceedings of the 24th Aerospace Mechanisms Symposium*, no. 213, 1990.

[16] G. Venier and E. Casserly, "Multipy-alkylated cyclopentanes (macs): A new class of synthesized hydrocarbon films," *Lub.Eng.*, no. 23, 1990.

[17] E. McMurtrey, "Lubrication handbook for the space industry," *NASA TM*, no. 86556, 1985.

[18] K. W. S. Jr and K. Miyoshi, "Application of carbon based nano-materials to aeronautics and space lubrication," *NASA/TM*, no. 214473, 2007.

[19] A. Hirata, M. Igarashi, and T. Kaito, "Study on solid lubricant properties of carbon onions produced by heat treatment of diamond clusters or particles," *Tribology International*, vol. 37, no. 899-905, 2004.

[20] K. A. LaBel, "Radiation effects on electronics 101: Simple concepts and new challenges," 2004.

[21] D. M. Fleetwood, P. S. Winokur, and P. E. Dodd, "An overview of radiation effects on electronics in the space telecommunications enviroments," *Microelectronics Reliability*, 2000.

[22] Y. H. Lho and K. Y. Kim, "Radiation effects on the power mosfet for space applications," *ETRI Journal*, no. 4, 2005.

[23] A. S. Keys, M. D. Watson, D. O. Frazier, J. H. Adams, M. A. Johnson, and E. A. Kolawa, "High performance,radiation-hardened electronics for space environments," 2017.

[24] K. Neumeier, P. Seegebrecht, and H. P. Bruemmer, "Radiation tolerance of double layer field oxides," *IEEE*, 1992.

[25] M. Inoue, T. Kobayashi, and A. Maruyama, "High reliability power mosfets for space application," 2010.

[26] T. R. Oldham, F. B. McLean, H. E. Boesch, and J. M. McGarrity, "An overview of radiation-inducted interface traps in mos structures," 1989.

[27] J. Piscator and O. Engstrom, "Schottky barrier modulation on silicon nanowires," *Appl.Phys.Lett*, no. 90, 2007.

[28] L. Mu, Y. Chang, S. Sawtelle, M. Wipf, X. Duan, and M. Reed, "Silicon nanowire field-effect transistors?a versatile class of potentiometric nanobiosensors," *IEEE Access*, no. 3, 2015.

[29] T. Lobanova, Y. Vorontsov, and S. Kalinin, "The modern technology for silicon nanofet," *IEEE Xplore*, no. 1815, 2006.

[30] J. Choi, "Sic nanowires : from growth to related devices." `https://tel.archives-ouvertes.fr/tel-01061784`. Accessed: 2018-07-14.

[31] D. Wu, Y. Jiang, X. Yao, Y. Chang, Y. Yu, Z. Zhu, Y. Zhang, X. Lan, and H. ZHong, "Construction of crossed heterojunctions from p-znte and n-cdse nanoribbons and their photoresponse properties," *Journal of Materials Chemistry C*, no. 6547, 2014.

[32] S. M. Sze and K. K. Ng, *Physics of semiconductor devices.* Hoboken, N.J.: Wiley-Interscience, 2007.

[33] "Schottky barrier height basics." `http://academic.brooklyn.cuny.edu/physics/tung/Schottky/index.htm`. Accessed: 2018-06-20.

[34] R. Agarwal and C. M. Lieber, "Semiconductor nanowires: optics and optoelectronics," *Applied Physics A*, no. 85, 2006.

[35] "Gan devices bring benefits to pol dc-dc converter designs." `http://www.electronicdesign.com/analog/gan-devices-bring-benefits-pol-dc-dc-converter-designs`. Accessed: 2018-04-15.

[36] S. J. Pearton, F. Ren, E. Patrick, M. E. Law, and A. Y. Polyakov, "Review?ionizing radiation damage effects on gan devices," *ECS Journal of Solid State Science and Tachnology*, no. 5, 2016.

[37] S. Bazzoli, S. Girard, V. F. Cavrois, J. Baggio, P. Paillet, and O. Duhamel, "See sensitivity o f a cots gan transistor and silicon mosfets," *IEEE*, no. 978, 2007.

[38] S. Onoda, A. Hasuike, Y. Nabeshima, H. Sasaki, K. Yajima, S. Sato, and T. Ohshima, "Single-event damages caused by heavy ions observed in algan/gan hemts," *IEEE Translation On Nuclear Science*, no. 6, 2013.

[39] M. Rostewitz, K. Hirche, J. Latti, and E. Jutzi, "Single event effect analysis on dc and rf operated algan/gan hemts," *IEEE*, no. 0018, 2013.

[40] L. Scheick, "Determination of single-event effect application requirements for enhancement mode gallium nitride hemts for use in power distribution circuits," *IEEE Translation On Nuclear Science*, no. 6, 2014.

[41] M. Q. He, P. Z. Zhou, S. N. Mohammad, G. L. Harris, J. B. Halpern, R. Jacobs, W. L. Sarney, and L. Salamanca-Riba, "Growth of gan nanowires by direct reaction of ga with nh3 j cryst growth," *J Cryst Growth*, vol. 231, pp. 357–65, 2001.

[42] B. W. Jacobs, V. M. Ayres, M. P. Petkov, J. B. Haplern, M. Q. He, A. D. Baczewski, K. McElroy, M. A. Crimp, J. Zhang, and H. C. Shaw, "Electronic and structural characteristics of zinc-blende wurtzite biphasic homostructure gan nanowires," *Nano Lett*, vol. 7, pp. 1435–1438, 5.

[43] B. W. Jacobs, V. M. Ayres, R. E. Stallcup, A. Hartman, M. A. Tupta, A. D. Baczewski, M. A. Crimp, J. B. Halpern, M. He, and H. C. Shaw, "Electron transport in zinc-blende wurtzite biphasic gallium nitride nanowires and ganfets," *Nanotechnology*, no. 18, 2007.

[44] B. W. Jacobs, K. McElroy, R. A. Al-Duhauleb, M. A. Crimp, and V. M. Ayres, "Cross-section high resolution transmission electron microscopy and nanoprobe investigation of gallium nitride nanowires," *Int.J. Nanomanufacturing*, vol. 6, 2010.

[45] B. W. Jacobs, M. A. Crimps, K. McElroy, and V. M. Ayres, "Nanopipes in gallium nitride nanowires and rods," *Nano Letters*, no. 12, 2008.

[46] V. M. Ayres, B. W. Jacobs, M. E. Englund, E. H. carey, M. A. Crimp, R. M. Ronningen, A. F. Zeller, J. B. Halpern, M. Q. He, G. L. Harris, D. liu, H. C. Shaw, and M. P. Petkov, "Investigations of heavy ion irradiation of gallium nitride nanowires and nanocircuits," *Diamond and Related Materials*, no. 15, 2006.

[47] H. Takenaka, A. C. Casado, M. Fujiwara, M. Kitamura, M. Sasaki, and M. Toyoshima, "Satellite to ground quantum limited communication using a 50kg class microsatellite," *Nature Photonics*, vol. 107, 2017.

[48] NASA, "Cubesat based science missions. for geospace and atmospheric research," 2013.

[49] D. K. Oi, A. Ling, G. Vallone, P. Villoresi, S. Greenland, E. Kerr, M. Macdonald, H. Weinfurter, H. Kuiper, E. Charbon, and R. Ursin, "Cubesat quantum communication mission," *EPJ Quantum Technol*, vol. 4, 2017.

[50] Quantum entanglement, "Quantum entanglement," 2017.

[51] C. L. Lee, X. Wei, Q. Li, R. Carpick, J. W. Kysar, and J. [Hone, "Elastic and frictional properties of graphene," *Phys. Status Solidi Bl*, vol. 246, no. 2562-2567, 2009.

[52] C. H. W. Barnes, J. M. Shilton, and A. M. Robinson, "Quantum computation using electrons trapped by surface acoustic waves," *Physical Review B*, vol. 62, pp. 8410–8419, 2000.

[53] R. P. G. McNeil, M. Kataoka, C. J. B. Ford, C. H. W. Barnes, D. Anderson, G. A. C. Jones, I. Farrer, and D. A. Ritchie, "On-demand single-electron transfer between distant quantum dots," *Nature*, vol. 447, pp. 439–442, 2010.

[54] T. Aref, P. Delsing, M. Ekstrom, A. F. Kockum, M. V. Gustafsson, G. Johansson, P. Leek, E. Magnusson, and R. Manenti, "Quantum acoustics with surface acoustic waves," *Superconducting Devices in Quantum Optics*, 2016.

[55] J. Koch, T. M. Yu, J. Gambetta, A. A. Houck, D. I. Schuster, J. Majer, A. Blais, M. H. Devoret, S. M. Girvin, and R. J. Schoelkopf, "Charge-insensitive qubit design derived from the cooper pair box," *Physcial Rev A*, no. 76, 2007.

[56] S. Datta, *Electronic Transport in Mesoscopic Systems*. Cambridge, UK, Cambridge University Press, 1997.

[57] S. Battisti, R. Bossart, H. Schonbacher, and M. V. de Voorde, "Radiation damage to electronic components," *Nuclear Instruments and Methods*, no. 136, 1976.

[58] T. Raymond, "The physics and chemistry of the schottky barrier height," *Applied Physics Reviews*, no. 1, 2014.

[59] F. A. Padovani and R. Stratton, "1966 field and thermionic-field emission in schottky barriers," *Solid State Electron*, vol. 9, pp. 695–707, 1966.

[60] A. I. Lvovsky, "Photonic qubits: A quantum delivery note," *Nature Physics*, no. 9, 2013.

[61] J. J. Pla, K. Y. Tan, J. P. Dehollain, W. H. Lim, J. J. Morton, D. N. Jamieson, A. S. Dzurak, and A. Morello, "A single-atom electron spin qubit in silicon," *Nature*, no. 489, 2012.

[62] S. Maximillian, "Decoherence, the measurement problem, and interpretations of quantum mechanics," *Reviews of Modern Physics*, no. 76, 2005.

[63] L. Rayleigh, "On wves propagated along the plane surface of an elastic solid," *Proc.London Math Soc*, no. s1-17, 1885.

[64] N. Ohno, S. Mia, and S. Obara, "Friction and wear characteristics of advanced space lubricants," *Tribology Transactionsl*, vol. 53, no. 249-255, 2010.

[65] P. J. Bryanta, P. L. Gutshalla, and L. H. Taylora, "A study of mechanisms of graphite friction and wear," *Wear*, vol. 7, no. 118, 1964.

[66] W. Xueshen, L. Qunqing, X. Jing, J. Zhong, W. Jinyong, L. Yan, J. Kaili, and F. Shoushan, "Fabrication of ultralong and electrically uniform single-walled carbon nanotubes on clean substrates," *Nano Letters*, vol. 9, no. 9, pp. 3137–3141, 2009. PMID: 19650638.

[67] C. Cress, C. Schauerman, B. Landi, S. Messenger, R. Raffaelle, and R. Walters, "Radiation effects in single-walled carbon nanotube papers," *Journal of Applied Physics*, no. 107, 2010.

[68] A. Hirata and N. Yoshioka, "Sliding friction properties of carbon nanotube coatings deposited by microwave plasma chemical vapor deposition," *Tribology International*, vol. 37, no. 893-898, 2004.

[69] E. Akatyeva, J. Y. Huang, and T. Dumitrica, "Edge-mediated dislocation processes in multishell carbon nano-onions," *Phys. Rev. Lett*, vol. 105, no. 106102, 2010.

[70] O. O. Oleksandr, Y. M. Solonin, D. N. Batchelder, and R. Brydson, "Transformation of nanodiamond into carbon onions," *J. Appl. Phys*, vol. 97, no. 074302 1-16, 2005.

[71] Y. V. Butenko, S. Krishnamurthy, A. K. Chakraborty, V. L. Kuznetsov, V. R. Dhanak, and M. R. C. Hunt, "Photoemission study of onionlike carbons produced by annealing nanodiamonds," *Phys. Rev. B*, vol. 71, p. 075420, Feb 2005.

[72] J, J. F Ziegler, M. P Biersack, and D. Ziegler, "Srim: The stopping and range of ions in matter."

[73] R. Alduhailed, V. Ayres, B. Jacobs, X. Fan, K. McElroy, M. Crimp, A. Hirata, and M. Horikoshi, "Carbon onion films-molecular interactions of multi-layer fullerenes," *Material Research Society Symposium*, no. 1204, 2010.

[74] W. Li, X. Wang, X. Zhang, S. Zhao, H. Duan, and J. Xue, "Mechanism of the defect formation in supported graphene by energetic heavy ion irradiation: The substrate effect," *Scientific Reports*, no. 5, 2015.

[75] A. J. McKenna, T. Trevethan, C. D. Latham, P. J. Young, and M. I. Heggie, "Threshold displacement energy and damage function in graphite from molecular dynamics," *Carbon*, no. 99, 2016.

[76] S and Ahmad, "Continuum elastic model of fullerenes and the sphericity of the carbon onion shells," *J. Chem. Phys*, vol. 116, 2002.

[77] R. Al-Duhailed, K. Xie, V. Ayres, R. Ronningen, A. Zeller, T. Bauman, and A. Hirata, "Investigations of zipping mechanism in relativistic heavy ion interactions with carbon onions," *Mater.Res.Soc.Symp.Proc*, no. 1407, 2012.

[78] A. V. Eletskii, "Carbon nanotubes and their emission properties," *Phys. Usp.*, vol. 45, no. 4, pp. 369–402, 2002.

[79] A. V. Siklitskaya, S. G. Yastrebov, and R. Smith, "Statistical analysis of interatomic bonds and interlayer distances in a carbon helical onion structure with a variable step," *Technical Physics Letters*, vol. 38, pp. 891–894, Oct 2012.

[80] A. V. Krasheninnikov and N. K., "Irradiation effects in carbon nanotubes," *Nuclear Instruments and Methods in Physics Research B*, vol. 216, pp. 355–366, 2004.

[81] M. Terrones, F. Banhart, N. Grobert, J.-C. Charlier, H. Terrones, and P. M. Ajayan, "Molecular junctions by joining single-walled carbon nanotubes," *Phys. Rev. Lett.*, vol. 89, p. 075505, Jul 2002.

[82] B, M. Peng, P. Locascia, S. Zapol, S. Li, G. L Mielke, H. Schatz, and D. Espinosa, "Measurements of near-ultimate strength for multiwalled carbon nanotubes and irradiation-induced crosslinking improvements.," *Nature Nanotech*, vol. 3626, 2008.

[83] J. H. Warner, N. P. Young, A. I. Kirkland, and G. A. D. Briggs, "Resolving strain in carbon nanotubes at the atomic level," *Nature Materials*, no. 10, 958-962.

[84] D. Baowan, N. Thamwattana, and J. M. Hill, "Continuum modeling of spherical and spheroidal carbon onions," *Eur. Phys. J. D*, vol. 44, no. 117, 2007.

[85] K. Xie, S. A. Hartz, V. M. Ayres, Z. Liu, B. W. Jacobs, T. Baumann, R. M. Ronningen, A. F. Zeller, and M. A. Tupta, "2013 real-time investigation of nanofet current surge capability during heavy ion irradiation," *MRS Online Proceedings*, vol. 1512, 2013.

[86] B. W. Jacobs, V. M. Ayres, M. A. Crimp, and K. McElroy, "Internal structure of multiphase zinc-blende wurtzite gallium nitride nanowires," *Nanotechnology*, vol. 19, 2008.

[87] K. Xie, S. A. Hartz, V. M. Ayres, B. W. Jacobs, R. M. Ronningen, A. F. Zeller, T. Baumann, and M. A. Tupta, "Thermionic field emission in gan nanofet schottky barriers," *Materials Research Expressl*, vol. 2, p. 015003, 2015.

[88] C. cheidenberger, T. Stohlker, W. E. Meyerhof, H. Geissel, P. H. Mokler, and B. Blank, "Charge states of relativistic heavy ions in matter," *Nucl Instrum Meth B*, vol. 142, p. 142, 1998.

[89] A. A. Talin, F. Leonard, B. S. Swartzentruber, X. Wang, and S. D. Hersee, "Unusually strong space-charge-limited current in thin wires," *Phys Rev Lett*, vol. 101, 2008.

[90] J. R. Kim, H. Oh, H. M. So, J. J. Kim, J. Kim, C. J. Lee, and S. C. Lyu, "Schottky diodes based on a single gan nanowire," *Nanotechnology*, vol. 13, pp. 701–4, 2002.

[91] S. Y. Lee and S. K. Lee, "Current transport mechanism in a metal-gan nanowire schottky diode," *Nanotechnology*, vol. 18, p. 495701, 2007.

[92] C. C. Chen, M. Aykol, C. C. Chang, A. F. J. Levi, and S. B. Cronin, "Graphene-silicon schottky diodes," *Nano Lett*, vol. 11, pp. 1863–7, 2001.

[93] S. Heinze, J. Tersoff, R. Martel, V. Derycke, J. Appenzeller, and P. Avouris, "Carbon nanotubes as schottky barrier transistors," *Phys Rev Lett*, vol. 89, p. 186801, 2002.

[94] S. M. Sze, D. J. Coleman, and A. Loya, "Current transport in metal-semiconductor-metal (msm) structures," *Solid State Electron*, vol. 14, pp. 1209–81, 1971.

[95] C. R. Crowell and V. L. Rideout, "Normalized thermionic-field (t-f) emission in metal-semiconductor (schottky) barriers," *Solid State Electron*, vol. 12, pp. 89–105, 1969.

[96] E. E. Anderson, *Modern physics and quantum mechanics*. Philadelphia,: Saunders, 1971.

[97] Z. Y. Zhang, C. H. Jin, X. L. Liang, Q. Chen, and L. M. Peng, "Current-voltage characteristics and parameter retrieval of semiconducting nanowires," *Appl Phys Lett*, vol. 89, p. 073102, 2006.

[98] C. R. Crowell and V. L. Rideout, "Normalized thermionic-field (t-f) emission in metal-semiconductor (schottky) barriers," *Solid State Electron*, vol. 12, pp. 89–105, 1969.

[99] Y. Huang, X. F. Duan, Y. Cui, and C. M. Lieber, "Gallium nitride nanowire nanodevices," *Nano Lett*, vol. 2, pp. 101–4, 2002.

[100] J. Wen, X. T. Zhang, H. Gao, and M. J. Wang, "Current-voltage characteristics of the semiconductor nanowires under the metal-semiconductor-metal structure," *J Appl Phys*, vol. 114, p. 223713, 2013.

[101] L. Kenneth, "A method for the solution of certain non-linear problems in least squares," *Quarterly of Applied Mathematics*, vol. 2, 1944.

[102] D. Marquardt, "An algorithm of least-squares estimation of nonlinear parameters," *SIAM Journal on Applied Mathematics*, vol. 11, 1963.

[103] A. C. Schmitz, A. T. Ping, M. A. Khan, Q. Chen, J. W. Yang, and I. Adesida, "Schottky barrier properties of various metals on n-type gan," *Semicond Sci Tech*, vol. 11, pp. 1464–7, 1996.

[104] J. Pujol, "The solution of nonlinear inverse problems and the levenberg-marquardt method," *Geophysics*, vol. 72, pp. W1–W16, 2007.

[105] J. Wallentin, M. Ek, L. R. Wallenberg, L. Samuelson, and M. T. Borgstrom, "Thermionic field emission in gan nanofet schottky barriers," *Nano Lett*, vol. 12, pp. 151–5, 2012.

[106] H. Jung, D. Y. Park, F. Xiao, K. H. Lee, Y. H. Choa, B. Yoo, and N. V. Myung, "Electrodeposited single crystalline pbte nanowires and their transport properties," *J Phys Chem C*, vol. 115, pp. 2993–8, 2011.

[107] "Lunar laser communication demonstration nasa?s first space laser communication system demonstration." `https://www.nasa.gov/sites/default/files/llcdfactsheet.final_.web_.pdf`. Accessed: 2018-05-06.

[108] D. Collins, N. Gisin, and H. Riedmatten, "Quantum relays for long distance quantum cryptography," *Journal of Modern Optics*, no. 52, 2005.

[109] D. Stucki, N. Gisin, O. Guinnard, G. Ribordy, and H. Zbinden, "Quantum key distribution over 67 km with a plug and play system," *New Journal of Physics*, no. 4, 2002.

[110] C. Gobby, Z. Yuan, and A. Shields, "Quantum key distribution over 122 km of standard telecom fiber," *Applied Physics Letters*, no. 84, 2004.

[111] H. Briegel, W. Dur, J. Cirac, and P. Zoller, "Quantum repeaters: The role of imperfect local operations in quantum communication," *Phys.Rev.Lett*, no. 81, 1998.

[112] A. Ekert, "Quantum cryptography based on bell?s theorem," *Phys.Rev.Lett*, no. 67, 1991.

[113] C. Bennett, G. Brassard, S. Popescu, B. Schumatcher, J. Smolin, and W. Wootters, "Purification of noisy entanglement and faithful teleportation via noisy channels," *Phys.Rev.Lett*, no. 76, 1996.

[114] L. Rayleigh, "On waves propagated along the plane surface of an elasticsolid," 1885.

[115] "Quartz cut angle." `http://www.mecquartz.com/html/info.html`. Accessed: 2018-01-22.

[116] D. L. T. Bell and R. C. M. LI, "Surface acoustic wave resonators," *IEEE Proceeding*, vol. 64, 1976.

[117] N. Ramakrishnan, H. B. Nemade, and R. P. Palathinkal, "Resonant frequency characteristics of a saw device attached to resonating micropillars," *Sensors*, vol. 12, 2012.

[118] S. Dixit and R. C. Jain, "Surface acoustic waves based mems resonator," *COMSOL Conference Proceeding*, 2014.

[119] R. M. White and F. M. Voltmer, "Direct piezoelectric coupling to surface elastic waves," *Appl. Phys. Lett.*, no. 12, 1965.

[120] N. Miyazaki, A. Hattori, and H. Uchida, "Thermal shock cracking of lithium niobate single crystal," *Journal of Materials Science: Materials in Electronics*, no. 3, 1997.

[121] "About lnf." `https://lnf.umich.edu/about-lnf/`. Accessed: 2018-01-20.

[122] "Heidelberg upg mask 501 maker." `http://lnf-wiki.eecs.umich.edu/wiki/Heidelberg_%C2%B5PG_501_Mask_Maker`. Accessed: 2018-01-20.

[123] "Cee 100cb photoresist spinner." `http://lnf-wiki.eecs.umich.edu/wiki/CEE_100CB_photoresist_spinner`. Accessed: 2018-01-20.

[124] "Ma/ba-6 mask/bond aligner." `http://lnf-wiki.eecs.umich.edu/wiki/MA-BA-6_Mask-Bond_Aligner`. Accessed: 2018-01-20.

[125] "Yes-cv200rfs(e)." `http://lnf-wiki.eecs.umich.edu/wiki/YES-CV200RFS(E)`. Accessed: 2018-01-20.

[126] "Enerjet evaporator." `http://lnf-wiki.eecs.umich.edu/wiki/Enerjet_Evaporator`. Accessed: 2018-01-20.

[127] J. F. Ziegler, J. P. Biersack, and M. D. Ziegler, "Srim: The stopping and range of ions in matter."

[128] A. Botman, A. Bahm, S. Randolph, M. Straw, and M. Toth, "Spontaneous growth of gallium-filled microcapillaries on ion-bombarded gan," *Physical Review Letters*, vol. 111, 2013.

[129] Q. Wei, J. Lian, W. Lu, and L. Wang, "Highly ordered ga nanodroplets on a gaas surface formed by a focused ion beam," *Physical Review Letters*, vol. 100, 2008.

[130] D. Martin, A. Heinzig, M. Grube, L. Geelhaar, T. Mikolajick, H. Riechert, and M. Weber, "Probing of schottky barriers in si nanowire schottky barrier field effect transistors," *Physical Review Letters*, vol. 107, 2011.

[131] K. Yoon, J. K. Hyun, J. G. Connell, I. Amit, Y. Rosenwaks, and L. J. Lanhon, "Barrier height measurement of metal contacts to si nanowires using internal photoemission of hot carriers," *NanoLetters*, vol. 13, 2013.

[132] S. Yeong-Tai, L. Kook-Nyung, J. Kuk, L. M. Ho, L. HyungSu, S. Wookyeong, and K. Yong-Kweon, "Negative ions detection in air using nano field-effect-transistor (nanofet)," *Micro and Nano Systems Letters*, vol. 2, 2011.

[133] C. C. Chen, M. Aykol, C. C. Chang, A. F. J. Levi, and S. B. Cronin, "Graphene-silicon schottky diodes," 2011.

[134] K. Skucha, Z. Fan, K. Jeon, A. Javey, and B. Boser, "Palladium/silicon nanowire schottky barrier-based hydrogen sensors," *Sensors and Actuators B: Chemical*, vol. 145, 2010.